RCA Review

A technical journal published quarterly
by RCA Research and Engineering
in cooperation with the subsidiaries
and divisions of RCA.

Contents

September 1971 Volume 32 Number 3

RCA Corporation

Robert W. Sarnoff Chairman of the Board and Chief Executive Officer
A. L. Conrad President and Chief Operating Officer

Editorial Advisory Board

Chairman, J. A. Rajchman RCA Laboratories
E. D. Becken RCA Global Communications
G. H. Brown RCA Patents and Licensing
G. D. Cody RCA Laboratories
H. L. Cooke, RCA Research and Engineering
A. N. Goldsmith Honorary Vice President, RCA
N. L. Gordon RCA Laboratories
G. B. Herzog RCA Laboratories
J. Hillier RCA Research and Engineering
E. O. Johnson RCA Solid-State Division
H. W. Leverenz RCA Patents and Licensing
D. S. McCoy RCA Laboratories
H. F. Olson RCA Laboratories
K. H. Powers RCA Laboratories
P. Rappaport RCA Laboratories
F. D. Rosi RCA Laboratories
L. A. Shotliff RCA International Licensing
T. O. Stanley RCA Laboratories
J. J. Tietjen RCA Laboratories
W. M. Webster RCA Laboratories
L. R. Weisberg RCA Laboratories

Secretary, Charles C. Foster RCA Research and Engineering

Editor Ralph F. Ciafone

Associate Editors

W. A. Chisholm RCA Limited
D. B. Dobson Aerospace System Division
M. G. Gander RCA Service Company
T. G. Greene Missile and Surface Radar Division
W. O. Hadlock RCA Research and Engineering
W. A. Howard National Broadcasting System
C. Hoyt Consumer Electronic Systems Division
C. A. Meyer RCA Electronic Components
M. G. Pietz Defense Engineering
C. W. Sall RCA Laboratories
I. M. Seideman Astro-Electronics Division
W. Varnum Commercial Electronic Systems Division

© RCA Corporation 1971 All Rights Reserved Printed in USA

A Bipolar Transistor Model for Device and Circuit Design

R. B. Schilling

Solid State Division, Somerville, N. J.

Abstract—The regional approximation technique is used for the development of transistor models. This technique uses the interaction of physics and mathematics. Physics is used as a guide to the mathematical approximations. A linearized version of the Linvill lumped model is developed that is highly useful to both circuit and device designers. Model parameters are found from the charge distribution. Model development using the regional approximation technique allows for adjusting the complexity of the model. It is shown how a single region can adequately predict device performance under extreme base-widening conditions.

The device model's success is determined by the degree to which it represents physical reality while minimizing mathematical complexity.

1. Introduction

Renewed interest in the bipolar transistor has taken place during the last few years due to the advent of computer-aided design. This interest is centered on development of transistor models. Both circuit and device designers are seeking models that will predict performance over wide ranges of device operation. To satisfy both elements and to close the loop between them (in order to design the device for improved circuit performance) requires a model that is based on the internal physics of the device (the doping profile). In addition, the model must be capable of handling effects such as base-widening, conductivity

---

* A more detailed version of this paper is scheduled to be published by McGraw Hill, Inc., N.Y., as Chapter 1 in a book entitled *Modeling of Solid-State Devices for Computer-Aided Design.*

modulation, and other high-injection-level phenomena that are commonplace during operation of present-day transistors.

Analysis techniques from which transistor models have been derived fall into three categories: the classical-analytical approach,[1] the total computer approach,[2] and the recently presented regional approximation method (RAM).[3] The standard single-lump models (Linvill, Charge-Control and Ebers–Mole) are based on the classical approach. The classical approach has the advantage of an analytically tractable solution, simplicity, and a clear description of the physics. However, this approach is based on low-level injection and very simplified doping profiles. The single-lump models derived from the classical approach are therefore limited in scope. The total computer approach uses iterative techniques to solve the basic transistor equations. The results obtained using this approach are highly accurate (perhaps more accurate than is possible for the material parameters to be determined); however, the complexity of the approach is far too great to be of use in computer-aided design. The regional approximation method is based on dividing the transistor into physically defined regions. By combining this technique with computer monitoring of approximations, significant simplifications can be self-consistently made while a high level of accuracy can be maintained. In addition, defining regions by boundaries that depend on the operating voltage and current emphasizes the underlying physics and aids significantly in understanding the problem.

The results presented herein demonstrate that an analytically tractable determination of certain transistor parameters (electric field, charge densities, etc.) can be obtained under wide ranges of device operation. Many of the approximations used to obtain the analytical solution were determined by careful scrutiny of the computer results obtained using the regional approximation method. For this reason, the regional approximation method will be reviewed as an integral part of the analytical technique. Attention will be focused on high-level conditions of operation, because solutions under low-level conditions are readily available in the literature.

1.1 Structure

The structure we consider is that of the planar n+-pνn+ transistor illustrated in Fig. 1 (ν indicates a lightly doped n region). Under low-level conditions of operation, the active region requiring study (the base region) would be the fixed region contained between the emitter junction plane at $x = 0$ and the collector-junction plane at $x = x_{MJ}$, both of which are defined by the metallurgical preparation of the structure.

In practice, under high-level conditions of operation (e.g., high-current low-voltage conditions) there can be substantial base widening, even to the point where the base reaches the metallic collector plane at $x = L$ in Fig. 1. The regional approximation method must, therefore, provide regions whose boundaries are functions of the operating voltage and current. To this end the problem is divided into three separate regions, each dominated by separate physical considerations. The regions, as shown in Fig. 1, are the base, transition, and ohmic collector regions. The boundaries between regions, x_1 and x_2, are functions of emitter current I_E and collector-to-emitter voltage V_{CE}. This procedure not only keeps the underlying physics clearly in view, but greatly simplifies the determining equations, allowing analytical solutions to be obtained.

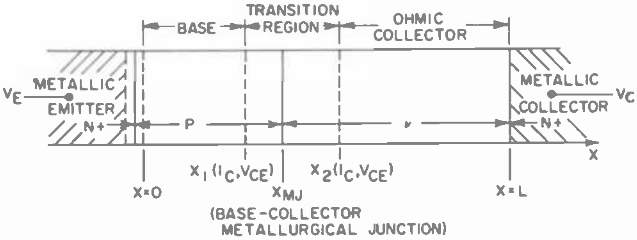

Fig. 1—One-dimensional transistor structure.

1.2 General Equations

The following equations characterize the transistor problem: the electron-current density equation,

$$J_n = e\mu_n nE + eD_n \frac{dn}{dx}\,; \qquad [1]$$

the hole-current density equation,

$$J_p = e\mu_p pE - eD_p \frac{dp}{dx}\,; \qquad [2]$$

the total-current density equation

$$J = J_n + J_p = \text{constant}; \qquad [3]$$

the Poisson equation

$$\frac{\epsilon}{e}\frac{dE}{dx} = p - n - N(x)\,; \qquad [4]$$

the electrostatic potential equation

$$\psi = -\int E dx\,; \qquad [5]$$

the electron particle-conservation equation

$$\frac{dJ_n}{dx} = -e(g-r)\,; \qquad [6]$$

and the hole particle-conservation equation

$$\frac{dJ_p}{dx} = e(g-r). \qquad [7]$$

where

D_n, D_p = electron and hole diffusion coefficients
e = absolute value of electron charge
E = electric field
n, p = electron and hole densities
μ_n, μ_p = electron and hole mobilities
ϵ = dielectric constant
N = doping profile
g = generation rate of electron–hole pairs
r = recombination rate of electron–hole pairs

For the case of the n-p-n transistor, the dominant carriers are electrons. The hole current J_p is, therefore, significantly less than either of its two components, i.e., it is a small difference between two much larger currents. Further, with operation at useful values of gain, neither the generation nor recombination of carriers significantly perturb the current flow. With these "classical" approximations, Eq. [1] can be replaced by

$$J_n = e\mu_n nE + eD_n \frac{dn}{dx} \simeq J = \text{constant}, \qquad [8]$$

and Eq. [2] by

$$E \simeq \frac{D_p}{\mu} \frac{dp/dx}{p} \qquad [9]$$

Eqs. [8] and [9], together with Eqs. [4] and [5], constitute the simplified transistor equations. From these equations, given J, ψ, and the doping profile $N(x)$, the quantities n, E, and the gain are determined. In practice, J and a boundary condition on n are used to generate $n(x)$ and $E(x)$, from which ψ is found from Eq. [5].

Reduction of Eqs. [4], [8], and [9] to an equation in one variable yields a highly nonlinear third-order differential equation. In contrast, through the use of the regional approximation method (RAM), only first-order differential equations will result, requiring substantially less computer time for solution and allowing rate-of-change calculations to be made using a slide rule. Also, through careful study of the results of the regional approximation method, a number of useful analytical equations can be obtained.

2. Review of Regional Approximation Method[4]

There are three regions in the problem, as illustrated in Fig. 1. Region I, adjacent to the emitter, is the classical base region characterized by approximate local neutrality. It terminates at the plane x_1 where this neutrality approximation runs out of self-consistency, namely where the neglected space charge $(\epsilon/e)(dE/dx)$ catches up with the separate components of charge in the base region. With this criterion, the base width is obviously not fixed, varying with the current and voltage. Herein, of course, lies the mathematical complexity of the problem. The three regions will be discussed separately:

2.1 Region I ($0 \leq x \leq x_1$)

This region is characterized by local neutrality,

$$p - n - N(x) = 0. \qquad [10]$$

This expression replaces the Poisson Equation given in Eq. [4].

Between this base region and the highly doped n+ emitter is a depletion layer. The left-hand edge of region I, $x = 0$, is taken at the base edge of the depletion layer. The density $n(0)$ at $x = 0$ is known from junction theory, given a known emitter doping and voltage across the emitter–base depletion layer. This voltage, added to the voltage from 0 to L, gives the total transistor voltage.

A differential equation in n is obtained by substitution of Eqs. [9] and [10] into Eq. [8],

$$\frac{dn}{dx} = \frac{n\left(\dfrac{J}{eD_n} - \dfrac{dN}{dx}\right) + \dfrac{J}{eD_n} N}{2n + N}. \qquad [11]$$

Eq. [11] is an Abel equation of the second kind[5] and, with $N(x)$ specified, it is readily solved for $n(x)$ on a computer; $p(x)$ is then given by Eq. [10] and $E(x)$ by Eq. [9].

The self-consistency condition on the neglected space charge defining the end of region I is

$$x = x_1: \quad R(x_1) = R_1 = \frac{\epsilon}{e} \frac{(dE/dx_1)}{p_1} = 0.5. \qquad [12]$$

It turns out that the final results are quite insensitive to the particular value of $R = R_1$ used to terminate the base over the range $0.1 \leqslant R_1 \leqslant 1$. At the plane $x = 0$, R is order of magnitudes less than unity.

Eq. [11] serves as the focal point for development of the analytical equations.

2.2 Region II ($x_1 \leqq x \leqq x_2$)

This region is characterized by the domination of drift current over diffusion current, so that Eq. [8] may be approximated by

$$J \simeq e\mu_n nE. \qquad [13]$$

On the other hand, from the characterization in Eq. [12] of the termination plane $x = x_1$, it is clear that space charge cannot be neglected beyond this plane. Thus, we must use the Poisson equation in place of the neutrality condition.

However, because p is negligible in this region (which can be shown using Eq. [9] for p when E has been determined from Eq. [15]), Eq. [4] simplifies to

$$\frac{\epsilon}{e}\frac{dE}{dx} = -n - N(x). \qquad [14]$$

Substitution of Eq. [13] for n in Eq. [14] produces a differential equation in E,

$$\frac{dE}{dx} = -\frac{J}{e\mu_n E} - \frac{e}{\epsilon} N(x). \qquad [15]$$

Like Eq. [11], this is an Abel equation of the second kind, readily solvable by computer.

Note that Eqs. [13], [14], and [15] characterizing this region are identical, for the case $N(x) = \text{constant}$ (positive, negative, or zero), to the equations characterizing one-carrier space-charge-limited current theory (positive constant to the Ohm's-law–square-law transition problem, zero to the perfect insulator problem, and negative constant to the trap-filled-limit problem) under homogeneous conditions, for which solutions are available.[4] For voltage drops across this region exceeding a few $V_T = kT/e$, the neglect of the diffusion current in these problems has been justified by detailed studies.[6]

Region II ends at plane x_2, where, once again, space charge is no longer important,

$$x = x_2; \quad R(x_2) = R_2 = \frac{\epsilon}{e}\frac{|dE/dx_2|}{n_2} = 0.5. \qquad [16]$$

Note that Region II will usually contain the plane x_M of the metallurgical junction between the p and ν regions of the structure.

2.3 Region III ($x_2 \leqq x \leqq L$)

Region III is an ohmic region, i.e., the space charge (ϵ/e) (dE/dx) can be dropped from Eq. [14], giving

$$n \simeq -N(x),$$

or, using Eq. [13],

$$J \simeq -e\mu_n N(x) E, \qquad [17]$$

which determines $E(x)$.

By use of the above theory, a computer calculation has been made for the prototype power transistor illustrated in Fig. 2, namely, one containing an exponential doping profile. Plots of electron (and hole) density and electric field as a function of position at fixed V_{CE} and varying I_C are shown in Figs. 3 and 4, respectively. Details of the computer program used in obtaining these results can be found in the literature.[3]

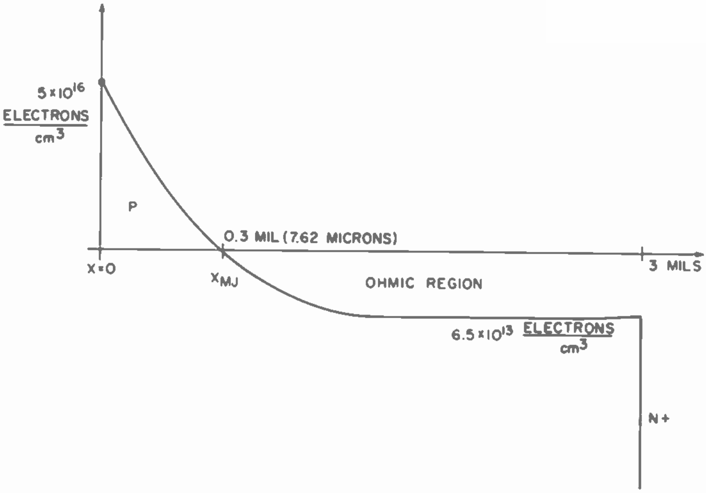

Fig. 2—Doping Profile for n+pνn+ prototype power transistor.

3. Analytical Equations

At this point, equations have been developed that characterize the transistor in the base, transition, and ohmic regions. With these regional equations (Eqs. [11], [15], and [17] in the base, transition, and ohmic regions, respectively) and the computed results shown in Figs. 3 and 4, we will now analyze the device physics further in order to derive additional approximations. We will focus our attention on high-current low-voltage (base-widening) operation. The results obtained using the approximations developed below will be evaluated by comparing them with Figs. 3 and 4.

3.1 Base Region ($0 \leq x \leq x_1$)

We note from Fig. 3 that the curves of electron density as a function of position, for bias conditions under which the base widens beyond

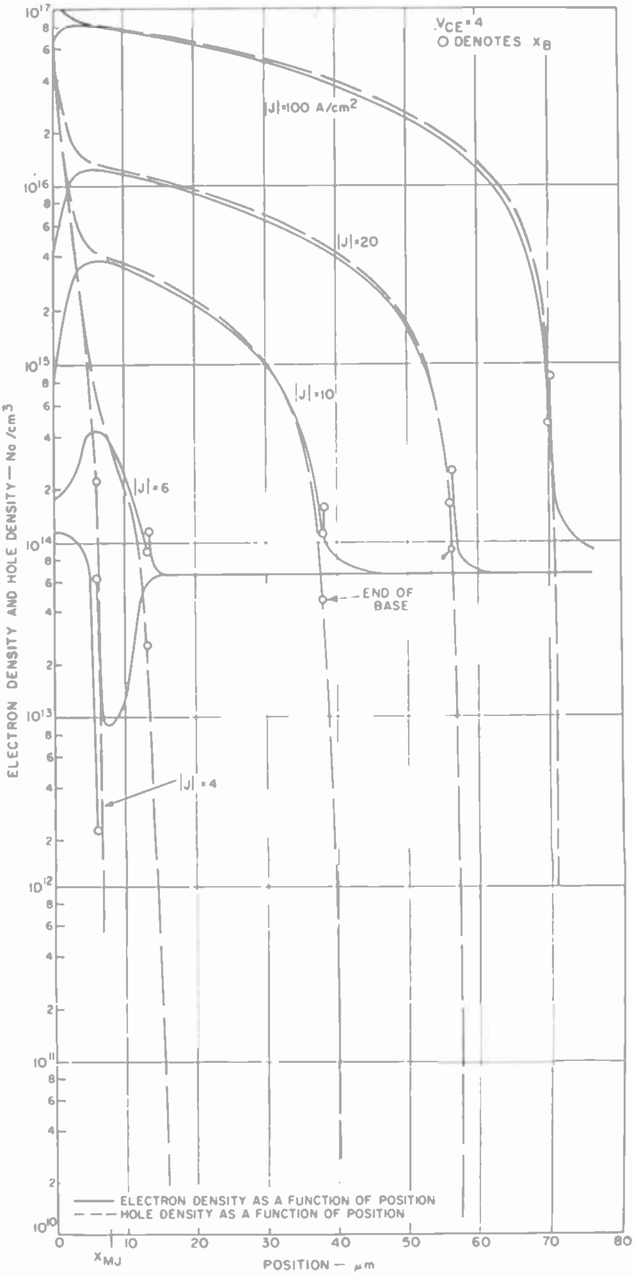

Fig. 3—Electron and hole density versus position at fixed V_{CE} and varying $J(I_C)$.

the metallurgical junction, are characterized by a positive slope, peak, and a negative slope as x increases from zero.

The governing equation in the base region, Eq. [11], is in terms of the electron density and is rewritten here for convenience as follows:

$$(2n+N)\frac{dn}{dx} = +\frac{J}{eD_n}(n+N) - n\frac{dN}{dx}. \qquad [18]$$

One method of simplifying the base region would be to separate the base into $dn/dx > 0$ and $dn/dx < 0$ regions. This procedure corresponds to neglecting the first and second terms on the right-hand side of Eq. [18], respectively (note: J and dN/dx are negative).

Another possibility for simplification is based on comparison of n and N in Eq. [18]. From Fig. 3, we note that within the positive sloping portion of n, $n < N$ is followed by $n > N$ as x increases from zero.

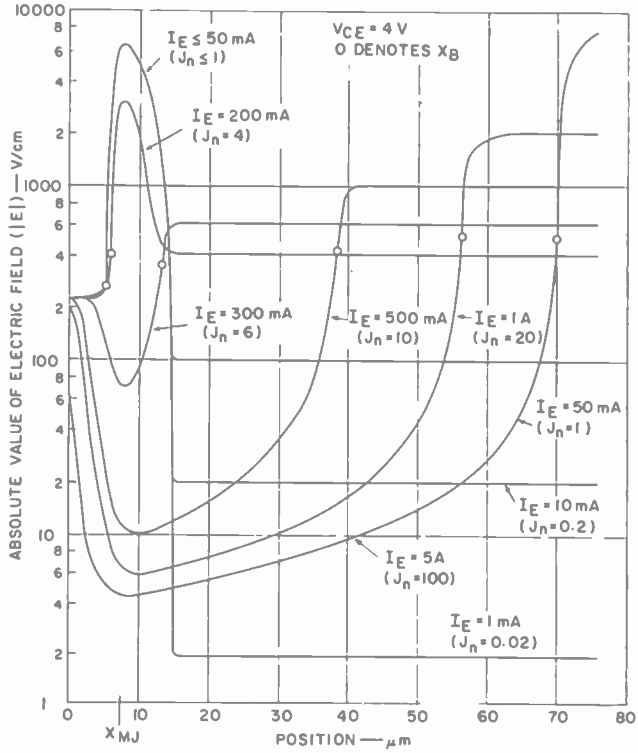

Fig. 4—Electric field versus position at fixed V_{CE} and varying $J(I_C)$.

The above discussion points to two approaches to dividing and simplifying the base, namely $n < N$, $n > N$ and $dn/dx > 0$, $dn/dx < 0$. These approaches are discussed in the following paragraphs.

3.1.1 Base Region Separation ($n < N$ and $n > N$)

Comparison of the electron density with the background doping in Fig. 3 leads to a physical division of the base in terms of $n < N$, $n > N$. Near $x = 0$, $n < N$; beyond some value of x, $n > N$. For very high current densities such as $J = 100$ A/cm², only the region of $n > N$ applies. The base is thereby divided into subregions with a boundary condition of $n = N$ used to join the subregions. Use of $n < N$, $n > N$ in Eq. [18] will lead to analytical equations for $n(x)$ in the subregions.

Considering $n < N$ (or $2n < N$) in Eq. [18] results in

$$N\frac{dn}{dx} = \frac{J}{eD_n}N - n\frac{dN}{dx}, \qquad [19]$$

or

$$\frac{d(nN)}{dx} = \frac{J}{eD_n}N. \qquad [20]$$

Integrating Eq. [20] and solving for n yields

$$n(x) = \frac{1}{N(x)}\left[n(0)N(0) + \frac{J}{eD_n}\int_0^x N(x)\,dx\right]. \qquad [21]$$

Computation of $n(x)$ using Eq. [21] is very simple. Comparison of results obtained using the analytical equations and Eq. [18] will be presented at the conclusion of the analytical discussion.

For $n > N$ in Eq. [18],

$$\frac{dn}{dx} = \frac{J}{2eD_n} - \frac{1}{2}\frac{dN}{dx}. \qquad [22]$$

Eq. [22] is very interesting in that it approaches the Webster equation as dN/dx approaches zero. Because J and dN/dx are both negative, it is determined from the right-hand side of Eq. [22] that the dN/dx term produces the positive slope and J term produces the negative slope in the electron density. As x increases beyond x_{MJ}, dN/dx approaches zero, forcing the slope in the electron density to become negative and constant (this is not evident in Fig. 3 because a semi-log drawing is used).

Solution of Eq. [22] for $n(x)$ gives

$$n(x) = n(x') + \frac{J}{2eD_n}(x - x') - \frac{1}{2}[N(x) - N(x')], \qquad [23]$$

where x' represents the plane where $n = N$.

The importance of Eqs. [21] and [23] for simplicity in obtaining $n(x)$ analytically is evident.

The importance of Eqs. [19] and [22] goes beyond the non-time-varying calculation of $n(x)$, in that they also provide the starting point for the development of a "linearized" Linvill lumped model.[7] This work is in its early stages and, therefore, will only be discussed briefly here. Solution of Eq. [19] for J gives

$$J = eD_n \frac{dn}{dx} + \left[\frac{eD_n \dfrac{dN}{dx}}{N}\right] n \text{ for } n < N. \qquad [24]$$

In the Linvill lumped approach to modeling, the key variable is the minority carrier density, n, and Eq. [24] is *linear* in n. The major drawback in the Linvill lumped approach regarding computation is that the drift term in the current equation is nonlinear, containing the product on n and E. Use of the approach outlined above to derive Eq. [24] removes the drawback of nonlinearity. The first term on the right-hand side of Eq. [24] represents the Linvill "diffusance" element. The second term represents a position-dependent conductance (because n behaves as potential in the Linvill scheme).

Rewriting Eq. [22] to solve for J, yields

$$J = 2eD_n \frac{dn}{dx} + eD_n \frac{dN}{dx} \qquad \text{for } n > N. \qquad [25]$$

Eq. [25] is linear in n with the first term on the right-hand side being the "diffusance" with D_n replaced by $2D_n$ and the second term representing a position-dependent current source.

The Linvill lumped elements given by Eqs. [24] and [25], together with the Linvill recombinance and storage elements, represent a major simplification in transistor modeling. The transistor circuit model corresponding to the above is obtained as follows: Linvill circuit elements corresponding to Eq. [24] are used from $x = 0$ to $x = x'$; Linvill circuit elements corresponding to Eq. [25] are used from $x = x'$ to $x = x_1$; and an ohmic region represented by a resistor is used from $x = x_1$ to $x = L$. The fact that Eqs. [24] and [25] were obtained under non-time-varying conditions may constrain these results to "quasi-time-varying" models. The ability of this approach to translate non-time-varying to time-varying conditions depends on dynamic monitoring of the subregion $n < N$, $n > N$ interface where $n = N$.

Transistor models that are presently in use, such as Ebers–Moll[8] and Gummel charge control,[9] are also based on static conditions. A further limitaton of these approaches is that the time-varying nature of the model is described only by external capacitances. In the "Regionalized" Linvill model suggested above, the time-varying parameters are internal, i.e., recombination and storage and the charge density are treated "quasi-dynamically".

Although Eqs. [21] and [23] yield a complete analytical description for $n(x)$, other alternatives, brought about by defining subregions based on $dn/dx > 0$, $dn/dx < 0$, will also be considered.

3.1.2 Base Region Separation—$dn/dx > 0$, $dn/dx < 0$

a. $dn/dx > 0$, $0 \leqslant x \leqslant x_p$

In the region of $x = 0$ the slope of the electron density is positive as shown in Fig. 3. Therefore, a subregion is defined from $x = 0$ to the plane in x, defined as x peak, where dn/dx equals zero; it is assumed that the second term on the right-hand side of Eq. [18] dominates in this subregion. The governing equation obtained from Eq. [18] is

$$(2n + N)\frac{dn}{dx} = -n\frac{dN}{dx}, \qquad [26]$$

with solution

$$n^2 + nN = (\text{constant}) = n^2(0) + n(0)N(0), \qquad [27]$$

or

$$n(x) = -\frac{N(x)}{2} + \sqrt{\left(\frac{N(x)}{2}\right)^2 + K}. \qquad [28]$$

Additional simplification of Eqs. [26] through [28] results if $n < N$, $n > N$ are considered. Thus, for $n < N$,

$$nN = K \text{ (constant)} = n(o)N(o), \tag{29}$$

and for $n > N$

$$n = K \text{ (constant)}. \tag{30}$$

The value of K in Eq. [30] serves as an upper limit for n peak.

It appears that the results given by Eqs. [26] through [30] are independent of J. This is not the case, because $n(0)$ is uniquely determined by J for a given value of V_{CB}.

b. Location of $dn/dx = 0$ Plane

Having solved for $n(x)$ under the condition that $dn/dx > 0$, we next consider the termination of this subregion at $x \equiv x_p$ where $dn/dx = 0$. Eq. [18] then yields

$$\frac{J}{eD_n}(n+N) = n\frac{dN}{dx} \qquad \text{at } x = x_p. \tag{31}$$

It is evident from Fig. 3 that at x_p, $n \gg N$. Using this result in Eq. [31] yields

$$\frac{J}{eD_n} = \frac{dN}{dx} \qquad \text{at } x = x_p. \tag{32}$$

Eq. [32] accurately locates x_p.

c. $dn/dx < 0$, $x_p \leqslant x \leqslant x_1$ The Webster Region[10]

An often used equation in transistor physics is

$$J = 2\,eD_n\frac{dn}{dx}. \tag{33}$$

This equation results when $n \simeq p \gg N$ in a region of the device where $N =$ constant. The result for these conditions is evidenced in Eq. [22].

In many treatments of transistor analyses, Eq. [33] is assumed to hold throughout the base region from $x = 0$ to $x = x_{MJ}$ (the base is assumed to terminate at x_{MJ} — no base widening). It is clear from

Fig. 3 that Eq. [33] does not hold near or at $x = 0$ under general conditions. We will now show that Eq. [33] is a good approximation in the base subregion where $dn/dx < 0$.

For $dn/dx < 0$, Eq. [18] is used with the first term on the right-hand side dominant, which results in

$$J = eD_n \left(\frac{2n + N}{n + N} \right) \frac{dn}{dx}. \qquad [34]$$

The Webster equation is obtained from Eq. [34] by noting that $n \gg N$ in the region of Fig. 3 where $dn/dx < 0$.

Solving Eq. [33] for $n(x)$ results in

$$n(x) = \frac{J}{2eD_n} (x - x_p) + n_p, \qquad [35]$$

where x_p, the location of the peak in the $n(x)$ curve, is found from Eq. [32] and n_p, the peak value of $n(x)$, is found from Eq. [28].

d. Webster Equation Correction

In the vicinity of x_1, $n \simeq |N|$ and Eq. [35] becomes less accurate. Additional accuracy can be obtained from Eq. [34]. Near x_1, it is noted in Fig. 3 that $N \simeq -N_C =$ constant, where N_C is the ohmic collector concentration. Under this condition, Eq. [34] becomes

$$J = eD_n \left(\frac{2n - N_C}{n - N_C} \right) \frac{dn}{dx}. \qquad [36]$$

If we write the bracketed term in Eq. [36] as $[2 + N_C/(n - N_C)]$, integration becomes simplified,

$$n(x) = n_p + \frac{J}{2eD_n} (x - x_p) + \frac{N_C}{2} \ln \left[\frac{n_p - N_C}{n - N_C} \right]. \qquad [37]$$

At first glance Eq. [37] appears complex regarding determination of $n(x)$. However, the first two terms on the right-hand side are identical to $n(x)$ given by Eq. [35]. The log term is, therefore, a correction factor that can be calculated using the value of $n(x)$ obtained from Eq. [35]. With a computer, very accurate results can be obtained quickly from Eqs. [35] and [37].

3.1.3 Exponential Profile

Due to the unique property of the exponential profile $(dN/dx \propto N)$, additional simplifications result. As an example Eq. [19] can be rewritten

$$\frac{dn}{dx} = \frac{J}{eD_n} - n\left[\frac{dN/dx}{N}\right]. \qquad [38]$$

If we assume $N \propto e^{-x\lambda}$, we have $(dN/dx)/N = -1/\lambda$, resulting in

$$\frac{dn}{dx} = \frac{J}{eD_n} + \frac{n}{\lambda}. \qquad [39]$$

Eq. [39] is a first-order linear differential equation with solution

$$n(x) = n(0)e^{x/\lambda} + \frac{J\lambda}{eD_n}(e^{x/\lambda} - 1)\ . \qquad [40]$$

Near $x = 0$ where $dn/dx > 0$, the second term on the right-hand side of Eq. [39] dominates, resulting in

$$n(x) = n(0)e^{x/\lambda}, \qquad [41]$$

which is equivalent to Eq. [29]. Eq. [41] works well as an upper bound on $n(x)$. Use of the exponential profile results in a position-independent Linvill conductance term in Eq. [24].

3.1.4 Onset of Base Widening

Eq. [39] was developed from Eq. [19] and is based on $n < N$ and $N \propto e^{-x/\lambda}$ or $(dN/dx)/N \simeq -1/\lambda$. We note from Fig. 3 that both the 4 and 6 A/cm² curves, in the vicinity of $x = 0$, are characterized by $n < N$. The profile used to develop Fig. 3, shown in Fig. 2, is given by

$$N(x) = N(0)e^{-x/\lambda} - N_C(1 - e^{-x/\lambda}). \qquad [42]$$

However, as shown in Fig. 2, $N(o) \gg N_C$, resulting in $(dN/dx)/N \simeq -1/\lambda$.

From the above discussion it is anticipated that both the 4 and 6 A/cm² curves can be described by Eq. [39]. The significance attached to this description is that the 4 A/cm^2 curve is pre-base-widening, and the 6 A/cm^2 curve is in base widening. Eq. [39], therefore, must contain the factors determining the onset of base widening. The sensitivity involved in choosing $n(0)$ at a given J (near onset of base widening) to obtain $V_{CE} = 4$ volts is very apparent in Fig. 3. The simple result developed below from Eq. [39] to describe the onset of base widening, therefore, is very useful.

Several interesting effects occur during the onset of base widening as shown in Fig. 3. For example, the slope of n at the origin changes sign from negative to positive as the current density increases from 4 to 6 A/cm^2. Intuition suggests, therefore, that the onset of base widening be determined where $dn/dx = 0$. Setting $dn/dx = 0$ in Eq. [39] results in

$$n(0) = \frac{\lambda}{eD_n} |J|. \qquad [43]$$

Eq. [43] accurately determines $n(0)$ as a function of J for the onset of base widening.

3.2 Transition and Ohmic Collector Regions

The termination of the base region under conditions of base widening occurs where the profile is constant (see Figs. 2 and 3). Analytical treatment is carried out, therefore, using the results of the problem of the "trap-free solid with thermal free carriers," as outlined below.[4] This problem is treated in two regions which coincide with the transition and ohmic regions used in the regional approximation method. The applicable equations are Eqs. [13] and [14], rewritten here for convenience as

$$J \simeq e\mu_n nE \qquad [44]$$

$$\frac{\epsilon}{e}\frac{dE}{dx} = -n + N_c \qquad [45]$$

where $n(x) = -N_C$ in the region of interest. The transition and ohmic regions are characterized as follows:

(a) Transition region ($x_1 \leqslant x \leqslant x_2$) $- N_c$ neglected

$$J \simeq e\mu_n nE \qquad [46]$$

$$\frac{\epsilon}{e}\frac{dE}{dx} = -n \qquad [47]$$

(b) Ohmic region $(x_2 \leqslant x \leqslant L) - n(x) = N_c$

$$J \simeq e\mu_n N_c E. \qquad [48]$$

The plane connecting the two regions is characterized by

$$n(x_2) = N_c, \qquad [49]$$

and the solutions are joined by requiring continuity of the electric field intensity:

$$E(x_2^-) = E(x_2^+). \qquad [50]$$

Solution of the electric-field intensity by use of Eqs. [46] and [47] results in

$$E(x) = \sqrt{\left(\frac{-2J}{\epsilon\mu_n}\right)x + C} \qquad [51]$$

where C is determined by matching the electric field at $x = x_1$ using Eq. [51] together with the value obtained from the solution in the base region evaluated at x_1.

The electric field solution in the ohmic collector, obtained directly from Eq. [48], is

$$E(x) = \frac{J}{e\mu_n N_c}. \qquad [52]$$

4. Comparison of Analytical and Regional Approximation Techinques

To compare the results of the analytical and regional approximation method (RAM) techniques and to demonstrate the application of the analytical scheme a complete determination of a typical curve in Fig. 3 will be carried out.

We begin with a discussion of how the curves in Figs. 3 and 4 were generated using RAM since the procedure used for the analytical technique is obtained in a similar manner. Starting at $x = 0$, Eq. [11] is used subject to a boundary condition on the electron density at $x = 0$. The value of $n(0)$ chosen for a given J determines the general shape of the electron-density curves shown in Fig. 3 and the electric field curves shown in Fig. 4. The value of $n(0)$, therefore, determines the voltage V_{CE} for a given J (the voltage V_{CE} is obtained by adding the emitter-to-base junction voltage, which depends on $n(0)$, to the applied voltage between $x=0$ and $x=L$). The value $n(0)$ itself is not significant. The important item to consider when comparing the RAM and analytical techniques is that, for the same V_{CE} and J, equivalent curves of $n(x)$ and $E(x)$ result. This will become clear below.

Eq. [11] subject to $n(0)$ and J, is solved from $x=0$ to x_1, which is determined through Eq. [12]. At x_1 Eq. [15] takes over, subject to continuity of the electric field at x_1. Eq. [15] is used up to $x=x_2$, which is determined through Eq. [16]. From x_2 to L, Eq. [17] applies, subject to continuity of the electric field at $x=x_2$.

To demonstrate the application of the analytical approach, Eqs. [21] and [23] will be used in the base region. These equations are chosen because they lend themselves to device modeling through the Linvill approach, as discussed previously. In addition, the exponential profile of Fig. 2 will be used, resulting in a linearized drift term in the Linvill model as given by Eqs. [24] and [25].

4.1 Base Region

If we begin at $x=0$, with Eq. [21] subject to an exponential profile, we obtain Eq. [40], which is rewritten here for convenience.

$$n(x) = n(0)e^{x/\lambda} + \frac{J\lambda}{eD_n}(e^{x/\lambda} - 1). \qquad [53]$$

We will consider the curves in Figs. 3 and 4 for $J = 20$ A/cm². A value of $n(0) = 2.0 \times 10^{15}$ will be chosen. Note that this is not the value of $n(0)$ used to obtain the $J = 20$ curve in Fig. 3, indicating a small error in $n(x)$ near $x=0$. This error is of little consequence because the main objective will still be met, that of obtaining equivalent curves of $n(x)$ and $E(x)$ over most of the structure for given values of V_{CE} and J. The value of $n(0) = 2.0 \times 10^{-15}$ was chosen to get a reasonably close fit to the $J = 20$ curve in Fig. 3. With $\lambda = 1.1 \times 10^{-4}$ cm (from Fig. 2) and $D_n = 25$ (value used in obtaining Fig. 3 and 4), Eq. [53] becomes

$$n(x) = 2 \times 10^{15} e^{x/\lambda} - 5.5 \times 10^{14}(e^{x/\lambda} - 1) \text{ for } 0 \leqslant x \leqslant x' \qquad [54]$$

Eq. [54] is used until $x = x'$ where $n(x') \simeq (2/3)N(x')$. (The original development in Section 3 used $n = N$ as the boundary. However, due to the term $(2n + N)$ in Eq. [18], from which Eq. [21]

was obtained, a more consistent boundary is obtained between $n = N/2$ and $n = N$).

For the present calculation, $x' = 1.5\lambda$ and $n(x') = 7.05 \times 10^{15}$ were used. Eq. [23] then becomes

$$
\begin{aligned}
n(x) &= n(x') - 2.5 \times 10^{18}\,(x - x') \\
&\quad -2.5 \times 10^{16}\,(e^{-x/\lambda} - e^{-x'/\lambda})
\end{aligned}
\qquad [55]
$$

for $x' \leqslant x \leqslant x_1$.

The location of x_1 is obtained using Eq. [12], requiring

$$
\frac{\epsilon}{e}\left|\frac{(dE/dx)_1}{p_1}\right| = 0.5. \qquad [56]
$$

To obtain the condition given in Eq. [56] in terms of the electron density, which together with Eq. [55] locates x_1, we must first obtain an analytical equation for the electric field.

4.1.1 Electric Field Equation

In the portion of the base bounded by $0 \leqslant x \leqslant x'$, Eq. [39] applies, which is equivalent to the electric field being constant and equal to

$$
E = \frac{-D_n}{\mu_n}\frac{1}{\lambda} = -\frac{V_T}{\lambda}. \qquad [57]
$$

For the present analysis, this represents a field of -227 V/cm.

Eq. [25] represents the current flow in the portion of the base bounded by $x' \leqslant x \leqslant x_1$. Rewriting Eq. [25] to obtain the electric field gives

$$
J = eD_n\frac{dn}{dx} + \left[\frac{V_T}{n}\left(\frac{dn}{dx} + \frac{dN}{dx}\right)\right] ne\mu_n. \qquad [58]
$$

The term in brackets in Eq. [58] is equal to $E(x)$. Thus, removal of the quantity dn/dx by use of Eq. [25] results in

$$
E(x) = \frac{V_T}{n}\left[\frac{J}{2eD_n} + \frac{1}{2}\frac{dN}{dx}\right]. \qquad [59]
$$

4.1.2 Location of x_1

It is evident from Fig. 3 that the location of x_1 occurs where the doping $N(x)$ is approximately constant. Calculation substantiates that

$$J/eD_n \gg dN/dx.$$

Thus, simplification of Eq. [59] in the vicinity of x_1 yields

$$E(x) \simeq \frac{V_T}{n} \frac{J}{2eD_n}. \qquad [60]$$

Use of Eq. [60] in Eq. [56], yields

$$n^2 (n + N) = \frac{\epsilon V_T}{2e} \frac{J}{eD_n}^2 \qquad [61]$$

where $dn/dx \simeq J/(2eD_n)$ was utilized.

For $J = 20$ A/cm² and a value of $\epsilon_r = 11.7$, Eq. [61] results in $n(x_1) = 1.55 \times 10^{14}$. With $n(x_1)$ known, x_1 can be found from Eq. [55]. Because $x_1 \gg x$, the term $e^{-x/\lambda}$ in Eq. [55] can be neglected at $x = x_1$. Substitution of $n(x_1) = 1.55 \times 10^{14}$, $x' = 1.5\lambda$, and $n(x') = 7.05 \times 10^{15}$ into Eq. [55] yields $x_1 = 47\lambda = 51.7$ micrometers.

4.2 Transition and Ohmic Regions

In the transition region, Eq. [51] is used for the electric field. A slight variation of Eq. [51] used for ease of computation is

$$|E(x)| = \sqrt{\frac{2|J|}{\epsilon\mu_n}(x - x_1) + [E(x_1)]^2} \qquad [62]$$

Use of Eq. [60] with $n(x_1) = 1.55 \times 10^{14}$ yields $E(x_1) = 419$ V/cm. With $|J| = 20$ A/cm², Eq. [62] becomes

$$|E(x)| = \sqrt{4.26 \times 10^6 (x - x_1) + 1.76 \times 10^5} \qquad [63]$$

where $(x - x_1)$ is in units of λ.

Eq. [63] is valid for $x' \leqslant x \leqslant x_2$ where x_2 is defined by Eq. [49], requiring $n(x_2) = N_c$. The location of x_2 is found by substituting Eq. [63] into Eq. [46].

The ohmic region holds for $x_2 \leqslant x \leqslant L$ with $n_{\text{ohmic}} = N_c$ and $|E_{\text{ohmic}}| = |J|/e\mu_n N_c = 2000$ V/cm.

The results obtained from Eqs. [53] through [63] for $|J| = 20$ A/cm^2 and $n(0) = 2 \times 10^{15}$ are shown in Figs. 5 and 6 for the electron density and electric field, respectively. Also included are similar computations for $n(0) = 2.5 \times 10^{15}$.

Agreement between computer and analytical techniques in Figs. 5 and 6 is very close. It is evident that for a given $J - V_{CB}$ operating point, the electron density and electric field profiles obtained through computer or analytical techniques are, for all practical considerations, identical. The approximations used to obtain the analytical equations,

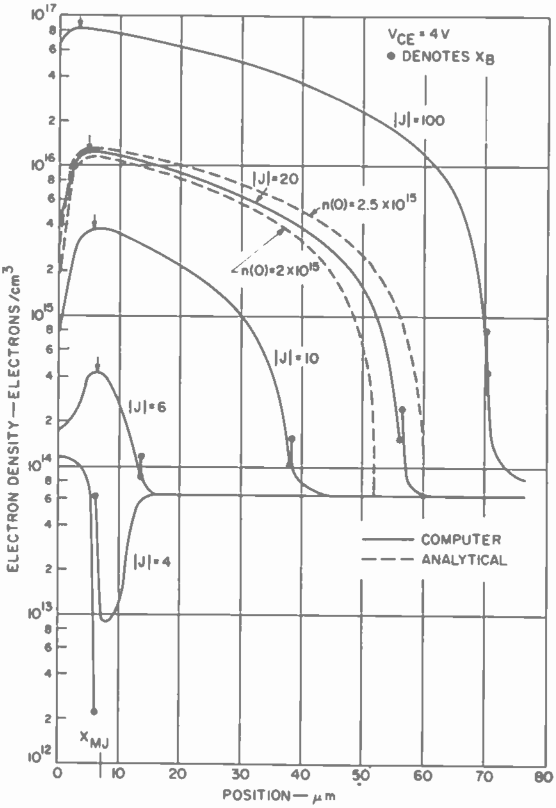

Fig. 5—Electron density versus position, analytical and computer results.

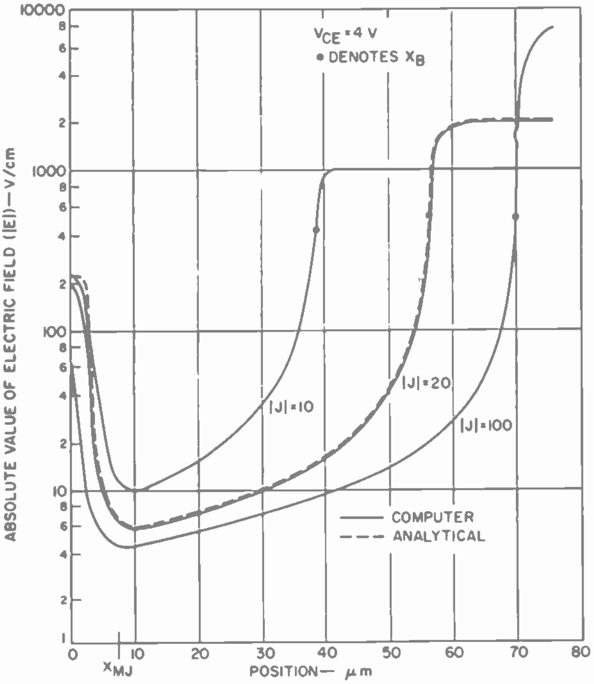

Fig. 6—Electric field versus position, analytical and computer results.

therefore, are justified. In addition, the analytical equations can now be used with confidence to develop simplified yet accurate models for determining transistor behavior.

5. Dominant Region Technique

In the previous sections, we developed the complete analytical approach for determining electron density and electric field profiles throughout the transistor. Under certain operating conditions, however, portions of the transistor have negligible effect on performance. For example, under extreme base-widening conditions, practically all of V_{CB} is dropped across a small region near the collector. Taking advantage of these situations leads to significantly simplified, yet highly accurate results. In this section, this "Dominant Region" technique is described. Two very important results in transistor behavior developed using this technique are discussed. The results presented below were brought to light through use of the regional approximation method.

5.1 Base-Widened Transit Time

In the classical approach to transit-time calculations, the electron density in an n-p-n transistor is assumed to vary in the base as shown in Fig. 7. The base transit time T_B is then found as the ratio of the total base charge to the electron current density,

$$T_B = \frac{Q_B}{J} = \frac{(1/2)W_B en(0)}{eD_n \dfrac{n(0)}{W_B}} = \frac{W_B{}^2}{2D_n}. \qquad [64]$$

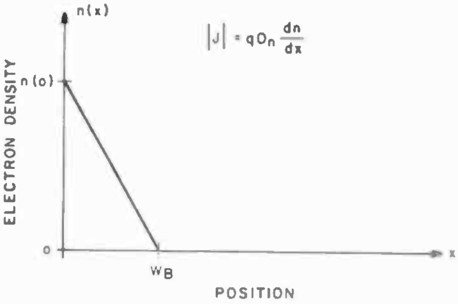

Fig. 7—Electron density versus position for low-level injection.

Two assumptions are inherent in Eq. [64]:

1. Only diffusion current is present, resulting in the profile in Fig. 7.
2. Electron density is zero at fixed base width W_B (no base widening) for all operating conditions (i.e., I_C, V_{CE}).

These assumptions, however, are unrealistic under general operating conditions.

Another variation of the transit-time calculation which includes drift current and conductivity modulation is obtained using Eqs. [1] and [9] with $p \simeq n$, resulting in

$$J = 2eD_n \frac{dn}{dx}. \qquad [65]$$

The classical approximation of $n(W_B) = 0$ (no base widening) is again assumed, yielding

$$T_B = \frac{W_B^2}{4D_n}. \qquad [66]$$

Use of Eq. [64] or Eq. [66] to calculate base transit time under conditions of base widening leads to useless results. What is required is calculation of the transit time that considers the specific current and voltage at which the device operates. For the device shown in Fig. 2 with $V_{CE} = 4$ volts and varying current density, the computer calculations of transit time shown in Fig. 8 were obtained by dividing the total electron base charge shown in Fig. 3 by the electron current density.

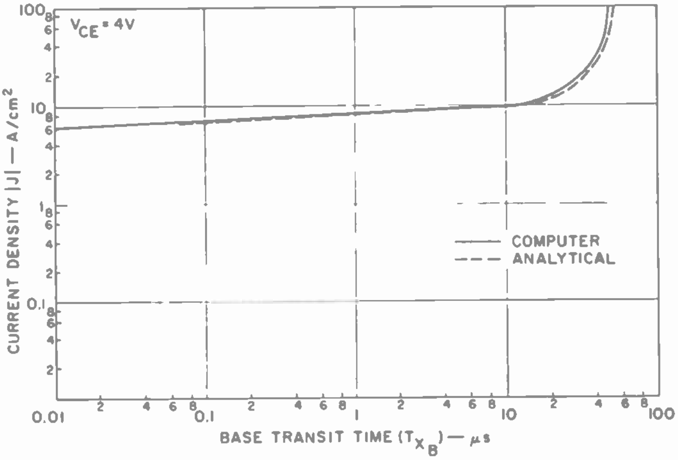

Fig. 8—Transit time versus current density, analytical and computer results.

Rather than discard the form of the transit time formula given in Eqs. [64] and [66], a reinterpretation is presented for base-widened operation. We replace the fixed quantity W_B by the effective base width W_B (I_C, V_{CE}) to obtain

$$T_B (I_C, V_{CE}) = [W_B (I_C, V_{CE})]^2/(\eta D_n). \qquad [67]$$

where η is a factor to be determined.

The use of Eq. [67] at $J = 20$ A/cm² ($V_{CE} = 4$ volts) with W_B equal to 56.2 micrometers (Fig. 3), results in $\eta D_n = 104$. Since $D_n = 25$ was used in the computed calculation,

$$\eta \text{ (effective)} \simeq 4. \qquad [68]$$

It is reasonable that $\eta = 4$ under base-widening conditions because, over most of the structure, the Webster equation (D_n replaced by $2D_n$) governs the solution, i.e., p approximately equals n.

Eq. [67], therefore, gives reasonable values of base transit time under general operating conditions if η is equal to 4 and $W_B(I_C, V_{CE})$ is interpreted as the effective base. The remaining quantity to determine is $W_B(I_C, V_{CE})$. It is evident in Fig. 4 that, for $|J|$ greater than 6 A/cm², a major portion of V_{CE} is carried in the ohmic region where $|J|$ is equal to $q\mu_n N_c |E|$, resulting in

$$V_{CE} = \frac{|J|}{e\mu_n N_c}(L - W_B), \qquad [69]$$

or

$$W_B = L - \frac{V_{CE}(e\mu_n N_c)}{|J|}. \qquad [70]$$

For the transistor structure of Fig. 2, Eq. [70] becomes

$$W_B(\text{micrometers}) = 76 - \frac{100 V_{CE}}{|J|}. \qquad [71]$$

By use of Eqs. [67] and [71] with $\eta = 4$ and $D_n = 25$, data for transit time was generated as indicated by the dashed curve in Fig. 8. Comparison of computer-generated data and data obtained using Eqs. [67] and [71] indicates very close agreement. For $|J| = 6$ A/cm², i.e., at the onset of base widening, agreement is not as close.

Clarification is needed concerning the use of a single value of D_n for a general comparison of both the computer and analytical methods. By use of the analytical method, Eq. [69], it can be seen that T_B varies directly as D_n^{-1}. The computer method of calculating T_B is to divide the total base charge by J,

$$T_B = \frac{\left[q \int_0^{W_B} n(x)\,dx \right]}{J}$$

Thus, for both results to be independent of D_n, it is necessary for $n(x)$ to vary directly as D_n^{-1}, a condition that is true over the portion of the base where the Webster equation holds. This condition is shown in Fig. 3 to include most of the base. The reason for the discrepancy between computer and analytical results at $|J| = 6$ A/cm^2 is that, at the onset of base widening, only half the base is Webster-like.

5.2 High-Field Region Under Severe Base Widening

Destructive second breakdown in high-power transistors has been attributed to high fields in the vicinity of the collector metallization during high-current low-voltage operation, i.e., when the device is operating under severely base-widened conditions. Our purpose here is to analytically characterize the high-electric-field region in the collector under such conditions.

5.2.1 Constant Mobility

It is evident from Fig. 4 that as the current increases at fixed V_{CE}, the ohmic region shrinks. For $J \leqslant 20$ A/cm^2, the ohmic region is significant in that a major portion of V_{CE} is dropped across it. For $J \geqslant$ A/cm^2, two physical effects become evident. First, the electric field becomes very large in the region of the collector; second, most of V_{CE} is dropped in the high-field region to the right of the effective base (denoted by a small circle). It is this high-field region that is considered below.

In the high-field region, Eqs. [46] and [47] apply, resulting in

$$|E| = \sqrt{\frac{-2J}{\epsilon\mu_n}(x - x_1) + E(x_1)}. \qquad [72]$$

From Fig. 4 we note that as J increases beyond 100 A/cm^2, the effect of $E(x_1)$ on E in the high-field region diminishes. Therefore, it will be assumed that $E(x_1) \simeq 0$, resulting in

$$|E| = \sqrt{\frac{-2J}{\epsilon\mu_n}}\,(x - x_1)^{1/2}. \qquad [73]$$

Because almost all of V_{CE} appears across the high-field region, we can write

$$V_{CE} \simeq \int_{x_B}^{L} |E|\,dx,$$

or

$$V_{CE} = \sqrt{\frac{8}{9}\frac{J}{\epsilon\mu_\eta}}\,[L - x_1]^{3/2}. \qquad [74]$$

The technique of finding $E(x)$ for a given operating condition is based on Eqs. [73] and [74] as follows. Given V_{CE} and J, x_1 is found from Eq. [74]. With x_1 and J known, Eq. [73] is used to find $E(x)$.

(a) *Analytical Results*

Comparisons of $E(x)$ obtained using Eqs. [73] and [74] with the computer results in Fig. 4 are shown in Fig. 9 for $J = 100$, 250, and 1000 A/cm², respectively. $V_{CE} = 4$ volts was used in each case and a constant

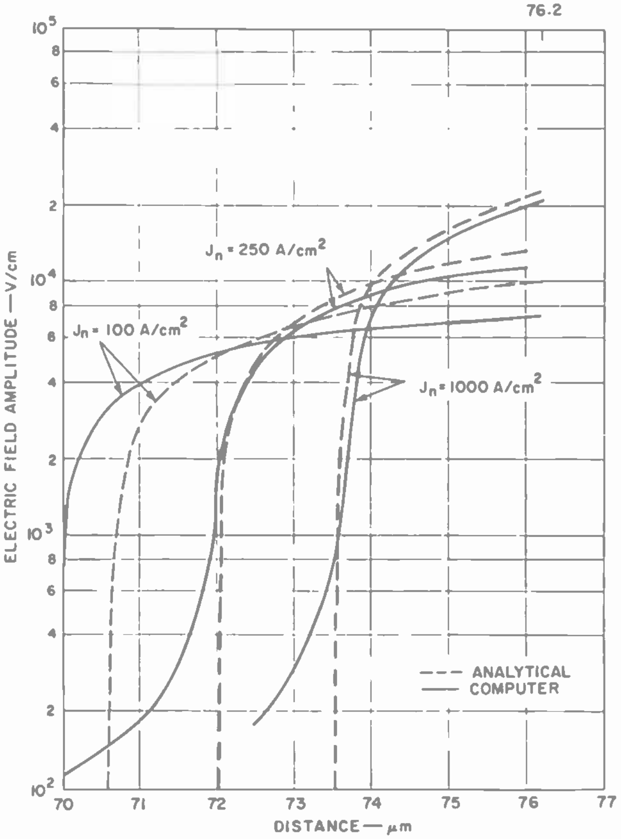

Fig. 9—Electric field versus position under severe base widening, analytical and computer results at $J = 100$, 250, and 1000 A/cm².

mobility of 1000 was assumed. Fig. 9 represents an expanded version of the high-field region of Fig. 4. It is evident that as J is increased, the accuracy is improved. The approximations used, namely, the negligible effect of $E(x_1)$ on the high-field region and V_{CE} being mainly taken up by the high-field region, are thereby verified. These conditions necessitate agreement between analytical and computer results for any velocity-field characteristic, assuming such a characteristic does not significantly alter the general features of the field profile upon which this method is based.

(b) *Constraints*

In the derivation of Eqs. [73] and [74], it is assumed, in addition to the normal regional approximations, that the background concentration, N_c, can be neglected in Poisson's equation (see Eq. [45]). It is required, therefore, that the minimum density, $n_{\min}$, satisfy the condition

$$n_{\min} > N_c. \qquad [75]$$

Eq. [46] requires that the minimum density occur at $x = L$, the location of the maximum field. By use of Eqs. [46], [73], and [74], we can write the condition [75]

$$|J| > \left(\frac{3e^3 N_c{}^3 \mu_n{}^2 V_{CE}}{\epsilon}\right)^{1/2}. \qquad [76]$$

For the device under study ($N_c = 6.5 \times 10^{13}$) operating at $V_{CE} = 4$ volts, Eq. [76] yields $|J| > 115$ A/cm^2. For $|J| = 250$ and 1000 A/cm^2, the values of $n_{\min} = 1.1 \times 10^{14}$ and 2.76×10^{14}, respectively, indicate satisfaction of the constraint given in Eq. [75]. Note that the error in the analytical approach is rather small even at 100 A/cm^2, because the electron density is greater than the background through most of the region of interest. Thus, the constraint given by Eq. [75] is more stringent than necessary and implies that the solution is certainly good. If Eq. [75] is not satisfied, a more accurate analysis is required.

5.2.2 Field-Dependent Mobility

This situation is analyzed using a "piecewise" linear approximation to the velocity-field characteristic. In this work, the following approximation is used for electrons in silicon:

region I, $x_1 \leqslant x \leqslant x_h$

$$v = \mu_h E$$

where $\mu_h = 1000$ cm²/V-sec and $E(x_h) = E_h = 3000$ V/cm;

region II, $x_h \leqslant x \leqslant x_l$

$$v = (\mu_h - \mu_l)\ E_h + \mu_l E$$

where $\mu_l = 455$ cm²/V-sec and $E(x_l) = E_l = 14{,}500$ V/cm;

region III, $x_l \leqslant x \leqslant L$

$$\mathrm{v} = v_s = 8.24 \times 10^6 \text{ cm/sec.}$$

In region I, the solution is identical to that in the constant mobility case; thus,

$$|E| = \sqrt{\frac{-2J}{\epsilon\mu_h}}\,(x - x_1)^{1/2} \qquad [77]$$

and

$$V_1 = \int_{x_1}^{x_h} E\,dx = \sqrt{\frac{8}{9}\frac{J}{\epsilon\mu_h}}\,(x_h - x_1)^{3/2} = \frac{\epsilon\mu_h E_h{}^3}{3J}. \qquad [78]$$

In region II, Poisson's equation becomes

$$\frac{\epsilon}{e}\frac{dE}{dx} = \frac{J}{env} = \frac{J}{e[(\mu_h - \mu_l)E_h + \mu_l E]} \qquad [79]$$

Defining $v_o = (\mu_h - \mu_l)E_h$ and integrating yields [80]

$$\frac{\mu_l}{2}(E^2 - E_h{}^2) + v_o(E - E_h) = \frac{J}{\epsilon}(x - x_h). \qquad [81]$$

The voltage across region II is found by substituting $dx = dV/E$ into Eq. [79], resulting in

$$V_2 = \frac{\epsilon v_o}{2J}(E_l{}^2 - E_h{}^2) + \frac{\epsilon\mu_l}{3J}(E_l{}^3 - E_h{}^3). \qquad [82]$$

Region III is characterized by

$$J = env_s. \qquad [83]$$

Poisson's equation is given by

$$\frac{\epsilon}{e}\frac{dE}{dx} = \frac{J}{ev_s}, \qquad [84]$$

or

$$E = E_l + \frac{J}{\epsilon v_s}(x - x_l). \qquad [85]$$

hence,

$$V_3 = E_l(L - x_l) + \frac{J}{2v_s\epsilon}(L - x_l)^2 \qquad [86]$$

Since the total voltage drop ($V_{CE} = V_1 + V_2 + V_3$) and V_1 and V_2, as specified by Eqs. [78] and [80], is given in terms of known quantities, V_3 may be computed. If the sum of V_1 and V_2 is less than V_{CE}, V_3 is positive and Eq. [86] can be used to find x_l. Eq. [81] evaluated at x_l yields the boundary x_h; x_1 can then be determined from Eq. [78]. With specification of the boundaries completed, the fields can be calculated in each region. If the sum of V_1 and V_2 is greater than V_{CE}, region III does not exist. Under this condition Eqs. [81] and [82] are rewritten

$$\frac{\mu_l}{2}(E_L{}^2 - E_h{}^2) + v_o(E_L - E_h) = \frac{J}{\epsilon}(L - x_h) \qquad [87]$$

$$V_2 = \frac{\epsilon v_o}{2J}(E_L{}^2 - E_h{}^2) + \frac{\epsilon\mu_l}{3J}(E_L{}^3 - E_h{}^3). \qquad [88]$$

Because there are only two regions,

$$V_2 = V_{CE} - V_1. \qquad [89]$$

Eq. [88] can be solved for E_L, allowing x_h to be calculated from Eq. [87]. Should Eq. [89] yield $V_2 < 0$, there is only one region, and the problem reduces to the case of constant mobility. It should be obvious that the number of regions and the position of the boundaries are functions of the operating point, i.e., J, V_{CE}. Fig. 10 indicates the effect of inclusion of field-dependent mobility for the device previously analyzed.

A constraint similar to that given for the constant-mobility case must be considered. Because

$$J = qnv, \qquad [90]$$

the maximum velocity must be determined from the field solution and the v-versus-E characteristic and requires that

$$n_{\min} > n_o, \qquad [91]$$

resulting in

$$J > qn_o v_{\max}. \qquad [92]$$

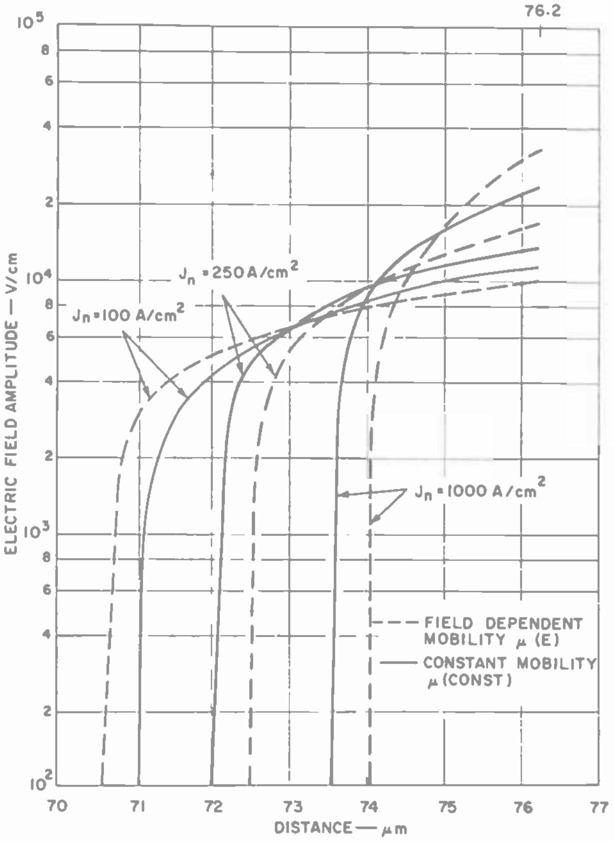

Fig. 10—Electric field versus position; effect of field dependent mobility at $|J| = 100$, 250, and 1000 A/cm^2.

As in the constant-mobility case, this constraint is more stringent than necessary; in some cases, a closer look may result in an easing of the constraint.

6. Conclusions

This paper has shown how the regional approximation technique is used for the development of transistor models. The key to the success of this technique is the interaction of physics and mathematics; the physics is used as a guide to the mathematical approximations. A linearized version of the Linvill lumped model was developed in Section 3. This model is highly useful to both circuit and device designers. The model parameters are simply found from the charge distributions discussed in Sections 2 and 3. Model development using the regional approximation scheme allows for adjustment of the complexity of the model. Section 4 showed how a single region can adequately predict device performance under extreme base-widening conditions.

The success of a device model is judged largely by its capability to represent physical reality with minimum mathematical complexity. As has been shown, such a combination is feasible.

References:

[1] W. Shockley, **Electronics and Holes in Semiconductors,** D. Van Nostrand Co., 1950.

[2] H. K. Gummel, "A Self-Consistent Iterative Scheme for One Dimensional Steady State Transistor Calculations," **IEEE Transactions on Electron Devices,** Vol. ED-11, pp. 455-465, Oct. 1964.

[3] R. B. Schilling, "A Regional Approach for Computer-Aided Transistor Design," Special Issue on Computer Aided Design, **IEEE Transactions,** Vol. E-12, pp. 152-161, 1969.

[4] M. A. Lampert and R. B. Schilling, "Current Injection in Solids: The Regional Approximation Method," **Semiconductors and Semimetal,** Chapter 1, Vol. 6, Academic Press, 1970.

[5] G. M. Murphy, **Ordinary Differential Equations,** D. Van Nostrand Co., Princeton, New Jersey, 1960.

[6] R. B. Schilling and H. Schacter, "Neglecting Diffusion in Space-Charge-Limited Currents," **J. Appl. Phys.,** Vol. 38, No. 2, p. 841, Feb. 1967.

[7] J. G. Linvill, **Models of Transistors and Diodes,** McGraw-Hill Book Company, New York, 1963.

[8] J. J. Ebers and J. L. Moll, "Large-Signal Behaviour of Junction Transistors, **Proc. IRE,** Vol. 43, No. 12, p. 1761, Dec. 1954.

[9] H. K. Gummel and H. C. Poon, "An Integral Charge Control Model of Bipolar Transistors," **Bell System Technical Journal,** Vol. 49, No. 5, p. 827, May-June 1970.

[10] W. M. Webster, "On the Variation of Junction-Transistor Current-Amplification Factor with Emitter Current," **Proc. IRE,** p. 914, June 1954.

[11] P. L. Hower and V. G. K. Reddi, "Avalanche Injection and Second Breakdown In Transistors," **IEEE Transactions on Electron Devices,** Vol. ED-11, p. 320, April 1970.

Small-Signal Theory of a Transit-Time-Negative-Resistance Device Utilizing Injection from a Schottky Barrier

K. P. Weller

RCA Laboratories, Princeton, N. J.

Abstract—A punch-through negative-resistance semiconductor device that utilizes injection from a Schottky barrier and transit delay in a velocity-saturated drift zone is described. A small-signal theory for the microwave impedance of this device is derived, and the result is used to predict the parameters required for optimum operation at a given frequency. The theory is applied to a device incorporating the PtSi-on-silicon Schottky barrier to evaluate the high-frequency operation. The desired barrier properties for microwave and millimeter-wave operation are discussed briefly.

Introduction

A semiconductor diode in which charge carriers injected or generated near one contact drift at saturated velocity to the other collector contact will usually exhibit a negative resistance over some frequency range. The best known device of this type is the avalenche diode proposed by Read.[1] More recently another transit-time device based on carrier injection from a p-n junction into a depleted drift zone was proposed.[2] This device is biased so the depletion region punches through the drift zone to the injecting junction during a portion of the rf voltage swing. Only during this portion of each cycle are carriers injected into the drift zone. Fabrication of this device requires a rather complex triple epitaxial layer structure to ensure that the injected carriers travel at saturated velocity through most of the drift zone.

Recently, Coleman and Sze have reported that a similar punchthrough device, using a Schottky barrier rather than a p-n junction, was fabricated and oscillated in the 4-6 GHz region.[3] The operation of such a device is the subject of this paper. The device, shown in Fig. 1(a), consists of an n-type semiconductor layer of width *W* sandwiched between two Schottky-barrier contacts. Other versions of the device are possible. For example, the Schottky barrier on the right could be replaced by a n-p+ barrier. This junction is used solely to deplete the drift zone of carriers and permit a high electric field to exist near the forward-biased Schottky-barrier interface on the left. The Schottky barrier on the left should not be replaced by a p-n junction, since it is desirable to have a contact that provides limited current injection even under large forward bias. A complementary structure utilizing electron injection from the metal is also conceivable by providing a Schottky-barrier metal with a sufficiently large barrier potential ϕ_{Bp} for holes. The analysis presented here relates to the structure of Fig. 1, but the results are applicable to the other versions with little modification.

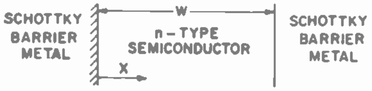

(a) DEVICE STRUCTURE

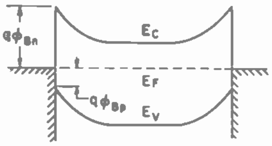

(b) 0-BIAS BAND DIAGRAM

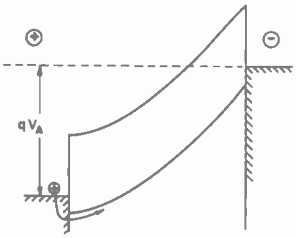

(c) BIASED TO PUNCHTHROUGH

Fig. 1—Device configuration and energy-band diagrams for one version of the Schottky-barrier injection transit time diode.

Small-Signal Analysis

A simplified energy-band diagram of the device is shown in Fig. 1(b). The bending of the conduction-band edge E_c and valence-band edge E_v resulting from the metal–semiconductor contact potential are shown when no bias is applied to the diode. The Fermi level E_F is a constant since the system is in thermal equilibrium. Applying a bias V_A shifts the relative position of the Fermi level in the two metal contacts as shown in Fig. 1(c). For a sufficiently large bias, the semiconductor layer is depleted of majority carriers. The large potential barrier of the reverse-biased contact on the right prevents the flow of majority carriers from the semiconductor to the forward-biased contact on the left. But a significant current density can result from injection into the semiconductor at the forward-biased contact, as illustrated in Fig. 1(c), since the barrier potential is relatively low.

There are two possible bias regions in which this current density will be strongly modulated by an applied rf voltage. These two regions are more clearly discussed in terms of the electric field $\mathcal{E}_b$ at the left metal–semiconductor interface. When the semiconductor layer is completely depleted of carriers, this field is related to the applied voltage by

$$\mathcal{E}_b = \frac{V_A}{W} - \frac{qN_D W}{2\epsilon}, \qquad [1]$$

where ϵ is the static dielectric constant, N_D is the donor density, and q is the electronic charge. One of these bias regions lies between the voltage required for complete depletion of the n-layer and the voltage for $\mathcal{E}_b = 0$ (where $V_A = qN_D W^2/2\epsilon$). In this region, the electric field near the left interface is negative. The effective potential barrier that holes in the metal must overcome to enter the semiconductor is $\phi_{Bp} + \epsilon \mathcal{E}_b{}^2/(2qN_D)$. As the voltage V_A is increased, $|\mathcal{E}_b|$ decreases, thereby lowering the effective barrier potential and enhancing the current. The second and higher bias region requires that $\mathcal{E}_b \gg 0$. In this region, the actual barrier potential ϕ_{Bp} is a function of field. The mechanisms involved in this mode of operation are discussed in more detail later. Because of the uncertainty in the semiconductor layer width, it is not possible to determine from Coleman and Sze's[3] published data the bias region in which their devices oscillated.

Operation in the lower bias region suffers from the same disadvantage as the earlier p-n junction device proposed by Ruegg.[2] The electric field in the drift zone of the semiconductor is very low adjacent to the injecting contact. The carriers do not travel at saturated velocity in this low-field region, but at a field-dependent velocity. Although this mode of operation will result in a negative resistance at the proper frequency, the ultimate high-frequency performance is expected to be poorer than that for operation in the higher bias region. In addition, the analysis is complicated by the existence of a region of field-dependent velocity in the drift zone. The analysis to follow will therefore concentrate on the higher-bias mode of operation, which assumes $V_A > qN_D W^2/2\epsilon$. For this mode of operation, it is desirable to make the semiconductor layer as near intrinsic as possible to reduce the applied voltage required.

The injected current density for $\mathcal{E}_b > 0$ can be expressed as[4]

$$J_b = A^{**}\, T^2 \exp\left\{-\frac{q\phi_{Bp}}{kT}\right\}, \qquad [2]$$

where A^{**} is the effective Richardson constant, T is the junction temperature, and k is Boltzmann's constant. In the analysis it is assumed that A^{**} is not a function of the electric field $\mathcal{E}_b$, but that the barrier height ϕ_{Bp} is. For simplicity, only the image-force barrier-lowering mechanism, or Schottky effect, will be included in the analysis. The modifications required to include other barrier-lowering mechanisms will be discussed briefly following the analysis. The barrier height can be expressed as

$$\phi_{Bp} = \phi_{BO} - \Delta\phi \qquad [3]$$

where ϕ_{BO} is the barrier height when $\mathcal{E}_b = 0$ and

$$\Delta\phi = \sqrt{q\mathcal{E}_b/4\pi\epsilon}.$$

The dielectric constant ϵ of the semiconductor is rather vaguely defined in this expression, but experimental results indicate that using the static value is appropriate.[5]

The expression for injected current at the left-hand side of the drift zone is now used to derive the small-signal impedance of the diode. The procedure used is similar to that of Gilden and Hines for the Read avalanche diode.[6] This analysis relies on the fact that the total ac current density $\tilde{J}_T$, which is the sum of displacement-current density $\tilde{J}_d(x)$ and ac conduction-current density $\tilde{J}_c(x)$, is independent of position x. The injected ac current density can be expressed as a complex fraction of the total ac current density as follows

$$\tilde{J}_b = M\tilde{J}_T. \qquad [4]$$

Assuming the drift velocity v_d is saturated, the ac conduction current density at any position x in the drift zone is

$$J_c(x) = M\tilde{J}_T \exp\left\{-\frac{j\omega x}{v_d}\right\}, \qquad [5]$$

where ω is the angular frequency. The total ac current density is then

$$J_T = \tilde{J}_c(x) + j\omega\epsilon\tilde{\mathcal{E}}(x). \qquad [6]$$

Rearranging Eq. [6] yields an expression for the ac field $\tilde{\mathcal{E}}(x)$ at any point in the drift zone

$$\tilde{\mathcal{E}}(x) = \frac{\tilde{J}_T}{j\omega\epsilon}\left[1 - M \exp\left\{-\frac{j\omega X}{v_d}\right\}\right]. \qquad [7]$$

If the small-signal assumption is made that the ac field $\tilde{\mathcal{E}}_b$ is much small than the dc field $\tilde{\mathcal{E}}_{bo}$ at the forward-biased contact, Eq. [2] can be separated into ac and dc components. The result is

$$J_b = J_{bo} + \tilde{J}_b,$$

where

$$J_{bo} = A^{**}\, T^2 \exp\left\{-\frac{q}{kT}\left(\phi_{BO} - \sqrt{\frac{q\mathcal{E}_{bo}}{4\pi\epsilon}}\right)\right\}, \qquad [8]$$

and

$$\tilde{J}_b = \frac{qJ_{bo}}{2kT}\sqrt{\frac{q}{4\pi\epsilon\mathcal{E}_{bo}}}\,\tilde{\mathcal{E}}_b.$$

Combining the expression for $\tilde{J}_b$ with Eqs. [4] and [6] evaluated at $x = 0$ leads to the expression

$$M = \frac{1}{1 + j\dfrac{\omega}{\omega_b}}, \qquad [9]$$

where

$$\omega_b = \left(\frac{q}{2kT\epsilon} \sqrt{\frac{q}{4\pi\epsilon}} \right) \frac{J_{bo}}{\sqrt{\mathcal{E}_{bo}}}.$$

Substituting this equation into Eq. [7] and integrating over the length of the drift zone W gives

$$\tilde{V} = \frac{\tilde{J}_T W}{j\omega\epsilon} \left[1 - \frac{1}{1 + j\dfrac{\omega}{\omega_b}} \left(\frac{1 - e^{-j\theta}}{j\theta} \right) \right] \qquad [10]$$

for the ac voltage. Here we have defined the transit angle $\theta = \omega W / v_d$. Finally, the ac impedance $\tilde{Z}$, separated into real and imaginary parts, is

$$\tilde{Z} = \frac{1}{\omega C} \frac{1 - \cos\theta + \dfrac{\omega}{\omega_b} \sin\theta}{\theta \left[1 + \left(\dfrac{\omega}{\omega_b} \right)^2 \right]} + \frac{1}{j\omega C} \left[1 - \frac{\sin\theta - \dfrac{\omega}{\omega_b} (1 - \cos\theta)}{\theta \left[1 + \left(\dfrac{\omega}{\omega_b} \right)^2 \right]} \right], \qquad [11]$$

where $C = \epsilon A / W$ is the capacitance of a diode of area A in the absence conduction current. It is clear from examination of the real part of $\tilde{Z}$ that the requirement on transit angle for obtaining negative resistance is

$$2\pi (n + ½) < \theta < (n + 1)\, 2\pi,\ n = 0, 1, 2, \ldots \qquad [12]$$

For a given transit angle in this range, the resistance is negative only when the operating frequency exceeds some minimum value which is dependent on θ and ω_b.

Discussion

The real part of $\tilde{Z}$ can be made negative for any value of the ratio ω/ω_b greater than zero through the choice of an appropriate transit angle. However, the magnitude of the negative resistance becomes small for $\omega/\omega_b < 1$. This is illustrated in Fig. 2 where the real part of Z normalized to $1/\omega C$ is plotted as a function of θ for several values of ω/ω_b. As ω/ω_b decreases, the range of θ over which negative resistance occurs becomes smaller. Simultaneous optimization of the real part of Z with respect to ω/ω_b and θ results in an optimum transit angle of approximately 292°. The real and imaginary parts of $\tilde{Z}$ are plotted as a function of ω/ω_b for this value of θ in Fig. 3. The optimum negative real part is obtained for $\omega/\omega_b = 1.88$. For these conditions, the negative Q of the diode (defined as the angular frequency times the ratio of average stored energy to average energy generated per unit time) is approximately 22.5.

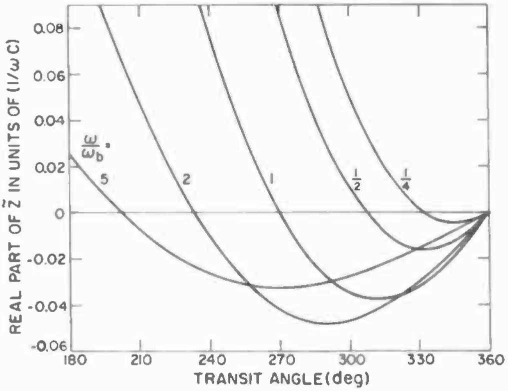

Fig. 2—Small-signal negative resistance as a function of transit angle.

The negative Q of this device is generally much larger in magnitude than can be obtained with avalanche diodes, and higher Q circuits are required to obtain a self-sustaining oscillation. The efficiency of the device as an oscillator or amplifier is expected to be lower than that of the avalanche diode. However, carrier injection is expected to be a much quieter process than avalanche generation. Therefore the device has potential as a low-noise low-power oscillator or amplifier.

As a practical example, the analysis is applied to the platinum-silicide on n-type silicon Schottky-barrier contact. The relevant para-

Table 1—Parameters of the PtSi-Si Schottky Barrier.[10]

Parameter	Value
A** for holes	32 A cm^{-2} $°K^{-2}$
$q\phi_{BO}$ for holes	0.25 eV
ϵ	12 ϵ_o

meters are listed in Table 1. The effect of the Schottky-barrier properties on the diode performance is contained in the "injection frequency" ω_b, which is proportional to $J_{bO}/\sqrt{\mathcal{E}_{bO}}$. In Fig. 4, J_{bO} is plotted as a function of $\sqrt{\mathcal{E}_{bO}}$ for several values of junction temperature T for the PtSi-Si barrier. At this point, only the solid curves are relevant. The value of field $\mathcal{E}_{bO}$ is limited to between 10^4 and 4×10^5 V/cm. The field must be greater than 10^4 V/cm to ensure that the injected holes travel at saturated velocity through the drift zone. If the hole velocity is not saturated, the ac field in the drift zone will modulate the carrier velocity, thereby affecting the phase relationship between the voltage and current. When the field exceeds a few times 10^5 V/cm, avalanche breakdown in the drift zone will occur.

In Fig. 5, the Schottky-barrier injection frequency $f_b = \omega_b/2\pi$ is plotted as a function of $\sqrt{\mathcal{E}_{bO}}$ for several values of T. As discussed previously, the device should operate with optimum performance at a

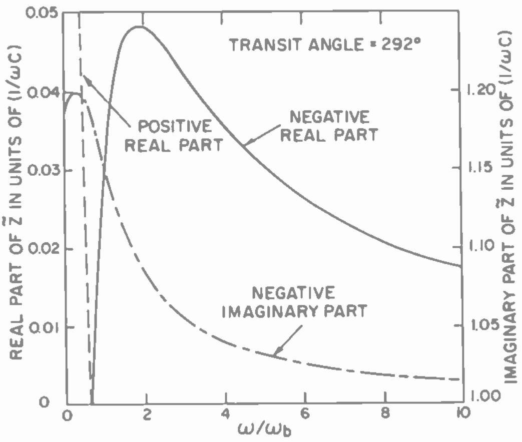

Fig. 3—Real and imaginary part of $\tilde{Z}$ as a function of ω/ω_b for a transit angle of 292°.

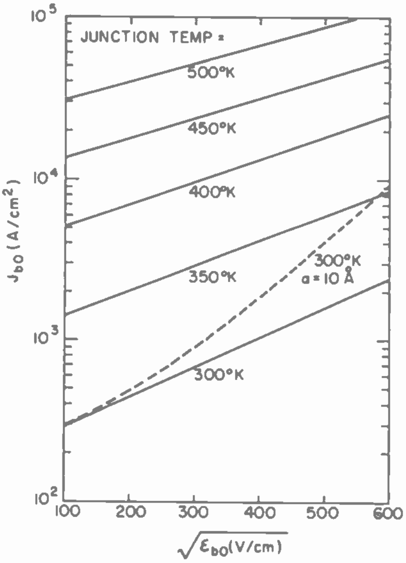

Fig. 4—DC injected current density as a function of the square root of the dc electric field at the interface for PtSi barrier.

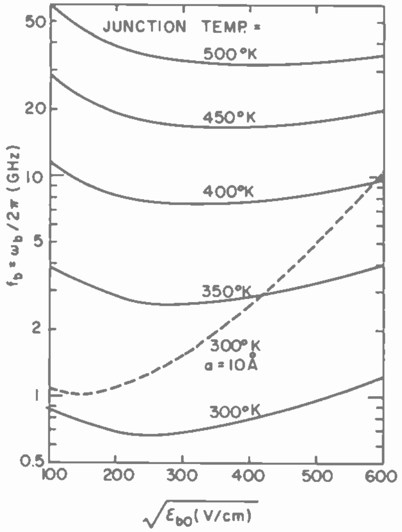

Fig. 5—PtSi Schottky-barrier injection frequency ($\omega_b/2\pi$) as a function of the square root of the dc electric field at the interface.

frequency of about two times f_b. The solid curves in Fig. 5 indicate that, for high-frequency operation, the diode may operate best at elevated temperature. The image-force barrier lowering is not great enough for the junction field to have a strong effect on f_b.

There is good experimental evidence that the actual barrier lowering is somewhat larger than predicted by the Schottky effect. Several mechanisms have been proposed, including electric field penetration into the barrier metal,[7] the dependence of the level of occupation of semiconductor surface states on $\mathcal{E}_b$,[8] penetration of surface-state charge into the semiconductor,[9] and a field dependence of barrier height predicted by an analysis of the equilibrium bound-charge distribution near the metal–semiconductor interface.[10] The relative importance of each mechanism is dependent on the surface condition of the semiconductor prior to formation of the Schottky barrier and the reaction that takes place between the metal and semiconductor. The density and distribution of surface states and the thickness of an insulating layer between the metal and semiconductor play a role in determining the field dependence of the barrier height. Regardless of the physical origin, the additional barrier lowering can be approximated as a linear function of $\mathcal{E}_b$, making the total barrier lowering

$$\Delta\phi = \sqrt{\frac{q\mathcal{E}_b}{4\pi\epsilon}} + \alpha\mathcal{E}_b, \qquad [13]$$

where α is a proportionality constant that must be experimentally determined. The small-signal theory parameters are then modified as follows:

$$\omega_b = \frac{q}{kT\epsilon}\left(\sqrt{\frac{q}{16\pi\epsilon\mathcal{E}_{bO}}} + \alpha\right) J_{bO} \qquad [14]$$

$$J_{bO} = A^*T^2 \exp\left\{-\frac{q}{kT}\left(\phi_{BO} - \sqrt{\frac{q\mathcal{E}_{bO}}{4\pi\epsilon}} - \alpha\mathcal{E}_{bO}\right)\right\} \qquad [15]$$

This modification can have a dramatic effect on the curves of Figs. 4 and 5. Values of α measured on silicon Schottky barriers range from 15 to 35 Å.[10] The value for α for PtSi on p-type silicon has not been measured, but, for the purpose of illustration, a value of 10 Å was assumed and the curves of J_{bO} and f_b at $T = 300$°K plotted. These curves (dashed lines in Figs. 4 and 5) indicate that the existence of even a small linear dependence of barrier height on electric field will make room-temperature operation at microwave frequencies possible. If the value of α is as great as 20 Å (the experimental value obtained for RhSi on p-type silicon[10]), operation through the millimeter wave range to 100 GHz is possible. Alternatively, use of a metal–semiconductor junction with a barrier potential that is slightly smaller than ϕ_{Bp} in the PtSi-Si system will make very high-frequency operation feasible.

Acknowledgments

The author is grateful to V. L. Dalal, B. B. Robinson, and C. P. Wen for discussions that clarified the physical model of the device under study. He also wishes to thank B. Hershenov for useful comments on the manuscript.

References:

[1] W. T. Read, Jr., "A Proposed High-Frequency, Negative-Resistance Diode," **Bell Sys. Tech. J.**, Vol. 37, p. 401, March 1958.

[2] R. E. Cardinal, RCA internal communication, June 1966; H. W. Ruegg, "A Proposed Punch-Through Microwave Negative Resistance Diode," **IEEE Trans. Electron Devices**, Vol. ED-15, p. 577, Aug. 1968.

[3] D. J. Coleman and S. M. Sze, "A Low Noise Metal-Semiconductor-Metal (MSM) Microwave Oscillator," **Bell Sys. Tech. J.**, p. 1695, May-June 1971.

[4] S. M. Sze, **Physics of Semiconductor Devices**, John Wiley and Sons, New York, 1969, pp. 378-381.

[5] **Ibid**, pp. 364-367.

[6] M. Gilden and M. E. Hines, "Electronic Tuning Effect in the Read Microwave Avalanche Diode," **IEEE Trans. Electron Devices**, Vol. ED-13, p. 169, Jan. 1966.

[7] C. A. Mead, E. H. Snow, and B. E. Deal, "Barrier Lowering and Field Penetration at Metal-Dielectric Interfaces," **Appl. Phys. Letters**, Vol. 9, p. 53, 1 July 1966.

[8] C. R. Crowell, H. B. Shore, and E. E. LeBate, "Surface-State and Interface Effects in Schottky Barriers at N-Type Silicon Surfaces," **J. Appl. Phys.**, Vol. 36, p. 3843, Dec. 1965.

[9] G. H. Parker, T. C. McGill, and C. A. Mead, "Electric Field Dependence of GaAs Schottky Barriers," **Solid-St. Electron.**, Vol. 11, p. 201, Feb. 1966.

[10] J. M. Andrews, and M. D. Lepselter, "Reverse Current-Voltage Characteristics of Metal-Silicide Schottky Diodes," **Solid-St. Electron.**, Vol. 13, p. 1011, July 1970.

GaN Electroluminescent Diodes

J. I. Pankove, E. A. Miller, and J. E. Berkeyheiser
RCA Laboratories, Princeton, N. J.

Abstract—GaN diodes of the i-n (insulating-to-n-type) variety have been made by Zn doping. These exhibit green dc electroluminescence at room temperature. The radiated output is proportional to the input power; the external power efficiency is 10^{-4}; an external quantum efficiency of 10^{-2} has been obtained. The response time of several microseconds is limited mostly by the RC time constant of the structure. Photovoltaic measurements indicate a barrier height of about 1.6 eV at the i-n transition.

Introduction

Insulating GaN can be obtained by growing the material by the vapor-phase technique[1] in the presence of Zn vapor. We have recently reported electroluminescence in insulating GaN to which connections were made by point-contact electrodes.[2] The emission had a relatively low efficiency and occurred at many microscopic spots correlated with grain boundaries.

The present paper deals with the observation of more efficient electroluminescence over an extended area. The luminescence was obtained at the i-n transition between a 20-μm n-type layer and a 2.4-μm insulating layer, both grown by vapor transport. Hall measurements indicate an electron concentration of 1×10^{18} cm^{-3} and a mobility of 240 cm^2/Vsec in the n-type layer. Properties of i-n transitions in GaN, other than electroluminescence will also be described.

Electrical Characteristics

The presence of the insulating layer was detected by probing the surface with a point contact. When the cleaved side of the crystal was probed, the highly conducting region was found. The wafer was cut ultrasonically into about 1-mm-diameter disks. Indium contacts were made to the exposed edge of the n-type GaN with a peripheral ring electrode and also to the center of the insulating layer. Rectification characteristics could be obtained. Although these varied from sample to sample, Fig. 1 shows a typical $I(V)$ dependence. The $I(V)$ characteristic, with the insulating layer positive with respect to the n-type layer, usually exhibits a quadratic dependence $I \propto V^2$.

The capacitance of a 10^{-3} cm^2 indium dot is 3×10^{-12} F. From these values, one deduces that the thickness of the insulating layer is 2.4 μm.

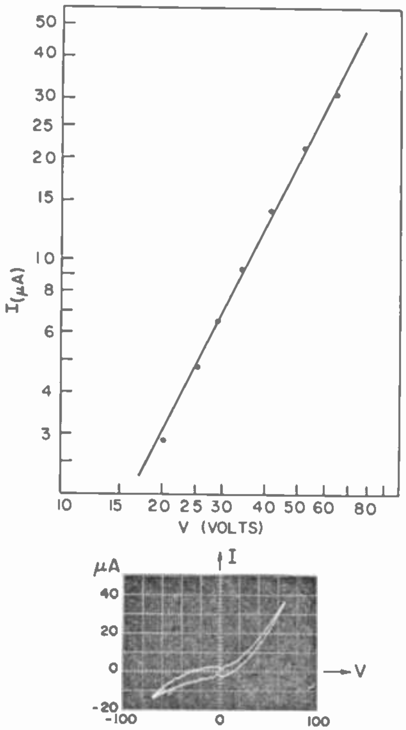

Fig. 1—*IV* characteristics of i-n diodes.

Emission Spectra

The photoluminescence spectra of the Zn-doped GaN peaked at about 2.8 eV at 78°K (the usual transition to Zn centers) with a weak near-gap contribution at 3.45 eV (Fig. 2). As the specimen was warmed up to 242°K, a new peak appeared at 2.5 eV; at room temperature, this peak is dominant and positioned at about 2.47 eV. The

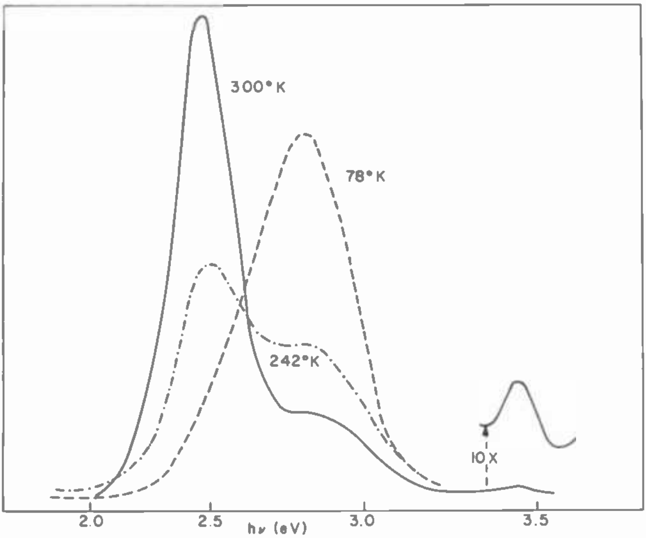

Fig. 2—Photoluminescence spectra at various temperatures for region of main interest. The low energy edge cutoff below 2.3 eV due to the photomultiplier response.

material is very nonuniform, however, and other spectra could be found at various locations on this wafer (see, for example, Fig. 3). Similar observations of nonuniformity were later found by electroluminescence.

Electroluminescence was obtained under the contact to the insulating layer. In some units, blue-violet light was emitted, and in others, green light. Broad peaks at 2.8, 2.4, 2.1, 1.8 and 1.5 eV could be found with "forward" bias (positive on the indium dot). With "reverse" bias (negative at indium dot), only small bluish microplasmas could be seen —and sometimes incandescence. The brightest and most uniform emission was the green emission (see Fig. 4). The green light appeared uniformly under the indium dot of two diodes and under part of the dot of several other diodes.

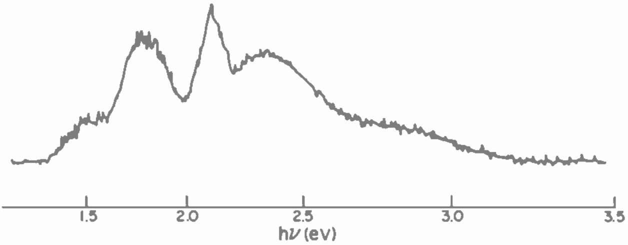

Fig. 3—Photoluminescence spectra at 300°K of another region of same crystal as used in Fig. 1.

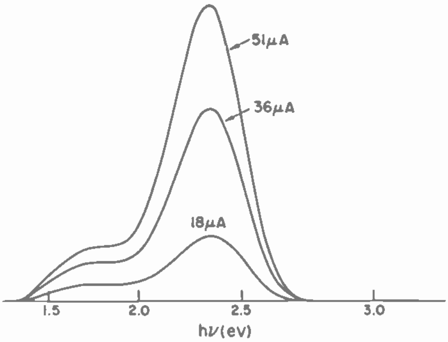

Fig. 4—Electroluminescent spectra at room temperature for three different currents through the i-n transition.

Conversion Efficiency

The emission intensity increased approximately as the 3/2 power of the current and linearly with the power input, up to burn-out at 270 mW (Fig. 5). Note that the proportionality of light output to 3/2 power of current is consistent with the quadratic $I(V)$ characteristic and the linear dependence of light on input power ($P_i = I \times V = I \times I^{1/2}$). The maximum input power density (> 100 W/cm^2 pulsed) could not be determined because the current distribution is believed to be non-

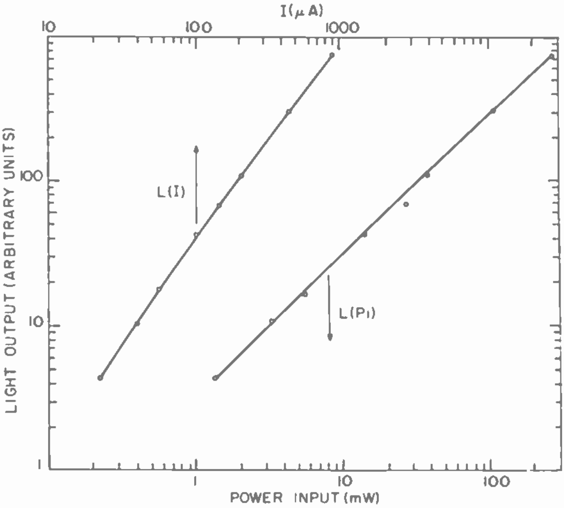

Fig. 5—Dependence of light intensity on current and on input power.

uniform. The cw luminescence efficiency was determined from a measurement of the emitted power using a calibrated selenium detector that collected almost all the light emitted from one side of the diode. It was assumed that only one half of the radiation was collected by the detector. The power efficiency was then about 10^{-4}, and the quantum efficiency was about 3.5×10^{-3} at 35 μA and over 10^{-2} at 1 mA.

Temperature Dependence

One diode was immersed in parafin oil, which is transparent between 3500 Å and 1.2 μm. The emission of the diode was measured with a 45-volt forward bias at various temperatures up to 150°C. The emission of the green peak shifted to lower energies by about 40 meV (less than the ~70 meV expected from the temperature dependence of the energy gap[3]). Since the current increased with temperature while the emission output remained nearly constant, it can be concluded that the emission efficiency decreased with increasing temperature.

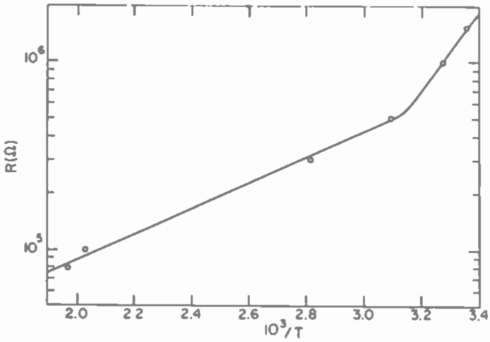

Fig. 6—Temperature dependence of diode internal resistance.

During the above experiment, it was convenient to measure the $I(V)$ characteristic of the diode and to determine its approximate internal resistance from the slope of the $I(V)$ curve at the highest current. This data plotted against $1/T$ (Fig. 6) indicates a thermal activation energy of 0.13 eV for transport in the insulating layer above 315°K.

Photovoltaic Properties

Since basically the diode consists of two differently doped regions, it was interesting to explore the photovoltaic properties of the i-n transi-

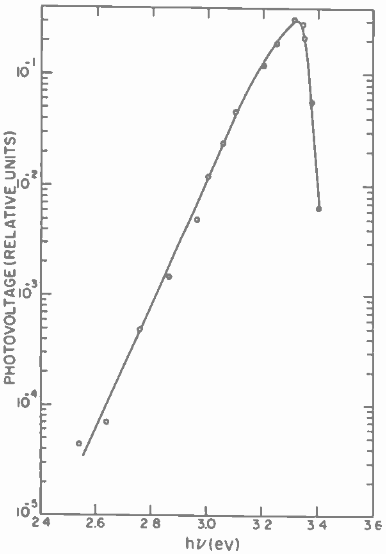

Fig. 7—Photovoltaic spectrum of i-n transition illuminated through n-region.

tion. The photovoltaic spectrum peaks at 3.30 eV (Fig. 7). The abrupt cutoff at the higher energy edge of the photovoltaic spectrum is determined by absorption in the n-type layer—this indicates that the hole diffusion length is much shorter than 2×10^{-3} cm. The low-energy edge tails down exponentially as exp ($h\nu/0.076$ eV). The diode was then illuminated with an Xe lamp filtered to transmit only UV radiation (no

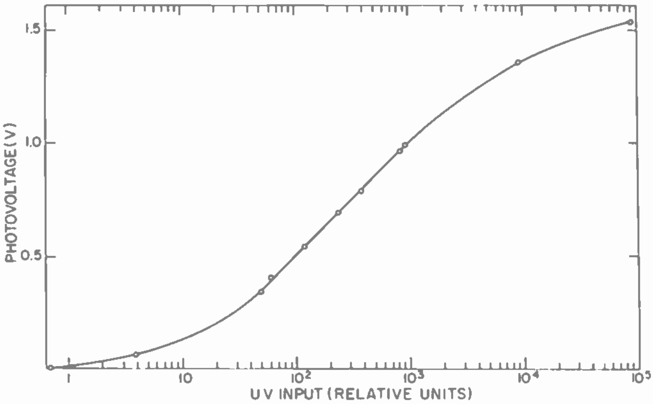

Fig. 8—Dependence of photovoltage on light intensity.

photovoltage is obtained below 2.6 eV). The intensity of illumination was varied by changing the lamp-to-diode distance, by inserting neutral-density filters, or by focusing the radiation. The intensity of the incident radiation was checked with a selenium detector. The corresponding response is shown in Fig. 8, which indicates that the photovoltage tends to saturate beyond about 1.6 eV.

The saturation of the open-circuit photovoltage is a measure of the barrier height, Φ_B, at the i-n transition (Fig. 9) : the maximum photovoltage is obtained when the bands have been flattened. The polarity of the photovoltage is positive at the indium dot, in accord with the present model. The i-n transition was scanned with a light spot from a Zr arc lamp focused to a diameter of less than 20 μm. There was no substantial change in the photovoltage over the entire area of the i-n transition even outside the In dot. This result confirms that we are dealing with a thin insulating layer extending over the whole surface of the crystal rather than with a barrier under the indium dot, such as a Schottky barrier.

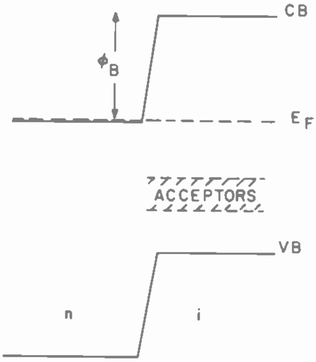

Fig. 9—Band structure at i-n transition.

Trapping Effects

When a positive ("forward") bias is applied to the i-region of Fig. 9, the barrier to electrons at the i-n transition is retained, as shown in Fig. 10; now, however, there appears also a trap for holes. When holes are trapped at this narrow interfacial layer, their space charge lowers the barrier and allows more electrons to flow from the n-layer to the indium dot contact (much as at the floating base of an n-p-n transistor). With a negative ("reverse") bias across the i-n transition, only the saturation current can flow. Illuminating the diode with 3.3 eV light generates electron–hole pairs at the i-n transition. With a reverse bias of 60 V, the saturation current is increased by a photocurrent of 1.6 μA; but with a 60-V forward bias, the optically excited holes that are trapped at the interface amplify the photocurrent to 2.8 μA. The spectral dependence of the photocurrent had the same shape for both polarities of bias (identical threshold), indicating that the mechanism of optical generation of carriers with an optical bias is due to the photoconductivity in the high-field region of the insulating layer, rather than to injection at the In contact.

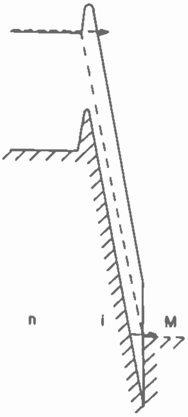

Fig. 10—Band structure of i-n transition with positive bias on i-region.

The presence of traps is often manifested by slow rise and decay times for pulsed luminescence. In the present case, the insulating layer has an inherent RC time constant that is independent of trapping effects and that may dominate the measured response. It is evident from the model of Fig. 10, however, that trapping will occur only during forward bias, whereas a reverse bias will empty the traps. (Note that a sufficiently large reverse bias will cause breakdown luminescence.) A close examination of Fig. 11 reveals that forward-bias electroluminescence has slower rise and decay times than the RC-controlled reverse-bias luminescence. The decay of forward-bias luminescence was followed by expanding the scale of the displayed light intensity. The resulting data, plotted in Fig. 12, shows that after an initial decay with

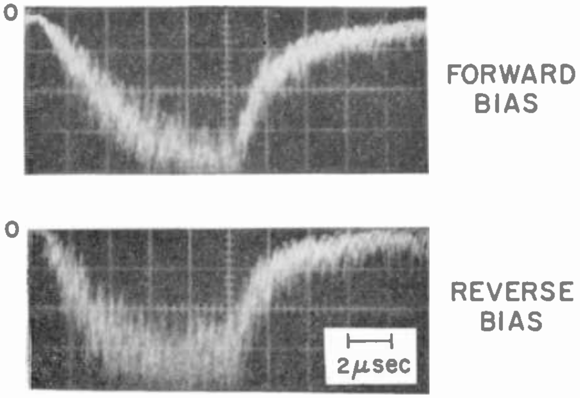

Fig. 11—Time dependence of pulsed luminescence with forward and reverse bias applied across the i-n transition.

a 2.4-μsec time constant, the luminescence continues to decay with a 14-μsec time constant. The shorter time constant compares with the *RC* value of 4.5-μsec obtained from the above measurements of resistance and capacitance.

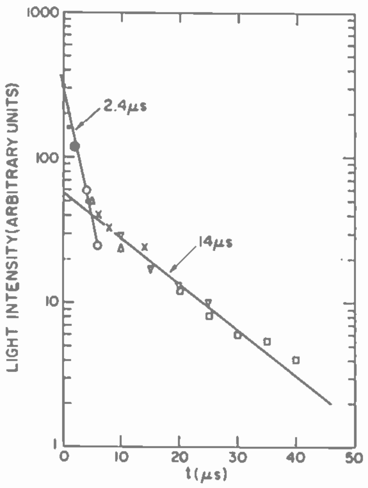

Fig. 12—Time dependence of luminescence decay after "forward" polarization.

Tentative Model

From the data obtained thus far, it is possible to construct a tentative model for the distribution of states in the i-n diode as shown in Fig. 9. The energy gap of GaN is 3.5 eV. In the n-type region, the Fermi level is slightly above the conduction band edge (we have observed no carrier freeze-out at low temperature in n-type GaN). The major emission band at 2.37 eV would be due to transitions terminating at Zn acceptor levels (or other centers associated with zinc impurities) about 1.1 eV above the valence-band edge. However, the low-temperature emission spectra peaking at 2.85 eV suggest that the Zn acceptors (and associated centers) extend from about 0.7 eV above the valence band, thus forming an acceptor band at least 0.4 eV wide. The response time of electroluminescence seems limited mostly by the *RC* time constant of the device.

Conclusion

GaN shows promise as a suitable material for a blue or green electroluminescent lamp. It is relatively easy to fabricate; the electrodes can be shaped into useful configurations, such as for alphanumeric displays. If ever p-type conducting GaN is obtained, it should be possible to make GaN injection lasers, since lasing in the n-type material has already been obtained by optical pumping.[4]

Acknowledgments

The authors are grateful to Mrs. M. Harvey for processing the diodes and to H. Kressel, M. Lampert, D. Richman and R. Williams for useful discussions.

References:

[1] H. P. Maruska and J. J. Tietjen, "The Preparation and Properties of Vapor-Deposited Single-Crystalline GaN," **Appl. Phys. Letters**, Vol. 15, p. 327, 1969.

[2] J. I. Pankove, E. A. Miller, D. Richman, and J. E. Berkeyheiser, **J. Luminescence** (to be published).

[3] J. I. Pankove, unpublished data: $dE_g/dT = -4.8 \times 10^{-4}$ eV/degree above 150° K.

[4] R. Dingle, R. F. Leheny, K. L. Shaklee, and R. B. Zetterstrom, "Stimulated Emission and Laser Action in GaN," **Bull. Amer. Phys. Soc.**, Ser. II, Vol. 16, p. 408, 1971.

Mode Guiding In Symmetrical (AlGa)As-GaAs Heterojunction Lasers With Very Narrow Active Regions

H. Kressel, J. K. Butler,[*] F. Z. Hawrylo, H. F. Lockwood, and M. Ettenberg

RCA Laboratories, Princeton, N. J.

Abstract—A theoretical and experimental study is presented of double heterojunction laser diodes in which the recombination region is so narrow that only the center of the wave is confined to the region of inverted population. Good agreement is demonstrated between theory and experiment based on a three-region-waveguide model. By use of a highly doped and closely compensated active region and small bandgap discontinuities at the heterojunctions, laser diodes have been made with very low room-temperature threshold and normal beam divergence.

Introduction

The refractive index discontinuities at (AlGa) As-GaAs heterojunctions improve mode guiding in the p-n junction region of laser diodes, which contributes to their greatly increased room temperature efficiency.[1-3] Previous papers have dealt with the near- and far-field emission patterns of diodes incorporating either one[3] or two heterojunctions[4,5] confining the radiation to an active region with a thickness of about 1 μm or more. The present paper extends the previous work to diodes where the active "waveguide" region is a small fraction of a micrometer thick. Here only the center of the wavefront is within the narrow recombination region, and a significant fraction of the electric field intensity propagates in the lower-refractive-index passive material adjoining the active region. Good agreement is demonstrated between simple waveguide theory and experiment. Of technological interest is

---

[*] Presently at Electronic Sciences Center, Southern Methodist University, Dallas, Texas 75222

the fact that the lasers described here combine the features of very low threshold, high efficiency, and relatively narrow beam. The present work was suggested by the theoretical modeling of the laser cavity as a three-slab structure of sufficient simplicity[1-4] to permit detailed calculation of the performance but enough complexity to describe subtle variations in the processing. This paper describes a study of the effect of the material parameters and the optimization of the device for good threshold and normal beam width.

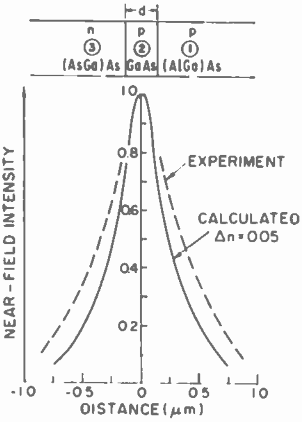

Fig. 1—Schematic of the basic heterojunction configuration showing the theoretically calculated and experimentally observed near-field intensity distribution. The experimental intensity distribution was determined from a densitometer trace. The calculated intensity distribution is based on a refractive index discontinuity $\Delta n = 0.05$ at the (AlGa)As-GaAs heterojunction interfaces.

Device Description

The diodes were fabricated by liquid-phase epitaxial growth in a multi-bin apparatus, originally described by Nelson,[6] in which a GaAs wafer is pushed sequentially into adjacent bins containing appropriate melts, while the furnace is slowly cooled from ~880°C.

A schematic of the diode structure studied here is shown in Fig. 1 (top). The thin GaAs recombination (active) region 2 ($d = 0.25$ μm in the case shown) is closely compensated with Si and Zn to a *total* concentration of $\sim 10^{19}$ cm^{-3} and a *hole* concentration of $2\text{-}5 \times 10^{17}$ cm^{-3} as determined from capacitance–voltage measurements. The difference in the bandgap energy between region 2 and the adjoining regions 1 and 3 is 0.1-0.15 eV as estimated from photoluminescence measurements. The free-carrier concentration in both regions 1 and 3 is approximately 2×10^{18} cm^{-3} (doped with Zn and Te, respectively).

Results and Analysis

1. Near- and Far-Field Patterns

The electric field intensity in the *near field* was determined from densitometer traces. As shown in Fig. 1, the electric field intensity extends significantly beyond the borders of the very narrow recombination region 2 in which the p+-p potential barrier helps to confine the carriers.[1,7] Above threshold the field intensity is symmetrically distributed about region 2 (Fig. 1), but below threshold the pattern is broader and less symmetrical, with a "tail" extending into the n side of the junctions. Owing to some uncertainty in focusing of the near-field image, the densitometer trace is probably broader than the true electric field distribution.

The near-field intensity distribution shown in Fig. 1 is theoretically consistent with a symmetrical three-region-waveguide model in which the recombination region, of width d, is too narrow to fully confine the TE wave. It is known that guided wave propagation is theoretically impossible below a critical d value in an *asymmetrical* waveguide, but that this restriction is not present in a symmetrical dielectric structure.[8-10]

Based on a bandgap energy discontinuity $\Delta E_g \cong 0.1$-0.15 eV, a refractive index discontinuity $\Delta n \cong 0.05$ is a reasonable estimate.[2] Fig. 1 shows a calculated plot of the electric field intensity in the junction vicinity with $\Delta n = 0.05$ and $d = 0.25$ μm and assuming an abrupt interface. The extent of the calculated field distribution is somewhat smaller than the experimental densitometer trace, which may be due to the focusing uncertainty mentioned earlier.

A more reliable comparison of waveguide theory and experiment is obtained by comparing the far-field emission pattern where the experimental measurements are more precise. The *far-field* emission pattern of the same laser is shown in Fig. 2. The electric field is strongly polarized parallel to the junction (TE wave). A single peak is seen in the direction perpendicular to the plane of the junction with a half-intensity width $\theta_p = 21°$. This value is similar to that seen in typical single heterojunction "close-confined" (SH-CC) lasers operating in the fundamental transverse cavity mode.[3] However, the 300°K threshold current density of the present lasers is much lower than that of state-of-the-art SH-CC lasers (8000-10,000 A/cm^2).[7,11] Fig. 2 shows the satisfactory agreement of the calculated with the observed far-field

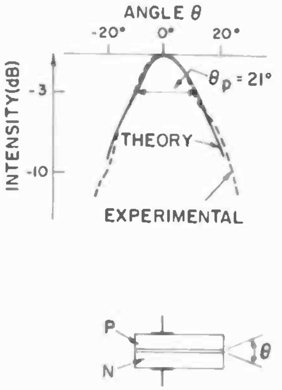

Fig. 2—Experimental and theoretical far-field intensity distribution in the direction perpendicular to the junction plane. The theoretical curve is based on $\Delta n = 0.05$ and $d = 0.25$ μm.

emission pattern using $\Delta n = 0.05$ and $d = 0.25$ μm. Thus, we conclude that mode guiding in narrow-active-region lasers can be satisfactorily explained on the basis of a simple three-region-waveguide model.

The far-field beamwidth θ_p decreases with decreasing cavity thickness d for a given refractive index difference Δn as shown in the theoretical curve of Fig. 3. For example, with $\Delta n = 0.05$, the calculated

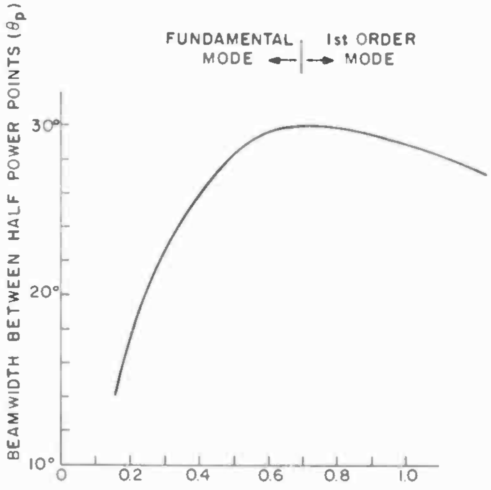

Fig. 3—Theoretical beamwidth θ_p between the half-power points in the direction perpendicular to the junction plane as a function of the active region thickness d with $\Delta n = 0.05$.

beamwidth $\theta_p = 30°$ for $d = 0.7$ μm. For this d value, the fundamental transverse order mode is still favored; for larger d, the calculated previously.[16] The gain coefficient in the lasers described here is linearly dependent upon the current density, so that

2. Threshold and Efficiency

Threshold current densities as low as 1400 A/cm^2 and differential quantum efficiencies of 30-50% were obtained at 300°K with lasers having $\theta_p \approx 20°$. This threshold is comparable to those previously reported for double heterojunction lasers with larger bandgap discontinuities (i.e., stronger radiation confinement)[12-15] and, consequently, larger beam divergence (>40°).[4]

Fig. 4(a) shows the threshold current density J_{th} as a function of the facet reflectivities R_1 and R_2, which were varied with SiO films of appropriate thickness. The reflectivities were calculated as described

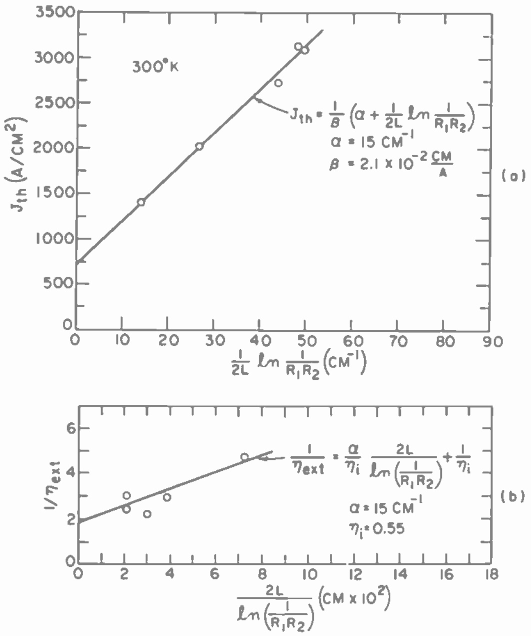

Fig. 4(a) Threshold current density at 300°K as a function of the Fabry–Perot cavity end loss, $(1/L)$ ln $(1/R_1R_2)$, of a single diode. The facet reflectivity was varied with SiO coatings of various thickness. (b) Differential quantum efficiency as a function of the reciprocal cavity end loss of the same diode described in (a).

previously.[16] The gain coefficient in the lasers described here is linearly dependent upon the current density, so that

$$J_{\text{th}} = \frac{1}{\beta}\left(\bar{\alpha} + \frac{1}{2L}\ln\frac{1}{R_1R_2}\right) \qquad [1]$$

or

$$J_{\text{th}} = J_{\infty}\left(1 + \frac{1}{2L\bar{\alpha}}\ln\frac{1}{R_1R_2}\right).$$

where L is the Fabry-Perot cavity length, $\bar{\alpha} = 15$ cm^{-1}, $\beta = 2.1 \times 10^{-2}$ cm/A, and J_{∞} (i.e., the extrapolated value for no end losses) is 750 A/cm^2. It was not possible to fit the data by assuming that $J_{\text{th}} \propto g_{\text{th}}^{1/b}$ with $b > 1$, where g_{th} is the gain coefficient at threshold.

As shown in Fig. 3b, the same $\bar{\alpha}$ of 15 cm^{-1} provides a reasonable fit to the variation of the differential quantum efficiency η_{ext} of the same laser as a function of reflectivity using the equation

$$\eta_{\text{ext}} = \eta_i \frac{\ln\dfrac{1}{R_1R_2}}{\bar{\alpha}L + \ln\dfrac{1}{R_1R_2}}, \qquad [2]$$

with an assumed internal quantum efficiency $\eta_i = 0.55$.

Because the lasing energy is less than the bandgap energy in the (AlGa)As regions adjoining the cavity, the radiation is only weakly absorbed there (mainly by free carriers).

We now consider the dependence of the threshold current density on the cavity width d. Increasing d increases the fraction of the wave inside the recombination region, thus increasing the gain at a fixed density of injected carriers; however, maintaining the density in the wider recombination region requires a higher current density. Consequently, for a given value of Δn there is a width d that minimizes J_{th}.

The gain coefficient at threshold, g_{th}, is plotted in Fig. 5 as a function of d. The curve was calculated for an absorption coefficient of 15 cm^{-1} in the (AlGa)As p-region and 7.5 cm^{-1} in the (AlGa)As n-region. Also shown in Fig. 4 is the propagation constant of the fundamental mode normalized to the free-space wave number $k_o = 2\pi/\lambda_o$ (λ_o is the free-space wavelength). Note that as d decreases, the propagation constant decreases and approaches the index of refraction of the outer p- and n-regions. This is because the wave is extending more into the outer regions. Since these regions are lossy, the gain at threshold has to be increased as d is narrowed. In the limiting case, we find that as $d \to 0$,

$$g_{\text{th}} \to \alpha_{fc} + \frac{\alpha_p + \alpha_n}{8n\Delta n k_o^2 d^2}, \qquad [3]$$

where α_p and α_n are the free-carrier absorption coefficients in the p- and n- (AlGa)As regions, respectively; $n = 3.6$ and α_{fc} is the free-carrier absorption coefficient of the active region.

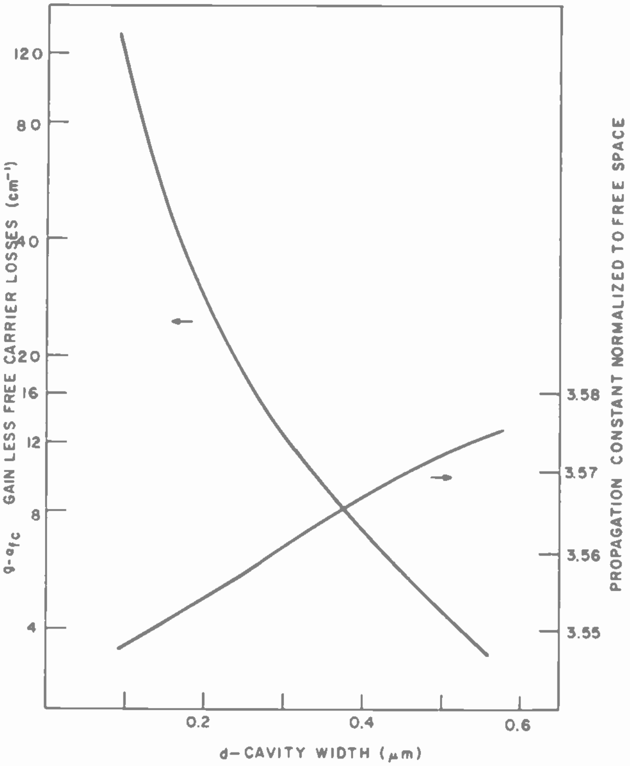

Fig. 5—The threshold gain coefficient, g_{th}, for an infinite-length cavity and normalized propagation constant plotted as a function of a cavity width. The index discontinuity was held constant ($\Delta n = 0.055$) for all calculations. The absorption coefficient values in the p- and n-(AlGa)As regions adjoining the active region were 15 cm^{-1} and 7.5 cm^{-1}, respectively.

As d approaches zero, g_{th} tends to infinity as d^{-2}. If we assume that $J_{\text{th}} \propto dg_{\text{th}}$, then $J_{\text{th}} \rightarrow d^{-1}$ in the limit of d small. On the other hand, for d large, $g_{\text{th}} \rightarrow \alpha_{fc}$; and hence, $J_{\text{th}} \propto d\alpha_{fc}$. Fig. 6 shows the normalized threshold current density plotted as a function of d. We have assumed that the active region is fully inverted and that only the fundamental mode is propagating. A value of $d = 0.2$-0.3 μm leads to the minimum in J_{th} with $\Delta n = 0.05$. A smaller d decreases θ_p (Fig. 3), but at the expense of increased J_{th}.

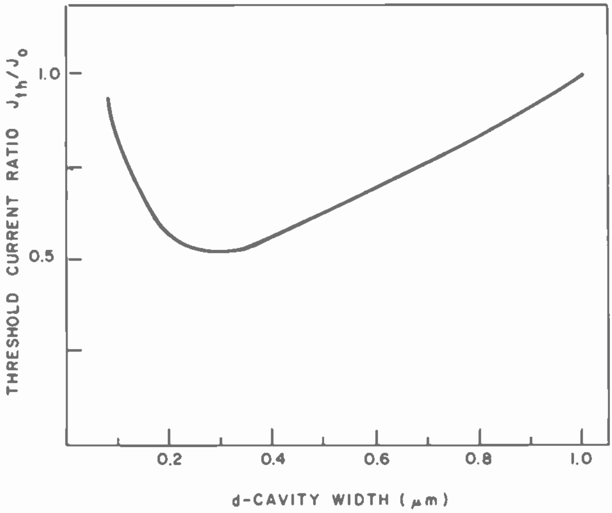

Fig. 6—The threshold current density J_{th} plotted as a function of the active region width d where we have normalized J_{th} to the threshold current density J_o for $d = 1$ μm with all other internal parameters held constant. The form of the current density is given as $J_{\text{th}} = J_o d(\alpha_{fc} + g_{\text{th}})/(\alpha_{fc} + g_{\text{tho}})$ where g_{tho} is the threshold gain for $d = 1$ μm. The quantity g_{th} is plotted in Fig. 5.

Conclusions

The near- and far-field emission patterns of (AlGa)As-GaAs heterojunction laser diodes with guiding regions so narrow that only the center of the wave is confined to the inverted region are consistent with the predictions of three-region-waveguide model. It is shown that with an appropriate combination of doping, of discontinuity in refractive index, and of thickness of the active layer, heterojunction lasers can be made that combine low threshold current densities (1400-2500 A/cm^2 at room temperature), high differential quantum efficiencies

(30-50%), and reasonable beam-width perpendicular to the junction (~20°). This angular divergence is half that of previous double heterojunction lasers with similar threshold current densities. Devices of this design are of potential interest in applications requiring low power output at very high duty cycles. Similar lasers with the junction very close to a copper heat sink (within ~5 μm) have operated continuously at room temperature with a power output of 120 mW and a power efficiency of ~7%. With improved metallic contacts and heat sink, higher values are possible.

Acknowledgments

We are grateful to H. S. Sommers, Jr. for some of the measurements and discussions, J. I. Pankove for comments on the manuscript, and to N. DiGiuseppe, D. B. Gilbert, M. Falk, and J. Alexander for technical assistance.

References:

[1] H. Kressel and H. Nelson, "Close-Confinement GaAs p-n Junction Lasers with Reduced Optical Loss at Room Temperature," **RCA Review**, Vol. 30, p .106 (1969).

[2] H. Kressel, H. Nelson and F. Z. Hawrylo, "Control of Optical Losses in p-n Junction Lasers by Use of a Heterojunction: Theory and Experiment," **J. Appl. Phys.**, Vol. 41, p. 2019 (1970).

[3] N. E. Byer and J. K. Butler, "Optical Field Distribution in Close-Confined GaAs Laser Structures," **IEEE J. Quantum Electron.**, Vol. QE-6, p. 291 (1970).

[4] J. K. Butler, H. S. Sommers, Jr., and H. Kressel, "High-Order Transverse Cavity Modes in Heterojunction Diode Lasers," **Appl. Phys. Letters**, Vol. 17, p. 403 (1970).

[5] J. E. Ripper, J. C. Dyment, L. A. D'Asaro, and T. L. Paoli, "Stripe-Geometry Double Heterostructure Junction Lasers. Mode Structure and CW Operation above Room Temperature," **Appl. Phys. Letters**, Vol. 18, p. 155 (1971).

[6] H. Nelson, **Depositing Successive Semiconductor Layers from the Liquid Phase**, U.S. Patent 3,565,702 (1971).

[7] I. Hayashi, M. B. Panish, and P. W. Foy, "A Low-Threshold Room-Temperature Injection Laser." **IEEE J. Quantum Electron.**, Vol. QE-5, p. 211 (1969).

[8] W. W. Anderson, "Mode Confinement and Gain in Junction Lasers," **IEEE J. Quantum Electron.**, Vol. QE-1, p. 228 (1965).

[9] M. J. Adams and M. Cross, "Wave-Guiding Properties of GaAs-$A1_xGa_{1-x}As$ Heterostructure Lasers," **Phys. Letters**, Vol. 32A, p. 207 (1970).

[10] J. K. Butler, "Theory of Transverse Cavity Mode Selection in Homojunction and Heterojunction Semiconductor Diode Lasers," **J. Appl. Phys.**, Sept. (1971).

[11] R. Gill, "Room Temperature Close-Confined GaAs Laser with Overall External Quantum Efficiency of 40%," **Proc. IEEE**, Vol. 58, p. 949 (1970).

[12] Zh. I. Alferov, V. M. Andreev, E. L. Portnoi, and M. K. Trukan, "AlGaAs-GaAs Heterojunction Injection Lasers with a Low Room-Temperature Threshold," **Sov. Phys.-Semicon.**, Vol. 3, p. 1107 (1970).

[13] I. Hayashi, M. B. Panish, P. W. Foy, and S. Sumski, "Junction Lasers Which Operate Continuously at Room Temperature," **Appl. Phys. Letters**, Vol. 17, p. 109 1970).

[14] H. Kressel and F. Z. Hawrylo, "Fabry-Perot Structure $Al_xGa_{1-x}As$ Injection Lasers with Room-Temperature Threshold Current Densities of 2530 A/cm^2," **Appl. Phys. Letters**, Vol. 17, p. 169 (1970).

[15] I. Sakuma, H. Yonezu, N. Nishida, K. Kobayashi, F. Saito, and Y. Nannichi, "Continuous Operation of Junction Lasers at Room Temperature," **Jap. J. Appl. Phys.**, Vol. 10, p. 282 (1971).

[16] M. Ettenberg, H. S. Sommers, Jr., H. Kressel, and H. F. Lockwood, "Control of Facet Damage in GaAs Laser Diodes," **Appl. Phys. Letters**, Vol. 18, p. 571 (1971).

Clutter Suppression by Use of Weighted Pulse Trains

T. Murakami and R. S. Johnson
RCA Missile and Surface Radar Division, Moorestown, N.J.

Summary—Use of amplitude weighting of unequally spaced pulses is studied to determine the improvement in clutter performance that can be obtained in a coherent radar. A computer program that gives the optimum weights and the signal-to-clutter gain as a function of Doppler frequency has been developed. The effect of thermal noise and limiting have also been included in the program, which has a capacity of weighting up to 20 pulses. This study has shown the following: (1) With optimally weighted nonperiodic pulse trains, high clutter attenuation can be obtained over a large Doppler interval. (2) Signal-to-clutter gain obtained with optimum weighting is substantially greater than that obtained with binomial weights. (3) Conditions of low signal-to-noise ratio or i-f limiting restrict the benefits of optimized pulse weighting.

Introduction

Certain aspects of the performance characteristics of MTI (Moving Target Indication) radar using delay-line cancellers[1-3] to reject the clutter echoes and pass Doppler-shifted signals from moving targets are considered here. One advantage of the delay-line canceller type of clutter-rejection system is that range information is preserved without the use of range gates, thus making the radar much simpler for some applications than a range-gate Doppler-filtered system. The chief limitation of the canceller type of MTI radar in the past has been the complexity required to achieve the special transfer characteristics required and the need for nearly perfect adjustment in the delay lines to obtain near theoretical performance. With the advent of microelectronics and digital techniques, these difficulties have been

---

[†] This paper is extracted from T. Murakami's Doctoral Thesis for the University of Pennsylvania (see Ref. [14]).

alleviated to a large extent, so that the performance of the canceller type of system can be greatly improved.

The intent of this study is to determine the theoretical clutter performance of a coherent radar using a particular type of delay-line cancelling system. In the system considered, the pulses are staggered in repetition period to avoid target blind speeds and the pulses are amplitude weighted in an optimum way to achieve high clutter cancellation over the Doppler region of interest. The use of optimally weighted pulse trains for clutter suppression in the past has been mostly confined to finite pulse trains with uniform periods.[3-7] Brennan and Reed[8] analyzed optimum processing of unequally spaced radar pulse trains for clutter rejection but only indicated how one might proceed to solve the problem.

A portion of the analysis given here is not original and can be found in the references cited. It is given for completeness and to aid in the understanding of the extensions made in the study. The main contribution of this study is a means to determine an optimum pulse spacing combined with a method of determining the optimum pulse weights for the specified train of pulses that results in good clutter-rejection performance. The signal-to-clutter gain performance is also provided as part of the output of the computer program that was developed. Effects of thermal-type noise and limiting on the performance can also be found through the use of this computer program.*

The main items in this paper in the order of study are:

[1] System response of a delay-line canceller is determined.

[2] Signal-to-clutter gain is defined and then found for the delay-line canceller.

[3] The method for determining the optimum pulse weights based on Gaussian-type clutter is explained.

[4] A method for choosing the interpulse spacings is developed.

[5] The calculated results are explained.

In the analysis, the pulse spacing to achieve acceptable Doppler response is determined by a graphical method, and the corresponding pulse-amplitude weights are found by maximizing the function representing the average signal-to-clutter gain produced in the processor. Pulse-amplitude weighting procedures applied to equally spaced pulses show that optimum weighting results in about a 3-dB advantage over the binomial weighting normally associated with cascaded single-delay-

---

* A copy of the computer programs is available from the authors on request.

line cancellers.[5] This study shows that the gain difference between optimum and binomial weighting of staggered pulse trains can be considerably greater than 3-dB. The improvement obtained is shown to be a function of the spectral spread of clutter and the number of pulses used.

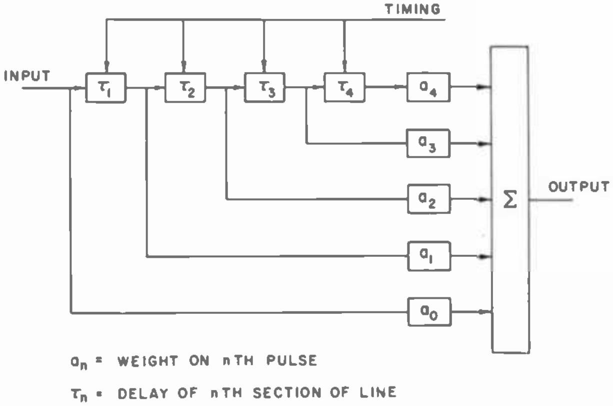

Fig. 1—Delay-line canceller.

System Response of Delay-Line Canceller

In this section, the system response of a delay-line canceller for a coherent pulsed radar using amplitude weights and staggered pulses is developed. Fig. 1 shows a block diagram of the delay-line canceller analyzed, where a_n is the amplitude weight of the n^{th} pulse and τ_n corresponds to the delay of the n^{th} section of line. These delays match the interpulse periods of the finite pulse train.

If an impulse $\delta(t)$ is applied at the input, the response of the delay-line canceller will be

$$\begin{aligned} h(t) &= a_0\delta(t) + a_1\delta(t-\tau_1) + a_2\delta(t-\tau_1-\tau_2) \\ &\quad + a_3\delta(t-\tau_1-\tau_2-\tau_3) + \cdots \\ &\quad + a_{N-1}\delta(t-\tau_1-\tau_2-\cdots\tau_{N-1}) \\ &= \sum_{k=0}^{N-1} a_k\delta(t-t_k), \end{aligned} \qquad [1]$$

where $t_k = \tau_1 + \tau_2 + \cdots + \tau_k$ and N is the number of pulses. The corresponding voltage transfer function $H(\omega)$, found by taking the Fourier transform of Eq. [1], is given by

$$H(\omega) = \sum_{k=0}^{N-1} a_k \exp\{-j\omega t_k\} \qquad [2]$$

The power transfer function $P(\omega)$ for the N-pulse canceller is then

$$\begin{aligned} P(\omega) &= |H(\omega)|^2 \\ &= \left[\sum_{i=0}^{N-1} a_i \cos \omega t_i\right]^2 + \left[\sum_{j=0}^{N-1} a_i \sin \omega t_i\right]^2 \\ &= \sum_{i=0}^{N-1} \sum_{j=0}^{N-1} a_i a_j \cos \omega (t_j - t_i). \end{aligned} \qquad [3]$$

If the system response to a stationary target ($\omega = 0$) is zero, the a's are such that

$$\sum_{i=0}^{N-1} \sum_{j=0}^{N-1} a_i a_j = 0. \qquad [4]$$

Dividing Eq. [3] by $\sum_{i=0}^{N-1} \alpha_i^2$ gives the normalized power transfer function for the N-pulse delay-line canceller; thus

$$\underline{P}(\omega) = \frac{\sum_{i=0}^{N-1} \sum_{j=0}^{N-1} a_i a_j \cos \omega (t_j - t_i)}{\sum_{j=0}^{N-1} a_i^2}, \qquad [5]$$

where the bar under the P denotes the normalized quantity. The quantity $\sum_{i=0}^{N-1} \alpha_i^2$ is the canceller power gain for band-limited white noise.[5] This can be shown as follows. Let the input noise voltage be denoted by $N_i(t)$ so that the output noise voltage $N_o(t)$ can be expressed as

$$N_o(t) = \sum_{j=0}^{N-1} a_j N_i(t - t_j). \qquad [6]$$

The average power output is then

$$\overline{N_o^2(t)} = \sum_{j=0}^{N-1} \sum_{k=0}^{N-1} a_j a_k \overline{N_i(t - t_j) N_i(t - t_k)}$$

$$= \overline{N_i^2(t)} \sum_{k=0}^{N-1} a_k^2, \qquad [7]$$

which shows the stated relationship.

To determine the relationship between the amplitude weights for the canceller shown in Fig. 1 and those for N cascaded single-delay-line cancellers of the constant-prf type, the system response for the latter is derived. A block diagram for a single canceller is shown in Fig. 2.

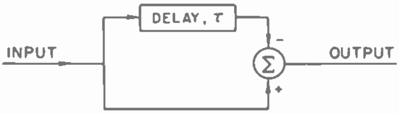

Fig. 2—Block diagram of single-delay-line canceller.

The impulse response for this canceller is simply

$$h(t) = \delta(t) - \delta(t - \tau), \qquad [8]$$

and the corresponding transfer function is

$$H(\omega) = 1 - \exp\{-j\omega\tau\}. \qquad [9]$$

When N such stages are cascaded, the overall response for the constant-prf case becomes

$$\begin{aligned} H(\omega) &= (1 - \exp\{-j\omega\tau\})^N \\ &= 1 - \binom{N}{1} \exp\{-j\omega\tau\} + \binom{N}{2} \exp\{-j2\omega\tau\} - \\ &\binom{N}{3} \exp\{-j3\omega\tau\} + \cdots + (-1)^k \binom{N}{k} \exp\{-jk\omega\tau) \cdots \\ &+ (-1)^N \exp\{-jN\omega\tau\}, \end{aligned} \qquad [10]$$

where

$$\binom{N}{k} = \frac{N(N-1)(N-2)\cdots(N-k+1)}{1\cdot 2\cdot 3\cdots k}.$$

This shows that the weights a_n in Eq. [1] and Fig. 1 are the binomial coefficients for the periodic pulse train.

Signal-to-Clutter Gain and Subclutter Visibility

The signal-to-clutter gain $G(\omega_d)$ of a clutter canceller is defined as

$$G(\omega_d) = \frac{\text{output signal-to-clutter power ratio}}{\text{input signal-to-clutter power ratio}} \qquad [11]$$

Subclutter visibility of a radar is the average of this quantity over a given range of Doppler frequencies. Although $G(\omega)$ has been previously derived for the delay-line canceller,[5,7,9] it is developed here for clarity and completeness.

For the N-pulse canceller, the output voltage $E_o(t)$ is the weighted sum of N pulse returns. Thus

$$E_o(t) = \sum_{j=0}^{N-1} a_j E(t_j), \qquad [12]$$

where a_j is the amplitude weight on the j^{th} pulse. $E(t_j)$ is the voltage of the j^{th} pulse consisting of signal and noise components where t_j denotes the time, $t - t_j$. $E(t_j)$ can be expressed in the form

$$E(t_j) = \sqrt{2S}\cos(\omega_d t_j + \psi) + \sqrt{C(t_j)}, \qquad [13]$$

where

S = signal power (into unit resistor)

ω_d = angular doppler frequency

ψ = arbitrary signal phase

C = clutter power (into unit resistor)

The average power output from the canceller is given by

$$\overline{E_o^2} = \overline{\left[\sum_{i=0}^{N-1} a_i E(t_i)\right]\left[\sum_{j=0}^{N-1} a_j E(t_j)\right]}, \qquad [14]$$

where the bar over the quantity denotes its expected value. Expanding the right-hand member of Eq. [14], assuming that the signal and clutter are independent, results in the output power,

$$\begin{aligned}\overline{E_o^2} &= 2S \overline{\sum_{i=0}^{N-1} \sum_{j=0}^{N-1} a_i a_j \cos(\omega_d t_i + \psi_i) \cos(\omega_d t_j + \psi_j)} \qquad [15]\\ &+ \overline{\sum_{i=0}^{N-1} \sum_{j=0}^{N-1} a_i a_j \sqrt{C(t_i)}\,\sqrt{C(t_j)}}\\ &= S \sum_{i=0}^{N-1} \sum_{j=0}^{N-1} a_i a_j \cos \omega_d (t_j - t_i) + C \sum_{i=0}^{N-1} \sum_{j=0}^{N-1} a_i a_j \rho(t_j - t_i),\end{aligned}$$

where $\rho(t)$ is the clutter autocorrelation function normalized so that $\rho(0) = 1$. From Eq. [15], the output signal-to-clutter ratio for the N-pulse canceller can be expressed as

$$\left(\frac{S}{C}\right)_o = \frac{S \sum_{i=0}^{N-1} \sum_{j=0}^{N-1} a_i a_j \cos \omega_d (t_j - t_i)}{C \sum_{i=0}^{N-1} \sum_{j=0}^{N-1} a_i a_j \rho(t_j - t_i)}. \qquad [16]$$

The corresponding signal-to-clutter gain becomes

$$G(\omega_d) = \frac{(S/C)_o}{(S/C)} = \frac{\sum_{i=0}^{N-1} \sum_{j=0}^{N-1} a_i a_j \cos \omega_d (t_j - t_i)}{\sum_{i=0}^{N-1} \sum_{j=0}^{N-1} a_i a_j \rho(t_j - t_i)}. \qquad [17]$$

The average value of $G(\omega_d)$ with respect to doppler frequency is found by rewriting Eq. [17] as

$$\overline{G(\omega_d)} = \frac{\overline{\sum_{i=0}^{N-1} a_i^2 + \sum_{\substack{i \\ i \neq j}}^{N-1} \sum_{j}^{N-2} a_i a_j \cos \omega_d (t_i - t_j)}}{\sum_{i=0}^{N-1} \sum_{j=0}^{N-1} a_i a_j \rho (t_j - t_i)}. \qquad [18]$$

Since the second term in the numerator of Eq. [18] averages to zero, the average value of $G(\omega_d)$ is given by

$$\bar{G} = \frac{\sum_{i=0}^{N-1} a_i^2}{\sum_{i=0}^{N-1} \sum_{j=0}^{N-1} a_i a_j \rho (t_j - t_i)}. \qquad [19]$$

Using $\overline{G}$ as given by Eq. [19] and the system gain $\underline{P}(\omega)$ as defined in Eq. [5], the signal-to-clutter gain $G(\omega_d)$ can be written as

$$G(\omega_d) = \bar{G} \cdot \underline{P}(\omega_d)$$

$$= \frac{\sum_{i=0}^{N-1} a_i^2}{\sum_{i=0}^{N-1} \sum_{j=0}^{N-1} a_i a_j \rho (t_j - t_i)} \cdot \frac{\sum_{i=0}^{N-1} \sum_{j=0}^{N-1} a_i a_j \cos \omega_d (t_j - t_i)}{\sum_{i=0}^{N-1} a_i^2}. \qquad [20]$$

Thus $G(\omega_d)$ is expressed in terms of a quantity $\overline{G}$ that is independent of target velocity and another quantity $\underline{P}(\omega_d)$ that is independent of the clutter characteristics. The quantity $\overline{G}$ is called the reference gain and is seen to depend on the amplitude weights a_i, the clutter correlation function $\rho(\tau)$ and the number of pulses, N.

Reference Gain for Periodic Pulse Train

Assuming a periodic pulse train and binomial amplitude weighting, the reference gain $\bar{G}$ will be calculated for use as a measure of performance. For the above conditions, the reference gain can be expressed by

$$\overline{G} = \frac{\sum_{j=0}^{M} a_j^2}{\sum_{i=0}^{M} \sum_{j=0}^{M} a_i a_j \rho[(j-k)T]}, \qquad [21]$$

where

$M = N - 1$

$N =$ number of pulses

$a_j = (-1)^j \binom{M}{j}$

$T =$ period of pulse train.

Eq. [21] can be rewritten as

$$\overline{G} = \frac{\sum_{j=0}^{M} \binom{M}{j}^2}{\sum_{j=0}^{M} \binom{M}{j}^2 \rho(0) + \sum_{j}\sum_{k}\limits_{j \neq k} (-1)^{j+k} \binom{M}{j}\binom{M}{k} \rho[(j-k)T]}$$

$$= \frac{1}{1 + 2\sum_{k=1}^{M} \frac{(M!)^2(-1)^k}{(M+k)!(M-k)!}\rho(kT)}. \qquad [22]$$

Eq. [22] is derived through use of the relations

$$\sum_{j=0}^{n} \binom{n}{j}^2 = \binom{2n}{n} = \frac{(2n)!}{(n!)^2}$$

and

$$\sum_{k=0}^{n-p} \binom{n}{k}\binom{n}{p+k} = \frac{(2n)!}{(n-p)!\,(n+p)!}.$$

In the case of Gaussian clutter, the autocorrelation function is

$$\rho(\tau) = \exp\{-2\pi^2\sigma^2\tau^2\}, \qquad [23]$$

where σ is the standard deviation of the clutter spectrum. A tabulation of the reference gain is shown in Table 1 as a function of the spectral spreading factor σT. The corresponding plot of this data is shown in Fig. 3.

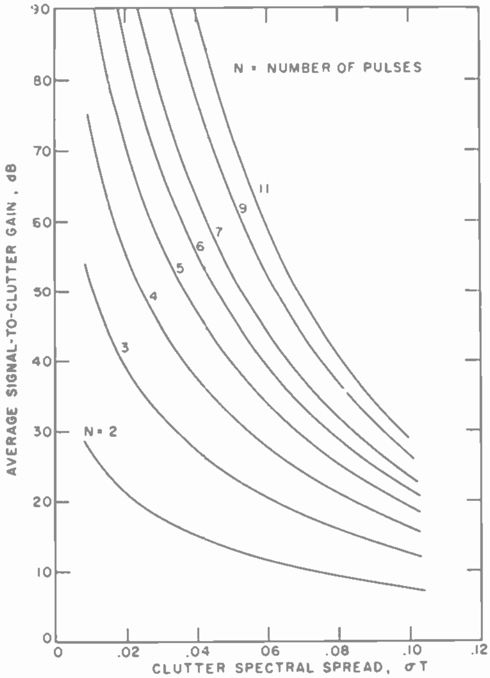

SIGNAL-TO-CLUTTER GAIN WITH PERIODIC BINOMIALLY WEIGHTED PULSES

Fig. 3—Signal-to-clutter gain with periodic binomially weighted pulses.

Optimum Pulse Weights

The criteria used to determine the optimum set of weights for a given number of pulses is that which maximizes the reference gain for a specified clutter model. Maximization of the reference gain expressed by Eq. [19] is obtained by minimizing the denominator with respect to a_i under the constraint that the numerator Σa_i^2 is a constant. Using

Table 1—Signal-to-Clutter Gain with Periodic Binomially Weighted Pulses

σT	$N = 2$	3	4	5	6	7	9	11
0.010	27.05 dB	51.10	73.39	94.44	114.52	133.79	167.25	184.76 dB
0.015	23.53	44.07	62.86	80.41	97.01	112.83	142.73	164.85
0.020	21.04	39.10	55.42	70.51	84.65	98.03	122.92	145.74
0.025	19.11	35.25	49.67	62.87	75.14	86.64	107.85	127.12
0.030	17.54	32.13	45.00	56.67	67.43	77.44	95.70	112.09
0.035	16.22	29.49	41.08	51.48	60.98	69.76	85.59	99.62
0.040	15.07	27.23	37.71	47.03	55.47	63.20	77.00	89.07
0.045	14.07	25.24	34.77	43.15	50.67	57.51	69.58	80.00
0.050	13.17	23.48	32.16	39.72	46.45	52.52	63.11	72.13
0.055	12.37	21.90	29.83	36.67	42.70	48.09	57.40	65.22
0.060	11.64	20.46	27.72	33.92	39.34	44.14	52.34	59.13
0.065	10.97	19.16	25.82	31.44	36.31	40.59	47.82	53.73
0.070	10.35	17.96	24.07	29.18	33.56	37.38	43.77	48.92
0.075	9.78	16.87	22.48	27.12	31.07	34.48	40.12	44.62
0.080	9.26	15.85	21.01	25.24	28.79	31.85	36.83	40.76
0.085	8.76	14.91	19.66	23.50	26.71	29.44	33.86	37.29
0.090	8.30	14.03	18.40	21.91	24.80	27.25	31.16	34.17
0.095	7.87	13.21	17.24	20.44	23.05	25.24	28.71	31.35
0.100	7.47	12.45	16.16	19.07	21.44	23.40	26.48	28.80

the method of Lagrangian multipliers, the quantity

$$\phi = \sum_{i=0}^{N-1} \sum_{j=0}^{N-1} a_i a_j \rho(t_j - t_i) - \lambda \sum_{i=0}^{N-1} a_i^2 \qquad [24]$$

is formed, where λ is the Lagrangian multiplier. Differentiation of Eq. [24] with respect to a_i results in the following condition for an extremum:

$$\frac{\partial \phi}{\partial a_i} = 2 \sum_{j=0}^{N-1} a_j \rho(t_j - t_i) - 2\lambda a_i = 0, \qquad [25]$$

where $i = 0, 1, 2, \cdots N-1$.

The condition for a minimum of ϕ is then[10]

$$D_k = \begin{vmatrix} f_{00} & f_{01} & f_{02} \cdots & f_{0k} \\ f_{10} & f_{11} & f_{12} \cdots & f_{1k} \\ f_{20} & f_{21} & f_{22} \cdots & f_{2k} \\ \cdot & \cdot & \cdot & \cdot \\ \cdot & \cdot & \cdot & \cdot \\ \cdot & \cdot & \cdot & \cdot \\ f_{k0} & f_{k1} & f_{k2} \cdots & f_{kk} \end{vmatrix} > 0 \qquad [26]$$

where $f_{ij} = \partial^2\phi/\partial a_i \partial a_j$, for $0 \leqslant k \leqslant N-2$, and D_{N-1} may equal zero.[10] Eqs. [25] possess a nontrivial solution for the set of a_i if

$$\begin{vmatrix} \rho(0) - \lambda & \rho(t_1 - t_0) & \rho(t_2 - t_0) \cdots & \rho(t_{N-1} - t_0) \\ \rho(t_0 - t_1) & \rho(0) - \lambda & \rho(t_2 - t_1) \cdots & \rho(t_{N-1} - t_1) \\ \rho(t_0 - t_2) & \rho(t_1 - t_2) & \rho(0) - \lambda \cdots & \rho(t_{N-1} - t_2) \\ \cdot & \cdot & \cdot & \cdot \\ \cdot & \cdot & \cdot & \cdot \\ \cdot & \cdot & \cdot & \cdot \\ \rho(t_0 - t_{N-1}) & \rho(t_1 - t_{N-1}) & \cdots \quad \cdots & \rho(0) - \lambda \end{vmatrix} = 0. \qquad [27]$$

The values of λ that satisfy the above determinental equation are the eigenvalues of the clutter covariance matrix R,

$$R = [\rho(t_j - t_i)]. \qquad [28]$$

That the resultant reference gain $\overline{G}$ is equal to the reciprocal of the smallest eigenvalue of the covariance matrix can be seen from the following.[8] Let the reference gain be expressed as

$$\overline{G} = \frac{\sum_{i=0}^{N-1} a_i^2}{\sum_{i=0}^{N-1} \sum_{j=0}^{N-1} a_i a_j \rho(t_j - t_i)} = \frac{A'A}{A'RA}, \qquad [29]$$

where A is the column matrix $\{a_i\}$ and A' its transpose. Since the covariance matrix satisfies the relationship

$$RA = \lambda A, \qquad [30]$$

from Eq. [29], the reference gain is

$$\overline{G} = \frac{A'A}{A'\lambda A} = 1/\lambda. \qquad [31]$$

Then the optimum set of weights $\{a_i\}$ is any eigenvector corresponding to the minimum eigenvalue λ.

Use was made of a subroutine within the main computer program to determine the minimum eigenvalue λ. The numerical procedure, known as the "power method," produces the largest eigenvalue and a corresponding eigenvector by iteration.[11] Hence, to use this method, it is necessary to rewrite Eq. [30] as

$$A = \lambda R^{-1} A,$$

or

$$MA = kA, \qquad [32]$$

where $M = R^{-1}$ and $k = 1/\lambda$. Thus the eigenvalue k corresponds to the reference gain $\overline{G}$.

Although the signal-to-clutter gain and reference gain given by Eqs. [17] and [19], respectively, were developed considering signal and clutter only, the effects of thermal noise can also be taken into account with the inclusion of the noise autocorrelation function. Thus Eq. [17] for the signal-to-clutter gain with noise included becomes

$$G(\omega_d) = \frac{\sum_{i=0}^{N-1} \sum_{j=0}^{N-1} a_i a_j \cos \omega_d (t_j - t_i)}{\sum_{i=0}^{N-1} \sum_{j=0}^{N-1} a_i a_j \left\{ \rho_c(t_j - t_i) + \frac{N_o}{C} \rho_N(t_j - t_i) \right\}} \qquad [33]$$

and the corresponding reference gain (Eq. [19]) becomes

$$\overline{G} = \frac{\sum_{i=0}^{N-1} a_i^2}{\sum_{i=0}^{N-1} \sum_{j=0}^{N-1} a_i a_j \left\{ \rho_c(t_j - t_i) + \frac{N_o}{C} \rho_N(t_j - t_i) \right\}} \qquad [34]$$

where $\rho_c(\ ) =$ clutter autocorrelation function

$\rho_N(\ ) =$ noise autocorrelation function

$N_o/C =$ noise-to-clutter power ratio

If band-limited white noise is assumed, the correlation function is

$$\rho_N(t_j - t_i) = \frac{\sin \pi B(t_j - t_i)}{\pi B(t_j - t_i)} \qquad [35]$$

where B is the video bandwidth. For the pulse spacings normally used, $B(t_j - t_i)$ will be large for all values of $t_j - t_i$ except for $j = i$, so that the correlation function can be approximated by

$$\rho_N(t_j - t_i) = \delta_{ij}, \qquad [36]$$

where δ_{ij} is the Kronecker delta ($\delta_{ij} = 1$ when $i = j$ and $\delta_{ij} = 0$ when $i \neq j$). Thus the ratio N_o/C will be added to the diagonal elements of the autocorrelation matrix so that the reference gain can be written as

$$G = \frac{\sum_{i=0}^{N-1} a_i^2}{\sum_{i=0}^{N-1} \sum_{j=0}^{N-1} a_i a_j \rho_c(t_j - t_i) + \frac{N_o}{C} \sum_{i=0}^{N-1} a_i^2},$$

or

$$\overline{G} = \frac{\overline{G'}}{1 + (N_o/C)\overline{G'}}, \qquad [37]$$

where $\overline{G'}$ is the signal-to-clutter power gain without thermal noise. A plot of Eq. [37] is shown in Fig. 4, where the overall reference gain $\overline{G}$ has been plotted as a function of the noise-to-clutter ratio and the reference gain with no noise.

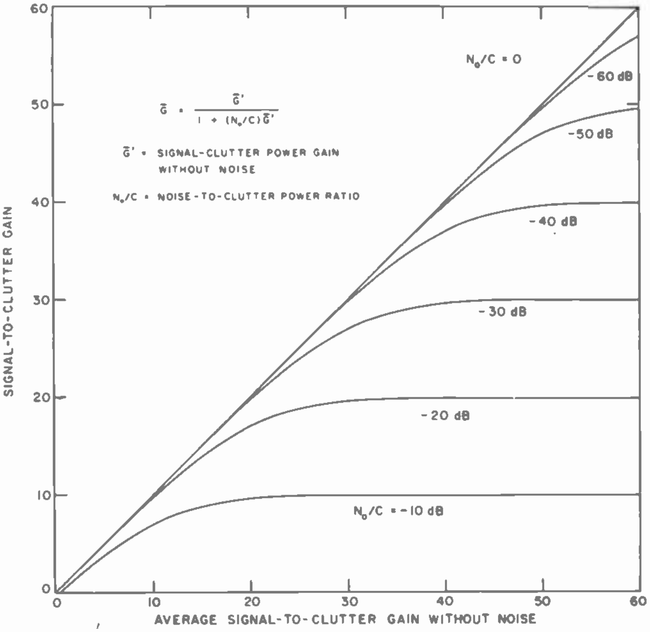

Fig. 4—Signal-to-clutter gain with band-limited white noise.

Choice of Interpulse Spacings

With a staggered-prf system, there is the problem of determining a set of interpulse spacings that result in no blind speeds over a given Doppler interval. The first blind speed occurs when the interpulse periods T_1, T_2, $\cdots$ T_N as shown in Fig. 5, satisfy the equalities

$$i/T_1 = j/T_2 = k/T_3 = \cdots n/T_N, \qquad [38]$$

where i, j, k, $\cdots$ n are integers.

Fig. 5—Staggered pulse train.

A graphical method is devised to choose a proper set of interpulse periods. If for a given set of periods as shown in Fig. 5, the products $\alpha T_1, \alpha T_2, \cdots$ are all integers, then α will correspond to a blind Doppler frequency. Fig. 6 shows a family of lines $f(T) = \alpha T$, where α denotes a normalized doppler frequency and T the normalized interpulse period. Use of this prf stagger chart is as follows.

[1] Normalize the repetition periods by dividing by one of the periods T_k (T_k could be the minimum period).

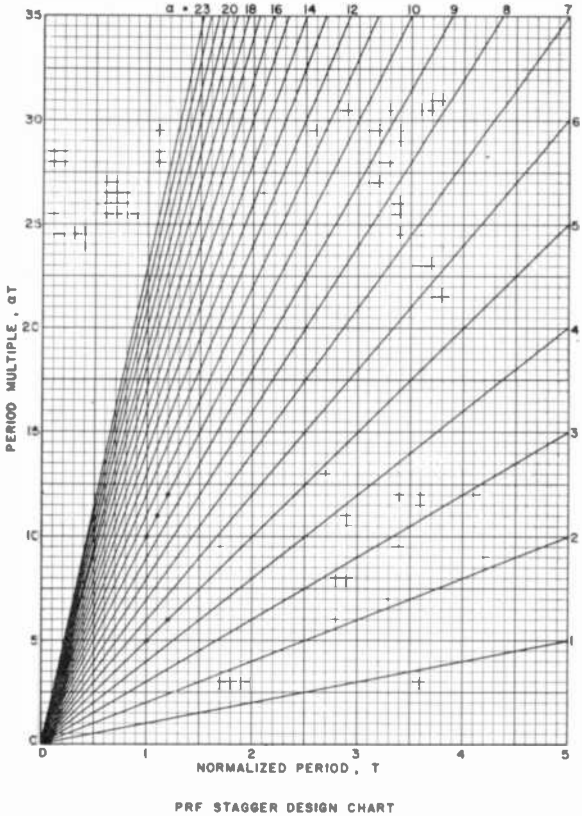

Fig. 6—PRF stagger design chart.

[2] On the design chart draw the vertical lines $T=1$, T_2/T_1, T_3/T_1, etc. $(k=1)$.

[3] The periods T_i are chosen so that all T_i do not intersect the sloping lines at integer values on the ordinate scale, αT.

[4] The sloping lines correspond to the normalized frequency at which the blind speeds will occur. The normalizing factor is the reciprocal of the scale factor on T. (If $T=1$ corresponds to one millisecond, multiply the factor α by 1000.)

[5] As an example, consider the normalized periods $T=1.0$, 1.2 (assume T in msec, see Fig. 6). The vertical lines $T=1$, $T=1.2$ will intersect the sloping line $\alpha=5$ at the integer values $\alpha T=5$ and $\alpha T=6$. For this case, the first blind speed will correspond to a Doppler frequency of 5000 Hz. When $T=1.0$, 1.2, and 1.1 (T in msec), the first blind speed will occur at 10,000 Hz where all three periods have an integer multiple, $\alpha T=10$, 12, and 11.

Partial nulls or holes will occur in the Doppler frequency response as calculated by use of Eq. [17] when the values, αT_k, are nearly integers. In this case, the periods can be slightly shifted to obtain a smoother frequency response without the partial nulls.

Calculated Results

Uniform Period Pulse Train

The signal-to-clutter gain has been calculated for periodic pulse trains of three, four, and five pulses using binomial amplitude weighting. Results of these calculations are shown in Fig. 7 for pulses that are spaced by one millisecond and correspond to responses obtained by cascading $N-1$ ($N=3$, 4, 5) single-delay-line cancellers. Values of the clutter standard deviation (bandwidth), σ, of 15 Hz and a carrier frequency of 1300 MHz were used in the calculations. This value of σ corresponds to rain-cloud clutter.

Fig. 8 shows curves of signal-to-clutter gain when optimized weights are used for the uniformly spaced pulse train. The amplitude weights obtained from the solution of Eq. [27] for the minimum λ is shown in Table 2. A Gaussian clutter autocorrelation function of the form

Table 2—Optimum Weights for Periodic Pulse Train

N	a_0	a_1	a_2	a_3	a_4
3	1.00000	−1.99119	1.00000		
4	1.00000	−2.97363	2.97363	−1.00000	
5	1.00000	−3.94740	5.89504	−3.94740	1.00000

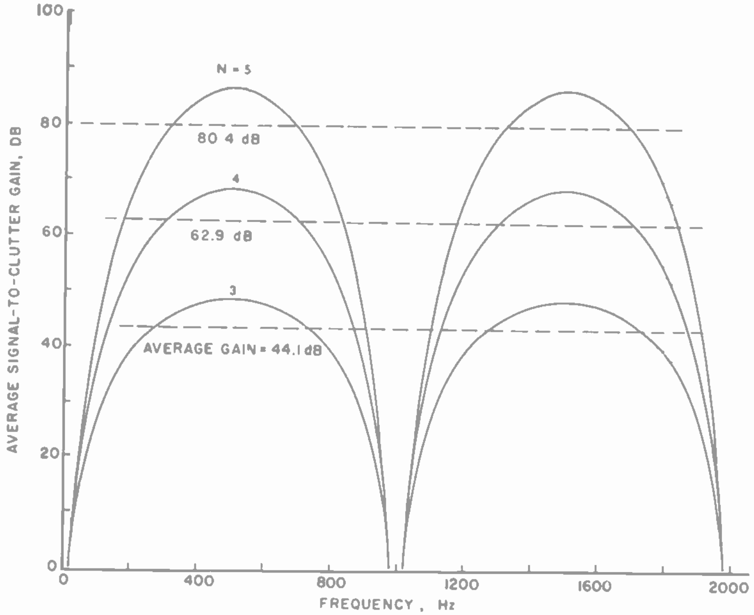

Fig. 7—Signal-to-clutter gain for uniformly spaced pulses using binomial weighting.

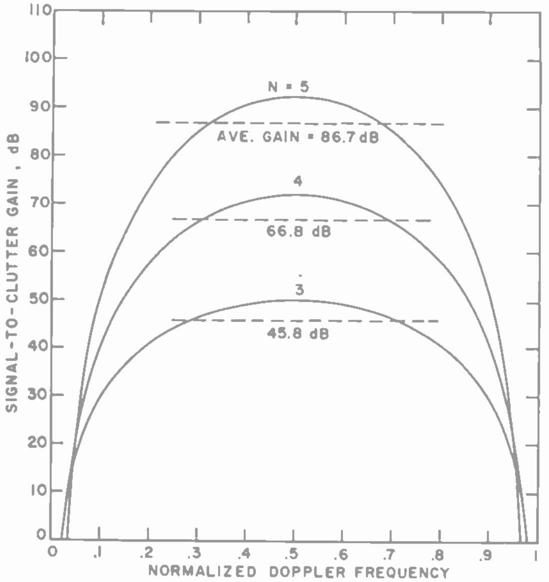

Fig. 8—Signal-to-clutter gain for uniformly spaced pulses with optimized weighting.

given by Eq. [23] has been used in the calculations The amplitude weights given in Table 2 are seen to be very nearly equal to the binomial coefficients. It is noted that the improvement obtained in the signal-to-clutter gain by use of optimum weighting over the normal binomially weighted case is relatively small.

Staggered Pulse Train

The signal-to-clutter gain characteristic for a typical 3-pulse train with prf stagger and optimized weighting is shown in Fig. 9. Blind speeds occur at velocities corresponding to frequencies that are multiples of 5 kHz for the particular set of spacings that were used for the pulses. The average gain obtained is seen to be very nearly that for the constant-prf case with binomial weighting. With binomial weighting applied to this case, the shape of the Doppler response will be about the same as in Fig. 9, but the average gain will be reduced by approximately 5 dB.

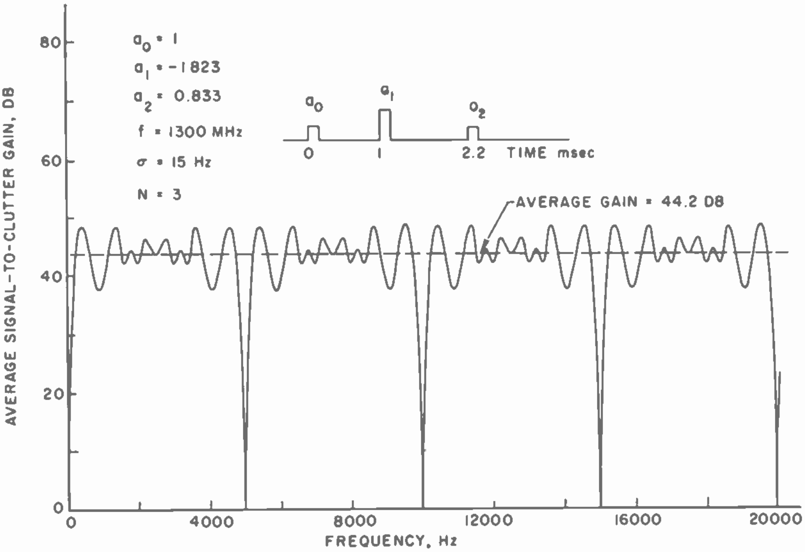

Fig. 9—Signal-to-clutter gain with prf stagger and optimized pulse weighting, $N = 3$.

A similar curve is shown in Fig. 10 for the four-pulse staggered-prf case with optimum weighting of the pulses. Here, the time spacing of the additional pulse was chosen to eliminate the 5 kHz Doppler null that occurred in the three-pulse response of Fig. 9. Use of binomial weighting with the prf's chosen for the four-pulse case results in a reference gain of 43 dB.

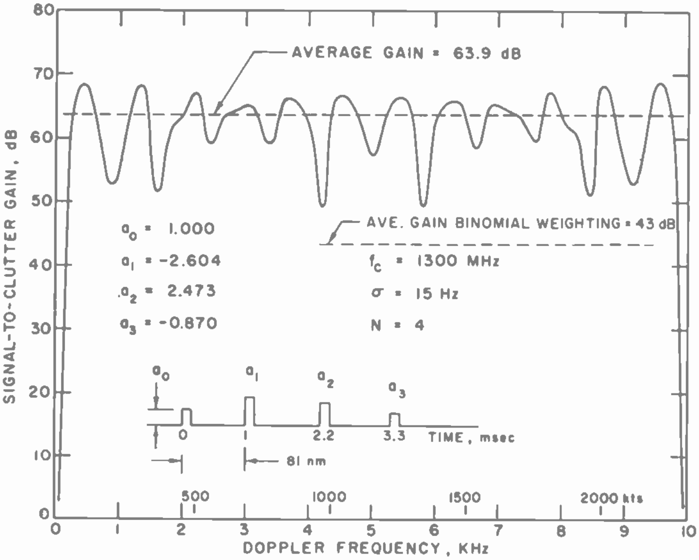

Fig. 10—Signal-to-clutter gain with prf stagger and optimized pulse weighting, $N = 4$.

A typical example of signal-to-clutter gain using five staggered pulses with optimized weighting is shown in Fig. 11. Using these spacings and binomial weighting, the reference gain drops to 72.5 dB. With such high average signal-to-clutter gains, effects such as noise and system stability become important. Figs. 9 to 11 show typical signal-to-clutter gain characteristics for the three-, four- and five-pulse cases.

The optimum weights for a given set of pulse spacings vary somewhat with the spectral width of the clutter. Fig. 12 shows the average signal-to-clutter gain obtained with optimum weighting of a four-pulse train as a function of the standard deviation of the clutter spectrum. As shown in Table 3, the optimum weights do not vary significantly over the range of clutter widths used. A curve of the average gain obtained using the optimum weights for $\sigma = 15$ Hz and shown in Fig. 12 indicates that, except for narrow clutter spectra, a fixed set of weights can be used to obtain near optimum performance.

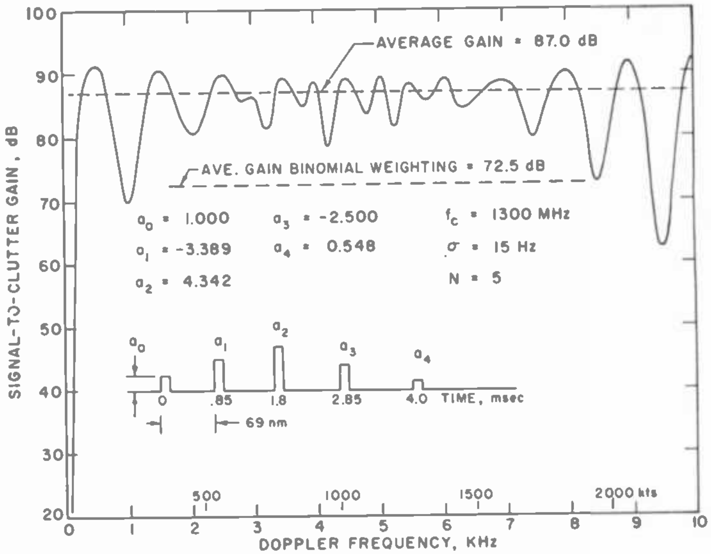

Fig. 11—Signal-to-clutter gain with prf stagger and optimized pulse weighting, $N = 5$.

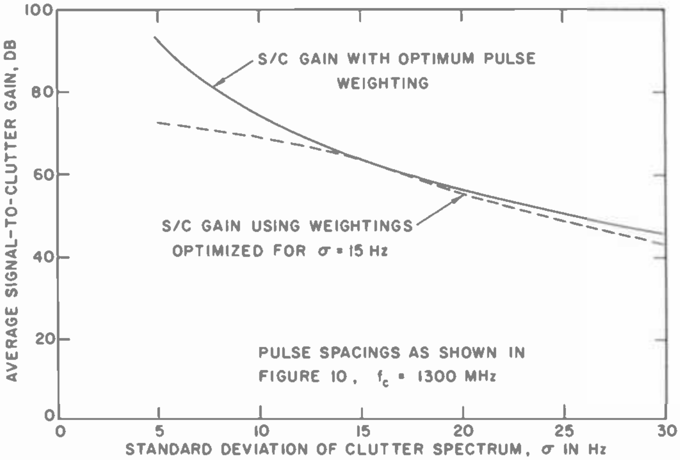

Fig. 12—Signal-to-clutter gain as function of clutter spectral width for four-pulse canceller.

Table 3—Optimum Amplitude Weights as Functions of Clutter Spectral Width ($N = 4$, $f_o = 1300$ MHz)

Clutter Spectral Width, σ (Hz)	a_0	a_1	a_2	a_3
5	1.0000	−2.6275	2.4970	−.8696
10	1.0000	−2.6186	2.4881	−.8696
15	1.0000	−2.6039	2.4735	−.8696
20	1.0000	−2.5837	2.4533	−.8696
25	1.0000	−2.5583	2.4279	−.8695
30	1.0000	−2.5280	2.3976	−.8695

There will be variations in the optimum reference gain as different pulse spacings are chosen for a given number of pulses. A comparison of the reference gains for optimumly weighted cases indicates gain differences of as much as 7 dB for the four- and five-pulse cancelling systems. Fig. 13 shows the average or reference gain that might be

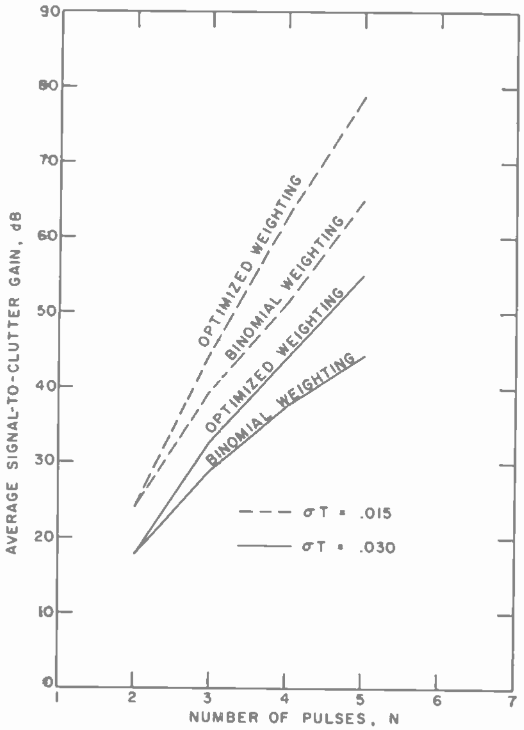

Fig. 13—Signal-to-clutter gain with prf stagger and pulse weighting.

expected with prf staggering and pulse amplitude weighting as a function of the number of pulses and the σT product for both optimum and binomial weighting.

Calculated Results Including Noise

The effect of sources of noise other than clutter is to add a bias term to the denominator of the function representing the signal-to-clutter gain. As shown in Fig. 4, this bias term is a constant for a given thermal noise level and limits the maximum available signal-to-clutter gain. If white noise is assumed, the signal-to-clutter gain characteristic with noise plus clutter will have a shape with respect to frequency similar to that for the case with clutter alone. It is found that the minimum eigenvalue, λ, is unaffected by the presence of the N_o/C bias term in the autocorrelation function, so that the pulse weights for the case where there is thermal noise are the same as for the case without thermal noise.* Figs. 14 and 15 show the signal-to-clutter gain characteristics for the four-pulse canceller with noise-to-clutter ratios of −40 and −60 dB, respectively. In these figures, the average gains as obtained with binomial weighting are also shown.

Effect of Limiting on Signal-to-Clutter Gain

The effect of a limiter prior to clutter cancellation is to reduce the signal-to-clutter gain from the value obtainable without limiting. To show the reduced clutter gain for optimized and binomial type of pulse weights, a clutter correlation function with limiting was implemented in the computer program. The following assumptions have been made in the formulation of the clutter correlation function:

[1] Error function type of limiter,

[2] Ideal band-pass filter with no response to harmonics outside the intermediate frequency band,

[3] Gaussian input clutter.

With these assumptions, the clutter correlation function can be expressed as[12,13]

$$\rho_c(\tau) = \frac{1}{A} \sum_{n=0}^{\infty} \frac{[(2n)!]^2}{2^{4n}(n!)^3(n+1)!} \cdot \frac{\exp\{-2(2n+1)\pi^2\sigma^2\tau^2\}}{\left(1+\dfrac{2}{\pi}x^2\right)^{2n+1}} \qquad [39]$$

---

* Note that the reference gain in this case is $1/[\lambda + (N_o/C)]$, rather than $1/\lambda$.

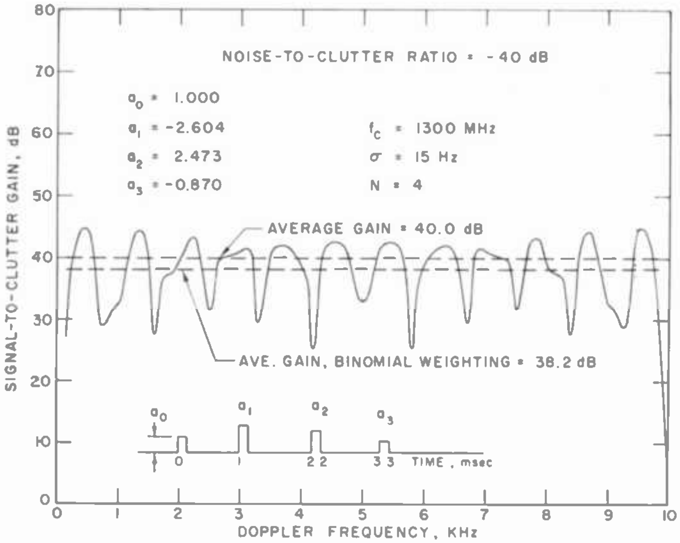

Fig. 14—Signal-to-clutter gain with prf stager and optimized pulse weighting in the presence of band-limited white noise, $N_o/C = -40$ dB.

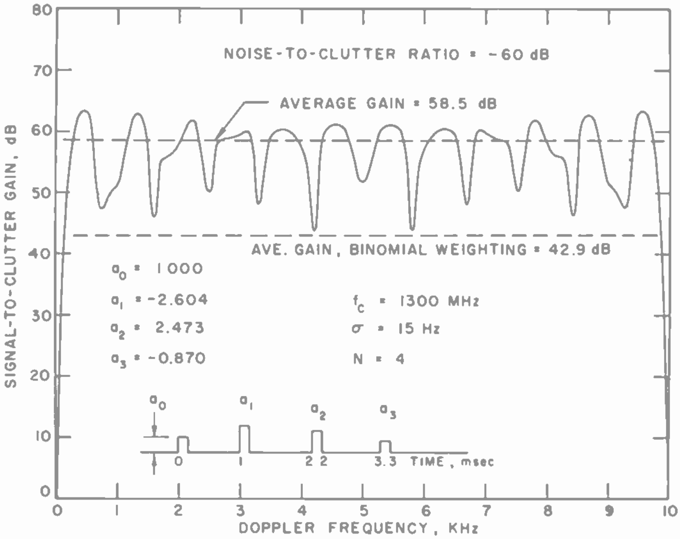

Fig. 15—Signal-to-clutter gain with prf stagger and optimized pulse weighting in the presence of band-limited white noise, $N_o/C = -60$ dB.

where

$$x = \frac{\text{limit level}}{\sqrt{\text{clutter input power}}},$$

$$A = \sin^{-1}\left[\frac{1}{1+\dfrac{2}{\pi}x^2}\right].$$

with σ and τ as defined in Eq. [23]. Using the set of optimized weights indicated in Fig. 10, the signal-to-clutter gain with limited clutter has been calculated. The general shape of the response function is as shown in Fig. 10 with a reduced average gain. A plot of the average gain as a function of limit level is shown in Fig. 16. Gain curves obtained with optimized and binomial weights are shown in this figure for comparison purposes. For values of rms clutter to limit ratios in excess of 20 dB, the effect of optimization is nullified. The optimization of pulse weight used in the above computations was calculated on the basis of no limiting of the clutter. Determination of the optimum pulse weights for a specific limit level results in a small increase in the signal-to-clutter gain. For the case considered above, the amplitude

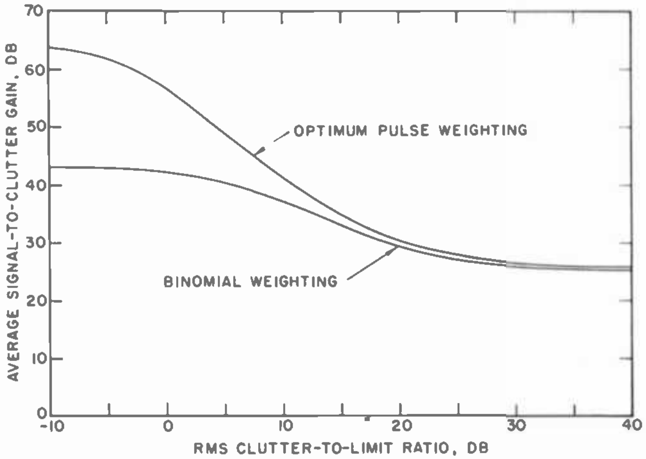

Fig. 16—Effect of limiting on signal-to-clutter gain for $N=4$.

weights optimized for limited clutter are shown in Table 4 when the rms clutter to limit level is 20 dB. The resultant increase in average signal-to-clutter gain is 0.3 dB.

Table 4—Optimized Pulse Weights With Limited Clutter ($\tau = 15$ Hz, $f_c = 1300$ MHz)

Parameter		Limited Clutter $x = -20$ dB	No Limiting
Optimized Weights	a_1	1.0000	1.0000
	a_2	−2.3770	−2.6039
	a_3	2.2074	2.4735
	a_4	−0.8293	−0.8696
Average Signal-to-Clutter Gain		30.4389	30.1376

Scaling of System Parameters

Although the examples given in the computations used a carrier frequency of 1300 MHz, and a certain pulse spacing, these same results could be applied to other cases by proper scaling. Since the optimization process involves a clutter autocorrelation function of the form

$$\rho(\tau) = \exp\{-2\pi^2\sigma^2\tau^2\}, \qquad [39]$$

where τ is a function of the interpulse period, the amplitude weights will remain unchanged. Also the signal-to-clutter response will have the same shape if the product σT, where T is the pulse period, is kept constant. Thus, if the pulse period is divided by a factor of three, σ is tripled so that for the same type of clutter, the carrier and Doppler frequencies must also be tripled.

Conclusions

The study of weighted pulse trains for use with delay-line type of clutter cancellers has shown the following:

[1] Use of optimally weighted nonperiodic pulse trains makes it possible to achieve high clutter attenuation over a relatively wide Doppler frequency interval.

[2] The signal-to-clutter gain obtained with optimum pulse weights is substantially greater than that obtained with binomial weights when noise and/or limiting is excluded.

[3] The optimum pulse weights for a given set of interpulse spacings and clutter spectral width can be used over a relatively wide range of spectral widths around the design value.

[4] Optimally weighted pulse trains for delay-line-type cancellers are most advantageous for use with systems that have wide dynamic range and are linear; under conditions of low signal-to-noise ratio or i-f limiting, the benefit of optimized pulse weighting is reduced.

References:

[1] D. K. Barton, **Radar System Analysis**, Prentice-Hall, Inc., Englewood Cliffs, N.J., 1964.

[2] R. S. Berkowitz, (Ed.): **Modern Radar Analysis, Evaluation and System Design,** Edited by R. S. Berkowitz, John Wiley and Sons, Inc., New York, N.Y., 1965.

[3] M. I. Skolnik, **Introduction to Radar Systems**, McGraw-Hill Book Co., Inc., New York, N.Y., 1962.

[4] D. F. DeLong and E. M. Hofstetter, "On the Design of Optimum Radar Waveforms for Clutter Rejection," **IEEE Trans. Information Theory,** Vol. IT-3, p. 454, July 1967.

[5] R. C. Emerson, "Some pulsed doppler MTI and AMTI techniques," **The Rand Corporation,** R-274, March 1954.

[6] R. L. Mitchell and A. W. Rihaczek, "Clutter Suppression Properties of Weighted Pulse Trains," **IEEE Trans. Aerospace and Electronic Systems,** Vol. AES-4, No. 6, p. 822, Nov. 1968.

[7] W. D. Rummler, "Clutter Suppression by Complex Weighting of Coherent Pulse Trains," **IEEE Trans. Aerospace and Electronic Systems,** Vol. AES-2, No. 6, p. 689, Nov. 1966.

[8] L. E. Brennan and I. S. Reed, "Optimum Processing of Unequally Spaced Radar Pulse Trains for Clutter Rejection," **The Rand Corporation,** p-3657, AD 657755, Aug. 1967.

[9] J. Capon, "Optimum Weighting Functions for the Detection of Sampled Signals in Noise," **IEEE Trans. Information Theory,** Vol. IT-10, No. 2, p. 152, April 1964.

[10] G. Leitman, **Optimization Techniques with Applications to Aerospace Systems,** p. 6, Academic Press, New York, N.Y., 1962.

[11] F. B. Hildebrand, **Methods of Applied Mathematics,** p. 62-65, Second Ed., Prentice-Hall, Inc., Englewood Cliffs, N.J. 1965.

[12] G. Grasso and P. F. Guarguaglini, "Clutter Residues of a Coherent MTI Radar Receiver," **IEEE Trans. Aerospace and Electronic Systems,** pp. 195-204, Vol. AES-5, No. 2, March 1969.

[13] H. R. Ward and W. W. Shrader, "MTI Performance Degradation Caused by Limiting," p. 168, East Coast Conf. Aerospace and Electronics Systems Conv. Record, Sept. 1968.

[14] T. Murakami, **Radar Clutter Attenuation,** Doctoral Dissertation, University of Pennsylvania, 1970 (Dr. R. S. Berkowitz, Dissertation Supervision); University Microfilms, Inc., Ann Arbor, Michigan, UM 70-25705.

Infrared Spectroscopic Method for Compositional Determination of Vapor-Deposited Borosilicate Glass Films and Results of Its Application

Werner Kern

RCA Laboratories, Princeton, N. J.

Abstract—An infrared analytical technique is described for rapidly and nondestructively determining the composition of binary borosilicate glass films chemically vapor deposited on silicon substrates. The principle of the method is based on a correlation of the absorbance ratio [B-O]/[Si-O] with the chemically determined composition of standard samples. The absorbance ratio is calculated from the measured B-O net absorbance maximum in the wavenumber region near 1370 cm^{-1} and the Si-O absorbance maximum at the stretching vibration frequency near 1075 cm^{-1}. Glass films up to approximately 2.5 μm thickness can be analyzed. Thicker films up to about 7 μm can be measured similarly by utilizing the net absorbance ratio of the less intense bands of B-O-Si at 917 cm^{-1} and of Si-O at 800 cm^{-1}. Applications of the method are discussed, including effects of reactor geometry on the composition of borosilicates, evidence of silicate formation during low-temperature vapor oxidation of hydrides, and the long-term stability of glass films. Changes in absorbance and wavelength positions of the infrared bands as a function of heat treatment, composition, glass densification, and film thickness are briefly discussed also.

Introduction

Vapor deposited films of borosilicate glasses prepared by a method previously described[1-3] have found extensive applications in silicon

---

Editor's note: Parts of the information in this paper were presented at the Electrochemical Society Meeting in Boston, Massachusetts, May 1968 (Paper No. 92) and in New York, N.Y., May 1969 (Paper No. RNP 372).

device technology.[3-6] A convenient analytical technique for monitoring these film compositions is therefore of considerable practical importance.

The principle of an infrared absorption technique was briefly described in previous papers;[2,7] it is based on correlation of the absorbance ratio [B-O]/[Si-O] with the chemical composition of the glass films. In our earlier work[2,7] the absorbance ratio was determined from the measured B-O net absorbance maximum in the wavelength region near 7.3 μm (1370 cm^{-1}) and the Si-O absorbance maximum at the stretching vibration frequency near 9.3 μm (1075 cm^{-1}). This method is limited to glass thicknesses up to about one micrometer. It will be shown that the infrared absorption technique can be extended to films of several micrometer thickness by using beam-attenuation techniques or by utilizing the weaker absorption peaks at 10.9 μm (917 cm^{-1}) for B-O-Si and 12.5 μm (800 cm^{-1}) for Si-O. It is not necessary to know the exact film thickness, since absorbance ratios rather than absolute values are taken.

Applications of this analytical method will be discussed for investigating effects of glass deposition parameters, silicate formation, heat treatment of films, and stability of borosilicate glass films over periods of several years.

Experimental Techniques

1. Film Substrates

The silicon wafers used as film substrate should transmit uniformly at least 50% of the infrared in the wavelength range of 3 to 14 μm without exhibiting scattering or back-to-front surface reflection phenomena. We found that uncompensated silicon of at least 100 ohm-cm resistivity made from vacuum float zone refined crystal low in oxygen fulfills these requirements if the slices have a thickness of about 0.025 inch (to avoid interference effects) and are polished on both sides. However, silicon with somewhat less ideal properties can be used as long as the substrate wafer is uniform and a piece of it is positioned in the reference beam.

2. Method of Film Deposition

Borosilicate glass films were prepared by chemical vapor deposition from nitrogen-diluted silane and diborane reacted with excess oxygen by the method described previously.[1] A small planetary hot plate reactor,[9] as well as a larger version of similar design, were used for depositing the films at a substrate temperature of 450°C. The glass composition was varied by using different diborane/silane ratios. Uniform film thicknesses in the range of typically 1 to 3 μm were deposited for most samples, with thin silicon dioxide top layers to ensure compositional stability[2] during the investigation. Appropriate corrections in the boron concentrations were made to compensate for this layer, as will be indicated.

3. Chemical Analysis

Chemical analysis of the glass films was employed to correlate the infrared data with the composition of the films. Coated silicon wafers were immersed in dilute hydrofluoric acid solution just long enough to dissolve the glass films, as evidenced by the hydrophobic behavior of the surface.[8] The solution was analyzed by complexing the BF_4^- with N-methylthionine (Azure C) and extraction of the dye with dichloroethane followed by colorimetric measurement.[10] The boron contents in the range of 0.5 to 15 μg can be determined by this method with an average deviation of ±0.2 μg. The quantity of glass used for each chemical analysis was sufficient to contain 6 to 30 μg of boron per sample for thin-film films, and 50 to 500 μg for thick film samples. The glass compositions are expressed as mole percent B_2O_3 in the glass. The SiO_2 contents were determined by difference, since previous tests had shown that no separate analysis of silicon is required for these binary borosilicates, $(B_2O_3)_x \cdot (SiO_2)_{1-x}$.

4. Infrared Spectroscopic Analysis

The following procedure is used for analyzing films up to 1.2 μm thickness: one half of each substrate wafer, stripped of glass film with diluted HF, is placed in the reference beam of a double-beam infrared recording spectrophotometer (Perkin-Elmer Model 137B). The coated half of the wafer is placed in the sample beam of the instrument. Both wafers are positioned perpendicular to the infrared beam. The instrument is set to zero absorbance by scanning the spectrum for the absorption minimum (usually in the wavelength region from 3 to 6 μm) and adjusting the reference beam attenuator for zero absorption. The spectrum is then recorded at slow scanning speed, and the absorbance values (A) of the absorption maxima read for the B-O and Si-O stretching-vibration major peaks. The baseline for the B-O peak is determined as indicated in Fig. 1, to calculate the net absorbance. The absorbance ratio (r) is calculated as follows:

$$r_{(\leq 1.2\,\mu\mathrm{m})} = \frac{\text{Net } A_{\text{B-O}} \text{ at } 7.3\,\mu\text{m}}{\text{Total } A_{\text{Si-O}} \text{ at } 9.3\,\mu\text{m}}. \qquad [1]$$

Note that the base-line absorbance for the Si-O peak is taken as zero; we found that this improves the linearity of the absorbance ratio versus composition.

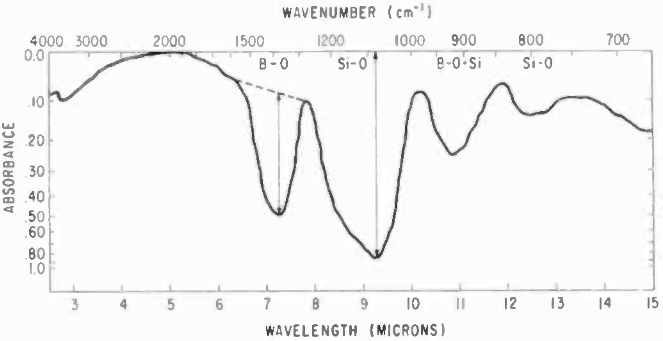

Fig. 1—Infrared absorption spectrum of a typical borosilicate glass film (0.92 μm thick) deposited by vapor oxidation of the hydrides at 450°C. The arrows indicate the net absorbance maxima for the B-O and Si-O major peaks used for ratio calculations.

Films of 1 to 2.5 μm thickness can be evaluated by the same method if the reference beam radiation is attenuated by a substantial factor, which effectively expands the absorbance scale. The peak absorbances can thereby be brought within readability. This can be accomplished by placing a metal screen* of suitable mesh size in the reference beam; widening the spectrometer slit width is advantageous.

Films in the range of 2 to about 7 μm thicknesses are best evaluated by utilizing the B-O-Si peak at 10.9 μm and the overtone Si-O peak at 12.5 μm:

$$r_{(2\text{-}7\,\mu\text{m})} = \frac{\text{Net } A_{\text{B-O-Si}} \text{ at } 10.9\ \mu\text{m}}{\text{Net } A_{\text{Si-O}} \text{ at } 12.5\ \mu\text{m}} . \qquad [2]$$

These measurements are taken with the silicon substrate blank wafer in the reference beam.

It should be noted that the exact absorption maxima may differ slightly from the typical wavelengths stated, as will be explained. The ratio values were always determined using the absorption maximum of the peaks. This technique has certain limitations,[11] but it is extremely convenient and is quite reliable for use with the empirical calibration

---

* Commercially available reference–beam attenuators of the adjustable type are particularly convenient.

curves recommended in this paper. The use of the integrated intensity of an absorption band would have greater theoretical significance as it measures the total absorption of energy by a vibration mode, but it is considerably less convenient for routine applications.

Analysis based on the ratio of infrared reflectance maxima can also be used for film thicknesses up to about 1.2 μm if suitable substrates are used, but interference effects complicate the spectra.

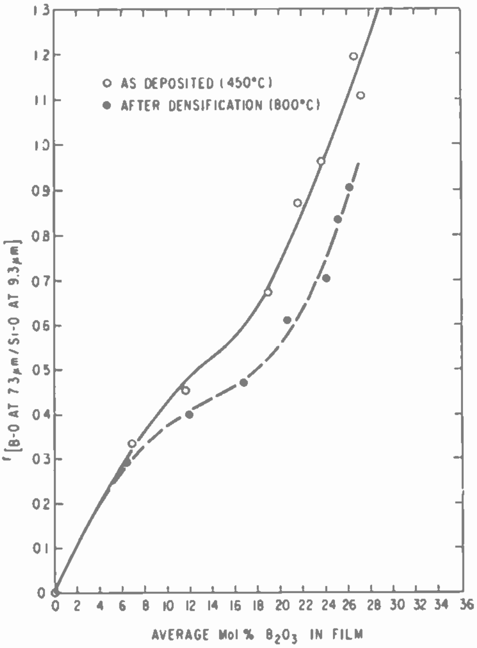

Fig. 2—Major peak absorbance ratio of SiO_2 coated borosilicate films of 1.2 to 1.3 μm thickness as a function of average boron oxide concentration in the total layer. Blank silicon substrate was used in reference beam.

Results and Discussion

1. Relationship of Film Composition and Absorbance Ratio

The range of glass compositions studied was from 0 to 30 mole percent B_2O_3. Higher boron concentrations are of little practical interest since such compositions tend to be unstable.[3]

Fig. 2 shows a plot of the absorbance ratios

$$r_{(\leq 1.2\,\mu\mathrm{m})} = \frac{\text{Net } A_{\text{B-O}} \text{ at } 7.3\ \mu\text{m}}{\text{Total } A_{\text{Si-O}} \text{ at } 9.3\ \mu\text{m}}$$

as a function of the B_2O_3 contents of the glass. The film thicknesses of these samples were 1.2 to 1.3 μm, including an SiO_2 top layer of 0.05 μm. The plot should yield a straight line if the Beer–Lambert law holds.* The resulting curve is slightly bent with an inflection point at about 17 mole percent, indicating some deviation from ideal behavior. The fact that this characteristic in the curve has been reproduced with samples made under different deposition conditions and with different film thicknesses suggests that it is real rather than caused by some analytical artifact.

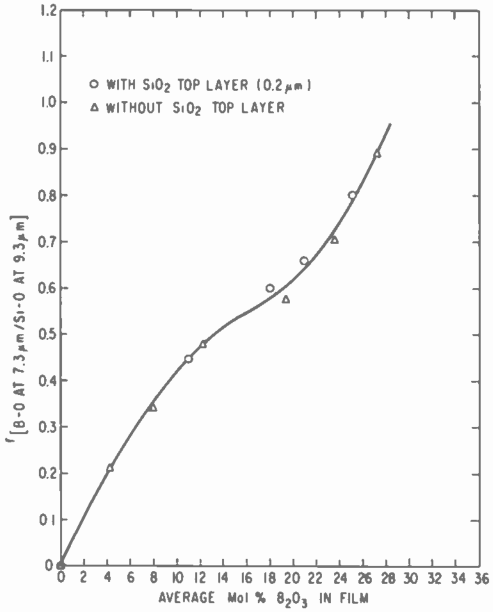

Fig. 3—Major peak absorbance ratio of SiO_2 coated borosilicate films of 2.1 to 2.6 μm thickness as a function of average boron oxide concentration in the total layer. Reference beam was attenuated with screen to 28%.

A graph of the same relationship for thicker films is presented in Fig. 3. These layers were 2.1 to 2.6 μm thick, including a 0.2 μm-thick SiO_2 top layer and very thin 0.065 μm SiO_2 base layer. The chemical analysis was made using the combined layer structure. The absorbance was measured before and after removal of the SiO_2 top layer with buffered HF etch,[12] as indicated in the figure. A metal screen of 28%

---

* The Beer–Lambert Law states that the quantity of monochromatic radiation absorbed by a material is proportional to the concentration of absorbing molecules and the thickness of the material.

transmittance was placed in the reference beam to reduce the magnitude of absorbance to readable values. The resulting curve in Fig. 3 shows again an inflection point at about 17 mole percent B_2O_3. The portion of the curve beyond this point exhibits somewhat lower absorbance ratios than those in Fig. 2 taken without the screen.

Fig. 4 shows the net absorbance ratio

$$r_{(1\text{-}2.5\ \mu m)} = \frac{\text{Net } A_{\text{B-O-Si}} \text{ at } 10.9\ \mu\text{m}}{\text{Net } A_{\text{Si-O}} \text{ at } 12.5\ \mu\text{m}}$$

as a function of the glass composition for the same series of samples. These measurements were taken with the blank silicon substrate in the reference beam, before and after removing the SiO_2 top layer. The shape of the resulting curve for the scale chosen is nearly identical with the curve in Fig. 2, although the absolute ordinate values are entirely different. It is apparent that the presence of an SiO_2 top layer in this relationship lowers the absorbance ratio significantly due to some anomaly caused by the 12.5 μm Si-O band, which is not the case

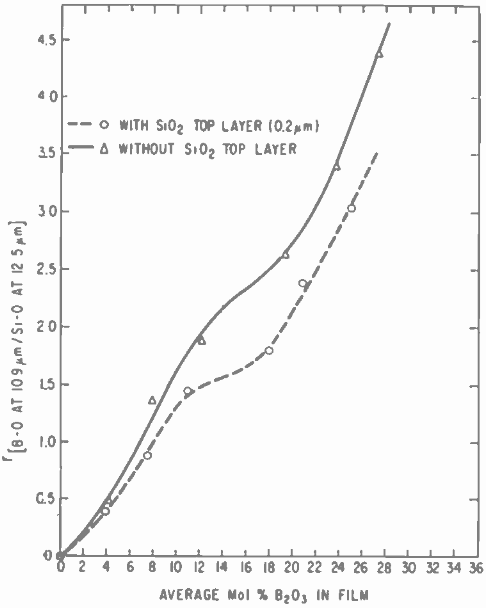

Fig. 4—Minor peak absorbance ratio of borosilicate films from Fig. 3 as a function of average boron concentration in the total layer. Blank silicon substrate was used in reference beam.

for ratios derived from the main absorbance peaks. Additional evidence that this effect is caused by the 12.5 μm Si-O band can be offered by comparing the curve obtained from the net absorbance ratio derived from the B-O band at 7.3 μm and the Si-O band at 12.5 μm: the same relative difference is manifested for the samples with and without the SiO_2 top layers. Calculations showed that the apparent absorptivity for the Si-O peak at 12.5 μm is considerably larger for the SiO_2 top layer than for that of the Si-O in the borosilicate structure, although this is not the case for separate layers. It is likely that this anomaly is caused by interface reflectivity phenomena. For thick layers where the minor absorption band is used, one should therefore preferably have no SiO_2 layers present, or else use a calibration curve prepared with samples having the same particular layer structure.

2. Calibration Curves

The use of a calibrated working curve is also recommended for the major peak ratio technique, since the ideal Beer–Lambert relation is not strictly obeyed. It is best to prepare standard samples under the same conditions and within the same thickness range as the samples to be analyzed routinely. This empirical procedure is most reliable and accurate as it will compensate for any possible effects of layer thickness, structure, film preparation, base-line determination, and instrumentation.

It should be kept in mind that the spectrophotometric accuracy falls off on both extremes of the absorbance scale.[13] One should therefore attempt to contain the absorption bands used in the analysis within the absorbance range of 0.1 to 1, or, preferably 0.2 to 0.8, by proper choice of one of the three infrared analytical techniques described, or by selecting a suitable film thickness if this is readily possible.

It is often necessary to relate the solid composition to the gas composition from which the glass was synthesized. Since this relationship is nonlinear on a mole basis, it is best to prepare a graph as shown in a previous paper[1] for the small deposition system. A convenient alternative technique for use in the laboratory consists of plotting the absorbance ratios of the glass samples directly as a function of the gas composition expressed as mole-percent diborane in the silane plus diborane before dilution. However, it must be realized that this relation is dependent upon deposition conditions for reasons discussed below. This type of working curve should therefore be considered valid only for a given reactor under fixed deposition conditions.

3. Effects of Reactor Geometry on Glass Composition

The dependence upon film deposition conditions noted above is due to effects of the geometry and wall temperature of the reaction chamber on the composition of the borosilicate glass. The formation of these glassy films is accompanied by homogeneous gas-phase nucleation,[4] which results in deposition of colloidal coatings of partially hydrated boron oxide and silicon dioxide on the wall of the deposition chamber. The boron-to-silicon ratio in these wall deposits may vary with the wall temperature and/or the wall-to-volume ratio of the reactor because of the thermodynamics of the silane and diborane oxidation reactions. The relative initiation temperature for the diborane–oxygen reaction is 110°C, as compared to 195-200°C for the silane–oxygen reaction.[14] The hydride mixture may therefore become partially depleted of boron inside the reactor. The degree of depletion is primarily a function of the temperature and relative surface area of the reactor wall.[1] For example, the solid compositions of the glass samples deposited in the large reactor (used for Figs. 3 and 4) are close to the theoretical stoichiometry, whereas those prepared with the small system (used for Fig. 2) contain considerably less boron.[1] Analogous observations have also been made for boron-doped oxides deposited under similar conditions on silicon, using sheet resistivity after diffusion as a quantitative analytical measure.[15]

4. Silicate Glass Formation as Evidenced by Infrared Spectroscopy

Borosilicate glasses are made up by interacting B_2O_3 and SiO_2 in various proportions. To examine whether glassy films of typical composition deposited at low temperature (450°C) from silane, diborane and oxygen are real borosilicates, rather than merely physical mixtures of B_2O_3 and SiO_2, we examined the infrared absorption spectra of separately vapor-deposited films of B_2O_3 and SiO_2 and then combined the samples in the infrared sample beam to obtain the combined additive spectrum. A comparison was then made with a film obtained by the usual co-oxidation of the hydrides.

Dry B_2O_3 films deposited from B_2H_6 and O_2 exhibit the strongest absorption peak at 7.94 μm (1259 cm^{-1}) due to B-O bond stretching, and a weaker symmetric band at 13.94 μm (717 cm^{-1}). These absorption modes are characteristic of vitreous B_2O_3.[16,17] Exposure of the film to moisture causes hydration of the boron oxide forming orthoboric acid, H_3BO_3. This is evident by a shift of the B-O main absorption peak to 6.82 μm (1468 cm^{-1}) and the appearance of a new sharp band at 8.38 μm (1193 cm^{-1}) and two new small peaks at 4.44 μm (2252 cm^{-1}) and 11.33 μm (883 cm^{-1}). All of these bands are characteristic of boric acid.[16] A strong absorption at 3.1 μm (3226 cm^{-1}) caused by O-H oscillation from surface absorbed water[18] becomes very pronounced.

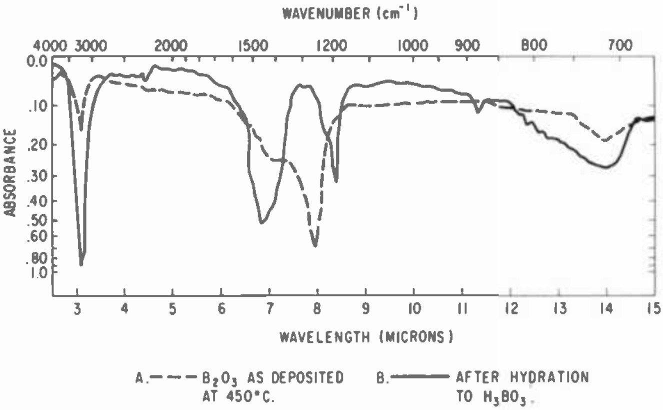

Fig. 5—Infrared absorption spectra of a vapor deposited boron oxide film before (A) and after (B) hydration to orthoboric acid.

Fig. 5 shows the spectra of a vapor-deposited B_2O_3 film taken immediately after deposition (A) and again after exposure to humidity (B). These phenomena are noted because undensified vapor-deposited glass films containing excessively high (greater than about 30 mole percent) boron oxide concentrations may devitrify forming a surface layer* of hydrated boron oxide, which then gives rise to the infrared bands described.

Pure SiO_2 deposited from silane and oxygen (Fig. 6, curve A) exhibits a major band in the region of 9.2 to 9.4 μm (1087 to 1064 cm^{-1}),[12] which is due to the Si-O stretching vibration observed in all types of viterous SiO_2.[19] The exact position of the maximum is sensitive to film thickness and particularly to structure and, hence, depends upon the degree of densification.[12] A second, much weaker, stretching vibration band occurs at 12.5 μm (800 cm^{-1}). Undensified films always show a small band in the region of 2.7 μm (3704 cm^{-1}) caused by O-H stretching due to absorbed moisture.

A film laminate consisting of a 0.3 μm layer of B_2O_3 deposited on a silicon substrate wafer and a top layer of 0.7 μm SiO_2 showed the

---

* This layer can be readily removed by rinsing with methyl alcohol without further changing the original glass layer.

following results. When measured against a 0.7 μm codeposited film (Fig. 6, curve A) in the reference beam, the difference spectrum revealed the expected spectrum for vitreous B_2O_3 (Fig. 6, curve B). Measured against a silicon blank in the reference beam, a composite spectrum resulted, as expected, consisting of the sum of the absorbances of the individual spectra (Fig. 6, curve C). The appearance of this

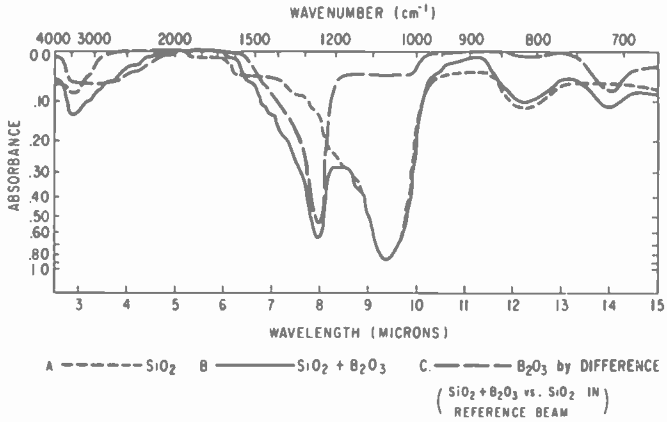

Fig. 6—Infrared absorption spectra of vapor deposited SiO_2 (curve A), $B_2O_3 + SiO_2$ (curve B), and B_2O_3 by difference measurement (curve C).

spectrum is quite different from the spectrum of a glass of comparable composition deposited by simultaneous oxidation of a silane–diborane mixture (Fig. 1). The most obvious difference is the absence of the B-O-Si absorption peak at 10.9 μm (917 cm^{-1}) and occurrence of the B-O absorption maximum at 7.94 μm (1259 cm^{-1}) instead of at the typical position 7.3 μm (1370 cm^{-1}). Heating of the laminate in argon for 15 minutes at 770°C produced a spectrum intermediate between additive and mixed component spectra, indicating that partial formation of borosilicate had taken place at the B_2O_3-SiO_2 film interface. Inspection of the B_2O_3-SiO_2 phase diagram[20] shows that, at this reaction temperature, the B_2O_3 phase can be expected to dissolve a substantial fraction of SiO_2.

These experiments clearly demonstrate that, even at the low temperatures tested (280-480°C), co-oxidation of nitrogen-diluted silane and diborane with oxygen results, under proper conditions,[1] in a real borosilicate glass, not merely in a mixture of B_2O_3 and SiO_2. In other words, there is some chemical interaction between the boron oxide and the silicon dioxide networks. The spectra also show that the various absorption bands utilized in the analysis are not seriously interfering with each other, especially since the net peak height ratios are determined. Some interference of the Si-O major peak with the B-O peak is manifest by the apparent shift of the B-O maximum towards longer wavelengths as increasing boron concentrations move the B-O peak closer to the Si-O band, but this interference does not affect the net absorbance ratio. It should also be noted that the absorption maxima of the B-O and the Si-O peaks shift slightly toward shorter wavelengths as the glass thickness increases.

5. Effect of Heat Treatments

Densifying heat treatments of vapor-deposited glass films at typically 800°C in nitrogen, oxygen, argon, or air for 10 to 15 minutes are desirable in practical applications where stable film structures with low structural stresses must be attained.[2] The effects of such heat treatments on the infrared spectrum and the absorbance ratios of borosilicates should therefore be briefly discussed also.

One of the most apparent effects in the infrared spectrum of heated samples is the increase in the absorption maximum of the Si-O major band at 9.3 μm and its shift toward shorter wavelengths. The absorbance of the main B-O band at 7.3 μm remains unchanged, indicating that no loss of B_2O_3 occurs during heating at temperatures of typically 800°C. This is true regardless of the presence or absence of an SiO_2 top layer. Therefore, the absorbance ratio [B-O]/[Si-O] is lower than before the heat treatment and decreases with increasing boron concentrations, but the general shape of the ratio versus composition curve remains the same, as seen from the dotted line in Fig. 2.

The B-O-Si and minor Si-O bands both show an increase in the height of the net absorbance peak on heat treatment, mainly due to a decrease in the base line of the peaks. Also, a narrowing of the bands occurs, which appears to sharpen the resolution. The increase is substantially greater for the Si-O band at 12.5 μm, which results in a lowering of the ratio value after heat treatment. The peaks of the absorption maxima both shift toward shorter wavelengths (larger wavenumbers) on heating. Typically, the B-O-Si peak at 10.9 μm gains 4 to 6 cm^{-1}, and the Si-O peak at 12.5 μm gains 11 cm^{-1}. These changes are shown in the spectra of Fig. 7 depicting a borosilicate glass film of about 5 μm thickness before and after densification at 800°C.

6. Stability of Vapor Deposited Borosilicate Glasses

We pointed out in a previous paper[2] that over long periods of time vapor deposited borosilicate films are stable only if they are densified sufficiently by a heat treatment. This conclusion had been reached primarily from an analysis of dielectric properties of the films; it can now be confirmed by infrared spectroscopic data.

Borosilicate layers containing 16-19 mole percent B_2O_3 were deposited on silicon wafers at 450°C by standard techniques.[1] A low and a high deposition rate were tested: 0.132 and 0.333 μm/min. The glass thickness was 1.0 μm. Top layers of 0, 0.01 and 0.03 μm SiO_2, respectively, were deposited over the glass to examine stabilizing effects on the borosilicate composition. A duplicate of each sample was densified by a heat treatment in air at 800°C for 10 minutes. Infrared spectroscopy was then carried out starting immediately after deposition and at intervals extending over a period of 3.6 years; the samples were stored in Petri dishes open to (humid) laboratory room air at approximately 23°C. A condensed summary of the results is presented in Tables 1 and 2. It can be seen that densified borosilicate films deposited at low or high rates exhibit satisfactory stability, in contrast to undensified films without SiO_2 top-layer protection.

Thicker films ($\geqslant$2.5 μm) of undensified glass have shown better stability than thinner layers, particularly if stored in a dry atmosphere. For example, the spectra shown in Fig. 7 were taken after storing the samples for 4 years in dry air.

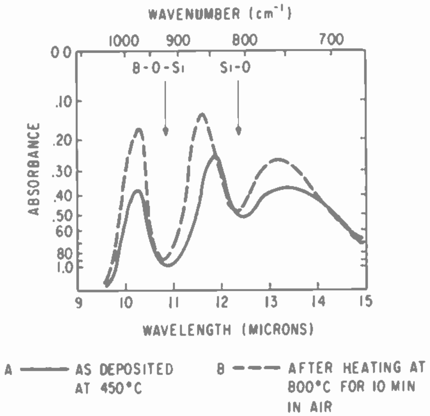

Fig. 7—Spectral shifts of the B-O-Si band and the minor Si-O band on heat treatment of a ~5 μm thick borosilicate layer.

Table 1—Testing of Borosilicate Glass Films by Infrared Spectroscopy: Stability of Films Vapor Deposited at *High Rate* as Functions of SiO_2 Top Layer and Densification

Treatment	Time From Deposition	No SiO_2 Top Layer						With SiO_2 Top Layer					
		As Deposited, 450°C			Densified, 800°C			As Deposited, 450°C			Densified, 800°C		
		B-O	Si-O	B-O/ Si-O	B-O	Si-O	B-O/ Si-O	B-O	Si-O	B-O/ Si-O	B-O	Si-O	B-O/ Si-O
None	None	1.00	1.00	1.00	1.00	1.00	1.00	1.00	1.00	1.00	1.00	1.00	1.00
Storage in Air	90 min	0.96	1.04	0.93	—	—	—	—	—	—	—	—	—
”	24 hours	0.92	1.04	0.89	0.98	1.04	0.88	0.96	1.01	0.95	0.99	0.98	1.01
”	48 hours	0.97	1.10	0.88	0.99	1.09	0.91	1.01	1.03	0.99	0.99	1.00	0.98
”	5 days	0.94	1.12	0.84	0.98	1.08	0.91	1.02	1.06	0.97	1.01	1.00	1.00
10 min Boiling	2 months	—	—	—	—	—	—	—	—	—	1.00	1.00	0.99
”	2 months	—	—	—	—	—	—	—	—	—	1.00	1.00	0.99
Storage in Air	11 months	0.61	1.30	0.47	0.96	1.05	0.91	0.91	1.19	0.76	0.97	1.00	1.00
”	3.6 years	0.48	1.46	0.33	0.95	1.08	0.88	0.88	1.28	0.69	1.05	1.04	1.01

Values Listed: Normalized net absorbance
Deposition Rate: 0.132 μm/min
Film Thickness: 1.0 μm with or without 0.01 μm SiO_2
Densification: 10 min 800°C in air
Storage Conditions: Room air at ~23°C, high relative humidity
Boiling Test: Distilled water at 100°C. Only one densified sample was tested.

Table 2—Testing of Borosilicate Glass Films by Infrared Spectroscopy: Stability of Films Vapor Deposited at *Low Rate* as Functions of SiO_2 Top Layer and Densification

Treatment	Time From Deposition	No SiO_2 Top Layer						With SiO_2 Top Layer					
		As Deposited, 450°C			Densified, 800°C			As Deposited, 450°C			Densified, 800°C		
		B-O	Si-O	B-O/ Si-O	B-O	Si-O	B-O/ Si-O	B-O	Si-O	B-O/ Si-O	B-O	Si-O	B-O/ Si-O
None	None	1.00	1.00	1.00	1.00	1.00	1.00	1.00	1.00	1.00	1.00	1.00	1.00
Storage in Air	24 hours	0.93	1.00	0.93	1.03	0.99	1.04	0.95	0.95	0.99	0.97	1.05	0.94
”	48 hours	0.90	1.00	0.90	0.99	0.97	1.00	0.97	0.98	0.98	1.01	0.94	1.07
”	5 days	0.89	1.03	0.86	1.01	1.03	0.98	0.95	1.05	0.90	1.03	0.97	1.03
”	2 months	—	—	—	1.03	1.03	1.00	—	—	—	—	—	—
10 min Boiling	2 months	—	—	—	1.03	1.03	1.00	—	—	—	—	—	—
3 hours Boiling	2 months	—	—	—	0.96	0.95	1.01	—	—	—	—	—	—
Storage in Air	11 months	0.59	1.13	0.51	—	—	—	0.89	1.15	0.76	0.95	1.02	0.91
”	3.6 years	0.34	1.45	0.24	—	—	—	0.89	1.20	0.75	0.98	1.05	0.91

Values Listed:	Normalized net absorbance
Deposition Rate:	0.333 μm/min
Film Thickness:	1.0 μm with or without 0.09 μm SiO_2
Densification:	10 min 800°C in air
Storage Conditions:	Room air at ~23°C, high relative humidity
Boiling Test:	Distilled water at 100°C. Only one densified sample was tested.

Also included in the tables are results that indicate the remarkable resistance of densified films to boiling distilled water, a particularly severe stability test for glass films.[2,21]

Conclusions

The preferred technique of infrared analysis is based on determining the ratio [B-O]/[Si-O] of the absorbance maxima of the main vibrational bands in the 7 and 9 μm-range and reading the glass composition from a calibration curve of absorbance ratio versus B_2O_3 contents. Systematic errors are canceled out, and the exact thickness of the film need not be determined. A glass film thickness up to 1.2 μm can be analyzed by this technique with good accuracy and precision.

Samples of 1 to 2.5 μm film thickness can be measured by attenuating the reference beam, which effectively expands the recorder scale such that the absorption maxima come within readability range.

Thicker layers up to about 7 μm can be evaluated by utilizing the Si-O-B peak near 11 μm and the Si-O peak at 12.5 μm. The ratio of the net absorbance of these peaks can be related to the boron concentration as in the preceding technique, but the ratio is influenced critically by the presence of SiO_2 layers, in contrast to the ratio of the major peaks. The effect is believed to be caused by interface reflectivity losses.

Calibration curves in terms of the composition of the hydride mixture used for depositing borosilicate glass films are very useful, but should be prepared for a given set of deposition conditions.

Applications of the method have been described for several investigations leading to the following conclusions:

(1) The borosilicate glass composition has been shown to be dependent on the geometry and temperature of the reactor due to the thermodynamics of the mixed hydride oxidation.

(2) Oxidation of a nitrogen diluted silane–diborane mixture in the temperature range of 280 to 480°C has been demonstrated to yield a borosilicate glass, not merely a physical mixture of B_2O_3 plus SiO_2.

(3) Densification of high-boron glasses can lead to surface layers of B_2O_3 that may hydrate to H_3BO_3 when exposed to moisture; these layers show characteristic infrared absorption bands.

(4) Heat treatment of borosilicate glass films at typically 800°C increases the absorption intensity of the Si-O bands and the Bi-O-Si band, but not that of the B-O band. Characteristic shifts in the wavelength positions of the absorption maxima occur on densification of the structure.

(5) Undensified and densified borosilicate glass films of 1 μm thickness containing 16 to 19 mol % B_2O_3, with and without thin SiO_2 top layers, were measured over a storage period of 3.6 years in room air of high relative humidity. The densified films with a thin SiO_2 top layer remained essentially stable over this time period, regardless of the rate of film deposition tested. Exposure to boiling distilled water did not change the composition of these films. As previously noted,[2] undensified borosilicate films are unstable on prolonged storage. The spectra of undensified films show a decrease of the B-O band, which an SiO_2 top layer can greatly reduce. The absorbance maximum of the major Si-O band of these films increases in magnitude with storage time, similar to what occurs during a high-temperature heat treatment within minutes. Thicker films of undensified layers, particularly if stored dry, have shown much better stability on storage.

Acknowledgments

The author wishes to thank Michael D. Sutherlin and Walter J. Miller for preparing vapor-deposited glass films; Charles J. Jacobs and Bernard L. Goydish for chemical analysis; Peter J. Zanzucchi for many helpful comments and discussions; and G. L. Schnable for critically reviewing this paper.

References:

[1] W. Kern and R. C. Heim, "Chemical Vapor Deposition of Silicate Glasses for Use with Silicon Devices—I. Deposition Techniques," **J. Electrochem. Soc.**, Vol. 117, p. 562 (1970).

[2] W. Kern and R. C. Heim, "Chemical Vapor Deposition of Silicate Glasses for Use with Silicon Devices; Part II—Film Properties," **J. Electrochem. Soc.**, Vol. 117, p. 568 (1970).

[3] W. Kern and A. W. Fisher, "Deposition and Properties of Silicon Dioxide and Silicate Films Prepared by Low-Temperature Oxidation of Hydrides," **RCA Rev.**, Vol. 31, p. 715 (1970).

[4] J. A. Amick and W. Kern, "Chemical Vapor Deposition Techniques for the Fabrication of Semiconductor Devices," p. 551, in **Chemical Vapor Deposition**, Second Internat'l. Conf., J. M. Blocher, Jr. and J. C. Withers, Editors, The Electrochem. Soc., Inc., New York, 1970.

[5] D M. Brown and P. R. Kennicott, "Glass Source B Diffusion in Si and SiO_2," **J. Electrochem. Soc.**, Vol. 118, p. 293 (1971).

[6] G. L. Schnable, "Glass Passivation of Integrated Circuits by Chemical Vapor Deposition of Oxide Films," IEEE International Convention 1971, New York, Paper 6CJ2.

[7] W. Kern, "Densification of Chemically Vapor Deposited Borosilicate Glasses," **J. Electrochem. Soc.**, Vol. 116, p. 251C (1969). (Abstract).

[8] W. Kern, "A Technique for Measuring Etch Rates of Dielectric Films," **RCA Rev.**, Vol. 29, p. 557 (1968).

[9] W. Kern, "Apparatus for Chemical Vapor Deposition of Oxide and Glass Films," **RCA Rev.**, Vol. 29, p. 525 (1968).

[10] B. L. Goydish, "The Quantitative Determination of Boron in Glasses Used as Encapsulants for Electric Devices," **Microchem. J.**, Vol. 15, p. 572 (1970).

[11] W. T. Potts, Jr., **Chemical Infrared Spectroscopy**, Vol. I—Techniques, John Wiley & Sons, Inc., New York, 1963.

[12] N. Goldsmith and W. Kern, "The Deposition of Vitreous Silicon Dioxide Films from Silane," **RCA Rev.**, Vol. 29, p. 525 (1968).

[13] A. L. Smith, "Infrared Spectroscopy," Chapter 66 in **Treatise On Analytical Chemistry,** I. M. Kolthoff and P. J. Elving, Eds., Vol. 6, Part I, Interscience Publishers, New York, 1965.

[14] K. Strater and A. Mayer, "The Oxidation of Silane, Phosphine, and Diborane during Deposition of Doped-Oxide Diffusion Sources," p. 469 in **Semiconductor Silicon,** R. R. Haberecht and E. L. Kern, Ed., The Electrochem. Soc., Inc., New York 1969.

[15] P. P. Webb, RCA Limited, Montreal, Canada; Private Communication.

[16] J. L. Parsons and M. E. Milberg, "Vibrational Spectra of Vitreous $B_2O_3 . x H_2O$," **J. Am. Ceram. Soc.,** Vol. 43, p. 326 (1960).

[17] N. F. Borelli and G. J. Su, "An Interpretation of the Infra-Red Spectra of Vitreous Boron Oxide," **J. Phys. and Chem. of Glasses,** Vol. 4, p. 206 (1963).

[18] R. V. Adams, "Infrared Absorption Due to Water in Glasses," **J. Phys. and Chem. of Glasses,** Vol. 2, p. 39 (1969).

[19] W. A. Pliskin, "The Evaluation of Thick Film Insulators," **Thin Solid Films,** Vol. 2, p. 1 (1968).

[20] T. J. Rockett and W. R. Foster, "Phase Relations in the System Boron Oxide-Silica," **J. Am. Ceram. Soc.,** Vol. 48, p. 78 (1965).

[21] W. A. Pliskin, "The Stability of Glazed Silicon Surfaces to Water Attack," **Proc. IEEE,** Vol. 52, p. 1468 (1964).

Numerical Differentiation Formulas For Stiff Systems of Ordinary Differential Equations

R. W. Klopfenstein
RCA Laboratories, Princeton, N.J.

Abstract—Numerical differentiation (N.D.) formulas of orders one through six provide effective means for the numerical solution of stiff systems of ordinary differential equations in that they are stable in a symmetric wedge including the negative real half-line. A generalization of previously used N.D. formulas increases the angular width of the wedge of stability at only modest cost in increased local truncation error. The asymptotic (large *h*) sensitivity of the formulas to the accuracy of the Jacobian matrix is not increased by this generalization. These formulas are useful, for example, in the determination of the response of large scale integrated circuits.

1. Introduction

The practice of numerical differentiation has traditionally been an anathema for practicing numerical analysts. This has been primarily due to the great sensitivity to small uncertainties in the data for algorithms based on polynomial approximation.

Recent work on the numerical solution of stiff systems of differential equations has done much to restore the respectability of numerical differentiation, at least within that context. Indeed, such algorithms turn out to have some unique advantages over other possible multistep formulas.

A formula that produces an approximation to the derivative of a given function at a given point through a linear combination of values of the function will be referred to as a numerical differentiation (N.D.) formula. Thus, the formula

$$hf(x_{n+1-r}, y_{n+1-r}) = \sum_{m=0}^{k} a_m y_{n+1-m}, \qquad [1.1]$$

where

$$y' = \frac{dy}{dx} = f(x,y),$$

is an example of such a formula suitable for the construction of approximate solutions to ordinary differential equations. It represents a linear multistep method (Ref. [4], p. 209) and when $r = 0$ it is an implicit formula in that y_{n+1} appears on both sides of Eq. [1.1] and is not given explicitly by the formula.

The most common form of Eq. [1.1] is given by

$$hf(x_{n+1}, y_{n+1}) = \sum_{m=1}^{k} \frac{1}{m} \nabla^m y_{n+1}, \qquad [1.2]$$

where $\nabla^m y_{n+1}$ denotes the mth order backward difference of the y values based at y_{n+1}. This is a linear k-step method of order k. The properties of Eq. [1.2] are discussed in considerable detail by Henrici (Ref. [4], pp. 206-209). Among the first to recognize the efficacy of formulas of the type [1.2] for stiff differential equations were Curtiss and Hirschfelder[1] in 1952. They explicitly exhibit versions through the fourth order ($k = 4$). More recently Gear[3] and Krogh[6] have recognized their applicability for systems of stiff differential equations and have reported considerable success in their exploitation toward that end.

In this paper I report the results of studies of a generalization of Eq. [1.2] that makes use of data generally present. This generalization results in improved stability characteristics at little cost in computational effort. The asymptotic (large h) stability characteristics of Eq. [1.2] as well as its generalization are studied in a subsequent section. These asymptotic stability characteristics provide guidelines for the exploitation of such formulas in applications.

2. Stability Diagrams and Optimization of Stable Regions

One particularly effective implementation[6] of Eq. [1.2] makes use of an extrapolative predictor formula,

$$p_{n+1} = \sum_{m=0}^{k} \nabla^m y_n, \qquad [2.1]$$

to obtain a first estimate for y_{n+1}. It is generally desirable that Eq. [2.1] have the same order of approximation (k) as Eq. [1.2]. Thus, Eq. [2.1] involves one more back point than does Eq. [1.2]. It is natural to inquire whether this additional datum would be of use in generalizing Eq. [1.2] to further improve its many desirable properties.

To that end, the following N.D. formula is considered:

$$hf(x_{n+1}, y_{n+1}) = \sum_{m=1}^{k} \frac{1}{m} \nabla^m y_{n+1} - \alpha\gamma_k (y_{n+1} - p_{n+1}), \qquad [2.2]$$

where

$$\gamma_k = \sum_{m=1}^{k} \frac{1}{m}.$$

In this form it is evident that Eq. [2.2] is of the same order as Eqs. [1.2] and [2.1]. Eq. [2.2] thus constitutes a one parameter family of kth order implicit N.D. formulas, and that parameter may be chosen to emphasize one or another desirable property of the algorithm. Through Taylor series expansions it is found that the error constant (Ref. [4], pp. 223, 238, 251) associated with Eq. [2.2] is given by

$$C = \alpha\gamma_k + \frac{1}{k+1}. \qquad [2.3]$$

In order to determine the stability properties of Eq. [2.2], I apply it to the single equation, $y' = \eta y$, and determine the values of ηh for which solutions of the resulting difference equation would tend to zero. The characteristic equation of this resulting difference equation is given by

$$\eta h = q = \sum_{m=1}^{k} \frac{1}{m} \xi^m - \alpha\gamma_k \xi^{k+1},$$

$$\xi = 1 - \lambda^{-1} = 1 - e^{-i\varphi}, \qquad [2.4]$$
$$-\pi \leqslant \varphi \leqslant \pi.$$

The region, S_q, of absolute stability in the q-plane is the complement of the map of the exterior of the unit circle in the λ-plane. Thus, the point at infinity is always included in the region S_q for the family of N.D. formulas of Eq. [2.2]. If the region, S_q, contains as a subset the entire left-half plane, the corresponding algorithm is termed A-stable.[2]

Dahlquist[2] has shown that in order for a multistep formula to be A-stable it must be (1) implicit and (2) have an order equal to or less than two; and further, that among all second order formulas that are A-stable the trapezoidal rule has the smallest error constant. Therefore, I will first study second order algorithms from the family of Eq. [2.2] seeking to minimize the error constant of Eq. [2.3] while retaining A-stability. Under the substitution indicated in Eq. [2.4] it is found that for $k = 2$

$$\operatorname{Re}(q) = 4\sin^4\theta[1 - 3\alpha + 12\alpha\cos^2\theta], \qquad \theta = \frac{\varphi}{2}, \tag{2.5}$$

where $\operatorname{Re}(q)$ denotes the real part of q.

Eq. [2.2] will be A-stable so long as $\operatorname{Re}(q)$ is non-negative for all values of φ. From Eq. [2.5] it is seen that this will be the case if and only if $-1/9 \leqslant \alpha \leqslant 1/3$. Since the error constant of Eq. [2.3] is a monotone function of α, the following theorem has been established:

Theorem 1. A-stable N.D. formulas of the family of Eq. [2.2] have orders equal to or less than two.[2] Among those of second order, that one corresponding to $\alpha = -1/9$ has the smallest error constant equal to $2C_T$, where C_T is the error constant of the trapezoidal rule.

The boundary of the stable region for second order algorithms is exhibited in Fig. 1 for three different values of α. The smallest value shown, $\alpha = -2/9$, corresponds also to $\alpha = 0$ for $k = 3$.

For N.D. formulas of orders greater than two, there is, of course, no hope of obtaining A-stability. I will obtain $A(\alpha)$ stability in the sense of Widlund[7] for orders equal to or less than six[6] and seek to maximize the width of the wedge shaped region so obtained by an appropriate selection of the parameter α.

A numerical procedure was used to obtain the value of α for orders three through six of the N.D. formulas of Eq. [2.2] which maximized the angular width of the wedge. The results for the sixth order case are

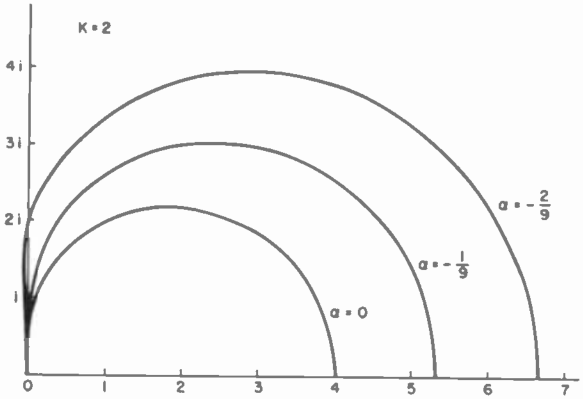

Fig. 1—Boundaries of stable regions for numerical differentiation formulas.

exhibited in Fig. 2. It is seen that in this case, the angular width of the wedge has been almost doubled.

Table 1 summarizes the results of this section and indicates, in greater detail than the graphs of Figs. 1 and 2, the tradeoffs to be expected.

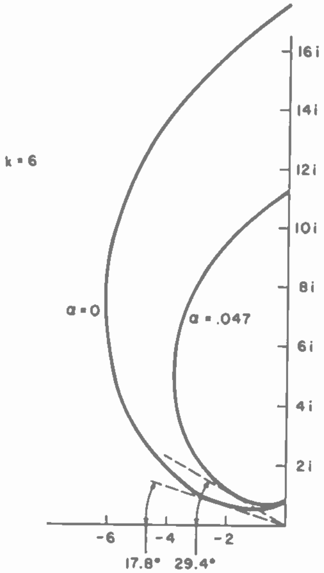

Fig. 2—Boundaries of stable regions for numerical differentiation formulas.

Table 1—Optimum N.D. Formulas

Computing Time Percent Increase (Decrease) for Given Max. Error	k	a	Max ($\cot\varphi$)	Min φ	Error Constant
	6	0	3.10722	17.84°	$C_0 = \frac{1}{7}$
+ 10.2%	6	.0464	1.77469	29.40°	1.7958 C_0
	5	0	.785799	51.84°	$C_0 = \frac{1}{6}$
+ 11.9%	5	.0551	.626691	57.92°	1.7549 C_0
	4	0	.299032	73.35°	$C_0 = \frac{1}{5}$
+ 14.1%	4	.0665	.248316	76.05°	1.6927 C_0
	3	0	.0693592	86.03°	$C_0 = \frac{1}{4}$
+ 17.2%	3	.0834	.0579483	86.68°	1.6116 C_0
	2	0	0.	90°	$C_0 = \frac{1}{3}$
− 29.3%	2	$-\frac{1}{9}$	0.	90°	0.5 C_0

Note: φ is the half-angle of the wedge of absolute stability.

3. Asymptotic Stability of P(EC)^m Algorithms Based on N.D. Formulas

While the analysis of the preceding section was based on implicit formulas of the form of Eq. [2.2], all algorithms for the numerical solution of ordinary differential equations are, in fact, explicit. The initial value problem

$$\mathbf{y}' = \frac{d\mathbf{y}}{dx} = \mathbf{f}(x,\mathbf{y}), \qquad \mathbf{y}_0 = \mathbf{y}(0), \tag{3.1}$$

is given and an algorithm constructs a discrete set

$$S = \{\mathbf{y}_n\}_{n=0}{}^{N}, \tag{3.2}$$

such that the $\mathbf{y}_n$ so obtained approximate the exact solution of Eq. [3.1], $\mathbf{y}(x_n)$, on some discrete mesh of points, x_n, with exact correspondence only at the point x_0. In progressing from the nth to the $(n+1)$st point, the information available is some fixed number, say $k+1$, of previous members of the sequence S and the derivative relationship of Eq. [3.1]. For the purposes of analysis, the set of points, x_n, are generally assumed uniformly spaced at an increment (step size) h though a practical algorithm must contain means for changing this step size as well as starting the solution. A constant step size is assumed in the work of this section.

To summarize, I consider the system of ordinary differential equations of Eq. [3.1] and a $(k+1)$-step algorithm

$$\mathbf{y}_{n+1} = \mathbf{F}(h,\tilde{J},\mathbf{y}_n,\cdots,\mathbf{y}_{n-k}), \qquad [3.3]$$

which generates the sequence of Eq. [3.2] of approximate solution values to Eq. [3.1] with h a real positive scaler. $\tilde{J}$ is a matrix which approximates the matrix J of the linear system of ordinary differential equations

$$\mathbf{y}' = J\mathbf{y} + \mathbf{c}, \qquad [3.4]$$

with $\mathbf{c}$ a constant vector, and J a constant matrix of order N with eigenvalues properly in the left-half complex plane. The difference between approximate and exact Jacobian matrices is denoted by the matrix

$$\Delta = J - \tilde{J}. \qquad [3.5]$$

Definition 1

The algorithm of Eq. [3.3] is said to be asymptotically $(h \to \infty)$ absolutely stable in solving the system of Eq. [3.4] if the sequence $\{\mathbf{y}_n\}_{n=0}^{\infty}$ is uniformly bounded in norm for all sufficiently large $h \geqslant h_0 > 0$ when the eigenvalues of

$$J^{-1}\Delta = I - J^{-1}\tilde{J},$$

lie within a region R containing a circle of radius $c > 0$ centered on the origin where c is independent of h.

Definition 2

The region R of Definition 1 is called the "region of asymptotic absolute stability" for the algorithm of Eq. [3.3].

The concepts and definitions introduced here are similar to those introduced at the beginning of Section II of Ref. [5]. The definition of asymptotic absolute stability given here, however, is more restrictive than that given in Ref. [5] and would not be met by the algorithms discussed there. The more favorable asymptotic stability characteristics of the algorithms discussed here is due to the numerical differentiation (N.D.) form of Eq. [2.2].

I now define a class of explicit $P(EC)^m$ algorithms that make use of the predictor of Eq. [2.1] followed by m applications of the Newton–Raphson method to the N.D. corrector formula of Eq. [2.2]. The algorithm is defined explicitly by

$$
\begin{aligned}
&\mathbf{y}_{n+1}{}^{(0)} = \mathbf{p}_{n+1} = \sum_{m=0}^{k} \nabla^m \mathbf{y}_n, \\
&\mathbf{r}_l = (1-\alpha)\,(\mathbf{y}_{n+1}{}^{(l-1)} - \mathbf{p}_{n+1}) - \frac{1}{\gamma_k}\left\{h\mathbf{f}(x_{n+1},\mathbf{y}_{n+1}{}^{(l-1)}) - \sum_{m=1}^{k}\gamma_m \nabla^m \mathbf{y}_n\right\}, \\
&\mathbf{y}_{n+1}{}^{(l)} = \mathbf{y}_{n+1}{}^{(l-1)} - A^{-1}\mathbf{r}_l, \\
&l = 1, 2, \cdots, m,
\end{aligned}
\qquad [3.6]
$$

where

$$
A = (1-\alpha)\, I - \frac{h}{\gamma_k}\tilde{J}.
$$

As in Ref. [5], it suffices to apply Eq. [3.6] to Eq. [3.4] with $\mathbf{c}$ set equal to zero since the sequence $\mathbf{y}_n$ obtained for non-zero $\mathbf{c}$ will be bounded in norm if and only if the sequence obtained for $\mathbf{c} = 0$ is. When this is done, the algorithm of Eq. [3.6] takes the form

$$
\begin{aligned}
&\mathbf{y}_{n+1}{}^{(0)} = \mathbf{p}_{n+1} = \sum_{m=0}^{k} \nabla^m \mathbf{y}_n, \\
&\mathbf{r}_l = (A - \frac{h}{\gamma_k}\Delta)\,(\mathbf{y}_{n+1}{}^{(l-1)} - \mathbf{p}_{n+1}) - \frac{h}{\gamma_k}\left\{hJ\mathbf{p}_{n+1} - \sum_{m=1}^{k}\gamma_m \nabla^m \mathbf{y}_n\right\}, \\
&\quad = (A - \frac{h}{\gamma_k}\Delta)\,(\mathbf{y}_{n+1}{}^{(l-1)} - \mathbf{p}_{n+1}) + \mathbf{r}_1
\end{aligned}
\qquad [3.7]
$$

$$\mathbf{y}_{n+1}{}^{(l)} = \mathbf{y}_{n+1}{}^{(l-1)} - A^{-1}\mathbf{r}_l,$$
$$l = 1, 2, \cdots, m.$$

After a certain amount of algebraic manipulation, Eq. [3.7] leads to

$$A\mathbf{y}_{n+1}{}^{(l)} = \frac{h}{\gamma_k}\Delta\,(\mathbf{y}_{n+1}{}^{(l-1)} - \mathbf{p}_{n+1}) + A\mathbf{y}_{n+1}{}^{(1)},$$

with [3.8]

$$A\mathbf{y}_{n+1}{}^{(1)} = (1-\alpha)\mathbf{p}_{n+1} + \frac{h}{\gamma_k}\Delta\mathbf{p}_{n+1} - \frac{1}{\gamma_k}\sum_{m=1}^{k}\gamma_m\nabla^m\mathbf{y}_n,$$

which exhibits the immediate convergence of $P(EC)^m$ algorithms when $\Delta = 0$, i.e., when $\tilde{J} = J$.

Lemma 1. The $\mathbf{y}_{n+1}{}^{(l)}$ satisfying Eq. [3.8] can be expressed by

$$\mathbf{y}_{n+1}{}^{(l)} = \sum_{r=0}^{l-1}\left(\frac{h}{\gamma_k}A^{-1}\Delta\right)^r(\mathbf{y}_{n+1}{}^{(1)} - \mathbf{p}_{n+1}) + \mathbf{p}_{n+1}, \qquad [3.9]$$

for $l = 1, 2, \cdots, m$.

Proof: The proposition holds identically for $l = 1$. Assume that it holds for $l = k$. Then, by Eq. [3.8],

$$\begin{aligned}\mathbf{y}_{n+1}{}^{(k+1)} &= \frac{h}{\gamma_k}A^{-1}\Delta\left[\left\{\sum_{r=0}^{k-1}\left(\frac{h}{\gamma_k}A^{-1}\Delta\right)^r(\mathbf{y}_{n+1}{}^{(1)} - \mathbf{p}_{n+1})\right.\right.\\ &\qquad\left.\left. + \mathbf{p}_{n+1}\right\} - \mathbf{p}_{n+1}\right] + \mathbf{y}_{n+1}{}^{(1)},\\ &= \sum_{r=0}^{k-1}\left(\frac{h}{\gamma_k}A^{-1}\Delta\right)^{r+1}(\mathbf{y}_{n+1}{}^{(1)} - \mathbf{p}_{n+1}) + \mathbf{y}_{n+1}{}^{(1)} - \mathbf{p}_{n+1} + \mathbf{p}_{n+1},\\ &= \sum_{r=0}^{k}\left(\frac{h}{\gamma_k}A^{-1}\Delta\right)^{r}(\mathbf{y}_{n+1}{}^{(1)} - \mathbf{p}_{n+1}) + \mathbf{p}_{n+1}.\end{aligned}$$

Hence, the result follows by induction.

In particular, as a consequence of Lemma 1,

$$\mathbf{y}_{n+1}{}^{(m)} = \sum_{r=0}^{m-1} \left(\frac{h}{\gamma_k} A^{-1}\Delta \right)^r (\mathbf{y}_{n+1}{}^{(1)} - \mathbf{p}_{n+1}) + \mathbf{p}_{n+1}. \qquad [3.10]$$

Now, from Eq. [3.8],

$$A(\mathbf{y}_{n+1}{}^{(1)} - \mathbf{p}_{n+1}) = \frac{1}{\gamma_k} \left\{ hJ\mathbf{p}_{n+1} - \sum_{m=1}^{k} \gamma_m \nabla^m \mathbf{y}_n \right\}. \qquad [3.11]$$

so that

$$\gamma_k A \mathbf{y}_{n+1}{}^{(m)} = \sum_{r=0}^{m-1} \left(\frac{h}{\gamma_k} \Delta A^{-1} \right)^r \left(hJ\mathbf{p}_{n+1} - \sum_{m=1}^{k} \gamma_m \nabla^m \mathbf{y}_n \right) + \gamma_k A \mathbf{p}_{n+1}. \qquad [3.12]$$

Now attention will be restricted to matrices J which can be fully diagonalized by a similarity transormation, and the definitions

$$\begin{aligned} Q &= hPJP^{-1}, \\ D &= hP\Delta P^{-1}, \\ \mathbf{z}_{n+1} &= P\mathbf{y}_{n+1}{}^{(m)}, \\ \mathbf{r}_{n+1} &= P\mathbf{p}_{n+1}, \\ B &= PAP^{-1} = (1-\alpha)I - \frac{1}{\gamma_k}(Q-D), \end{aligned} \qquad [3.13]$$

are introduced where Q is a diagonal matrix whose elements lie entirely in the left half plane.

When these are applied to Eq. [3.12], one obtains

$$\gamma_k B \mathbf{z}_{n+1} = \sum_{r=0}^{m-1} \left(\frac{1}{\gamma_k} DB^{-1} \right)^r \left(Q\mathbf{r}_{n+1} - \sum_{m=1}^{k} \gamma_m \nabla^m \mathbf{z}_n \right) + \gamma_k B \mathbf{r}_{n+1}. \qquad [3.14]$$

When $h \to \infty$,

$$B \sim -\frac{1}{\gamma_k}(Q\text{-}D),$$

$$B^{-1} \sim -\gamma_k (Q\text{-}D)^{-1},$$

and the asymptotic form of Eq. [3.14] is

$$\begin{aligned}\mathbf{z}_{n+1} &\sim \left\{ I - (Q\text{-}D)^{-1} \sum_{r=0}^{m-1} [-(Q\text{-}D)^{-1}]^r Q \right\} \mathbf{r}_{n+1}, \\ &\sim A_m \mathbf{r}_{n+1}.\end{aligned} \qquad [3.15]$$

Lemma 2. The matrix A_m defined in Eq. [3.15] is expressible as

$$A_m = (-1)^m [(Q\text{-}D)^{-1} D]^m. \qquad [3.16]$$

Proof: By direct substitution Eq. [3.16] holds for $m = 1$. Assume that it holds for $m = l$. Then

$$\begin{aligned} A_{l+1} &= A_l - (Q\text{-}D)^{-1} [-D(Q\text{-}D)^{-1}]^l Q, \\ &= [-(Q\text{-}D)^{-1} D]^l - (Q\text{-}D)^{-1} [-D(Q\text{-}D)^{-1}]^l Q, \\ &= [-(Q\text{-}D)^{-1} D]^l - [-(Q\text{-}D)^{-1} D]^l (Q\text{-}D)^{-1} Q, \\ &= [-(Q\text{-}D)^{-1} D]^l \{ I - (Q\text{-}D)^{-1} Q \}, \\ &= [-(Q\text{-}D)^{-1} D]^l (Q\text{-}D)^{-1} \{ Q\text{-}D\text{-}Q \}, \\ &= [-(Q\text{-}D)^{-1} D]^{l+1}. \end{aligned}$$

Lemma 2 follows by induction.

By methods similar to those used in Appendix 1 of Ref. [5], it can be shown that it is sufficient to study the asymptotic form of the difference equation of Eq. [3.15] in order to establish the asymptotic stability required by Definition 1. One, therefore, studies the stability properties of the difference equation

$$\begin{aligned} \mathbf{z}_{n+1} &= A_m \mathbf{r}_{n+1}, \\ &= A_m \sum_{r=0}^{k} \nabla^r \mathbf{z}_n, \\ &= A_m \sum_{r=0}^{k} (-1)^r \binom{k+1}{r+1} \mathbf{z}_{n-r}. \end{aligned} \qquad [3.17]$$

Again following the methods of Ref. [5], it can be shown that the stability of Eq. [3.17] is equivalent to the requirement that the eigenvalues, λ, of the matrix eigenvalue problem

$$[\lambda^{k+1} - (\lambda - 1)^{k+1}]A_m\mathbf{u} = \lambda^{k+1}\mathbf{u}, \tag{3.18}$$

be equal to or less than unity in absolute value and that eigenvalues of unit magnitude be simple.

Now consider the eigenvalue problem

$$A_1\mathbf{u} = f(\lambda)\mathbf{u}. \tag{3.19}$$

Repeated multiplication by A_1 leads to

$$A_1{}^m\mathbf{u} = A_m\mathbf{u} = f^m(\lambda)\mathbf{u}. \tag{3.20}$$

Therefore, Eq. [3.19] is equivalent to Eq. [3.18] with $f(\lambda)$ defined by

$$\begin{aligned} f^m(\lambda) &= \frac{d_k(\lambda)}{d_k(\lambda) - 1}, \\ d_k(\lambda) &= \left(\frac{\lambda}{\lambda - 1}\right)^{k+1}. \end{aligned} \tag{3.21}$$

Since $A_1 = -(Q\text{-}D)^{-1}D$, Eq. [3.19] can be written as

$$D\mathbf{u} = g(\lambda)Q\mathbf{u},$$

with [3.22]

$$g(\lambda) = \frac{f(\lambda)}{f(\lambda) - 1}.$$

The eigenvalue value problem of Eq. [3.22] furnishes the basis for studying the asymptotic region of stability of Definitions 1 and 2. The region R defined therein is the complement in the g-plane of the map of the exterior of the unit circle in the λ-plane. This mapping is defined through Eqs. [3.21] and [3.22].

Theorem 2. The $P(EC)^m$ algorithm consisting of one application of the predictor of Eq. [2.1] followed by m applications of the Newton-Raphson method to the corrector of Eq. [2.2] is asmptotically ($h \to \infty$) absolutely stable in solving the system of Eq. [3.4]. The region R of asymptotic absolute stability is the complement in the g-plane of the map of the exterior unit circle in the λ-plane. This mapping is defined through Eqs. [3.21] and [3.22].

Proof: It only remains to be shown that the region R is not empty. To do this, it is necessary to exhibit a neighborhood, N, of the origin in the g-plane such that all of the $k+1$ images in the λ-plane of every point in N fall within the unit circle.

The mapping, g, may be expressed by

$$(1-g^{-1})^m = 1-(1-\lambda^{-1})^{k+1}, \qquad [3.23]$$

which is equivalent to

$$\lambda^{k+1}(g-1)^m + g^m(\lambda-1)^{k+1} = g^m\lambda^{k+1}. \qquad [3.24]$$

From Eq. [3.24] it is evident that the origin itself is in N, as required, since the images of $g=0$ are a $(k+1)$-fold zero in the λ-plane. A straightforward application of inequalities to Eq. [3.23] shows that

$$|g| < \epsilon. \qquad [3.25]$$

implies that

$$|\lambda| < \frac{1}{\left[\left(\dfrac{1}{\epsilon}-1\right)^m - 1\right]^{1/(k+1)} - 1}, \qquad [3.26]$$

where

$$0 < \epsilon < \frac{1}{1+2^{1/m}}.$$

From this, it can be inferred that

$$|g| < \frac{1}{1+[1+2^{k+1}]^{1/m}}, \qquad [3.27]$$

is sufficient to ensure that all $k+1$ images in the λ-plane satisfy

$$|\lambda| < 1. \qquad \text{QED}$$

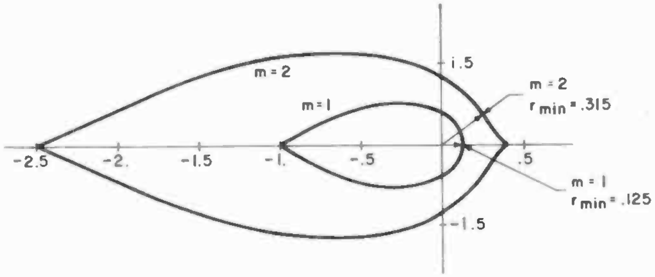

Fig. 3—Asymptotic regions of absolute stability for $P(EC)^m$ implementation of second order N.D. formulas.

It is to be noted that the parameter α which appears in Eqs. [2.2] and [3.6] does not appear in the eigenvalue problem of Eq. [3.22] defining the asymptotic region of stability. Thus, α may be selected to optimize the region, S_q, of absolute stability in the q-plane without affecting the asymptotic region of absolute stability. This is not to say, of course, that α may not influence the stability properties of Eq. [3.6] for intermediate values of h.

Figs. 3 and 4 exhibit the asymptotic regions, R, of absolute stability for one and two applications of the corrector of Eq. [2.2] for second- and fifth-order formulas, respectively. It should be noted that these are shown to different scales and the regions of Fig. 4 are actually much smaller than the corresponding regions of Fig. 3.

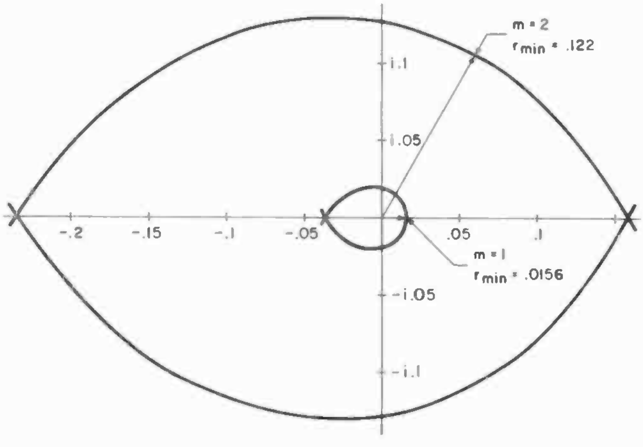

Fig. 4—Asymptotic regions of absolute stability for $P(EC)^m$ implementation of fifth order N.D. formulas.

The salient feature of these diagrams is their point of closest approach to the origin. This distance, denoted by $r_{\min}$, determines the minimum deviation of the eigenvalues of J from those of J that can lead to instability in the algorithm in the asymptotic $(h \rightarrow \infty)$ limit. It is desirable that $r_{\min}$ be as large as possible for minimum sensitivity to values of the Jacobian matrix.

Table 2—Minimum Radius of Asymptotically Stable Regions for $P(EC)^m$ Algorithms for various orders (k).

m \ k	2	3	4	5	6
1	.125	.0625	.0312	.0156	.0078
2	.315	.233	.170	.122	.0871
3	.343	.288	.241	.201	.166
4	.399	.353	.311	.273	.238
.	.	.	.	.	.
.	.	.	.	.	.
.	.	.	.	.	.
∞	.5	.5	.5	.5	.5

Table 2 exhibits the values of $r_{\min}$ for various orders, k, of the N.D. formulas of Eq. [2.2] and various (fixed) numbers, m, of its application in a $P(EC)^m$ implementation starting from the predictor of Eq. [2.1]. A number of characteristics of the resulting algorithms may be observed from this table. For a given number, m, of iterations the stable radius, $r_{\min}$, decreases monotonically with increasing order, k, but the rate of decrease is smaller for larger m being approximately in the ratio $(2m-1)/(2m)$. Furthermore, for fixed order, k, the value of $r_{\min}$ increases monotonically with m, and in each case it approaches the asymptotic $(m \rightarrow \infty)$ limit of $r_{\min} = 0.5$. The most dramatic increase in $r_{\min}$ occurs in going from $m = 1$ to $m = 2$. This suggests less justification for increasing the number of corrector applications beyond two. It should be noted that at least two derivative evaluations are required if one is to have a measure of the convergence to Eq. [2.2] in a practical algorithm.

4. Conclusions

The numerical differentiation formulas of Eq. [1.1] furnish a useful basis for constructing the numerical solution of stiff systems of ordinary differential equations when combined with the extrapolative predictor of

Eq. [2.1]. A non-zero parameter, α, may be introduced leading to the form of Eq. [2.2]. The order of the resulting algorithm is unchanged, there is no increase in storage requirements, and little increase in computing effort. The value of α may be selected to maximize the region of absolute stability, S_q, in the q-plane in the sense of Widlund[7]. Only modest increases in the error constants of the algorithm result from such selection (see Table 1).

The formula of Eq. [2.2] may be implemented in a $P(EC)^m$ manner by using the predictor of Eq. [2.1] followed by m applications of the Newton-Raphson method to Eq. [2.2]. A study of the asymptotic stability properties of these algorithms shows that such properties are not affected by the parameter α. Furthermore, there is little justification for using more than two applications of the corrector ($m = 2$) from the point of view of asymptotic absolute stability as defined here.

References:

[1] C. F. Curtiss and J. O. Hirschfelder, "Integration of Stiff Equations," **Proc. of National Academy of Science,** Vol. 38, p. 235, (1952).

[2] G. G. Dahlquist, "A Special Stability Problem for Linear Multistep Methods," **BIT,** Vol. 3, p. 27, (1963).

[3] C. W. Gear, "The Automatic Integration of Stiff Ordinary Differential Equations," **Proc. 1968 IFIPS Congress,** pp. A81-A85.

[4] P. Henrici, **Discrete Variable Methods in Ordinary Differential Equations,** John Wiley & Sons, New York, 1962.

[5] R. W. Klopfenstein and C. B. Davis, "PECE Algorithms for the Solution of Stiff Systems of Ordinary Differential Equations," **Math. of Computation,** Vol. 25, p. 457, (1971).

[6] F. T. Krogh, **The Numerical Integration of Stiff Differential Equations,** TRW Report No. 99900-6573-R000 (March 1968), Redondo Beach, California.

[7] O. B. Widlund, "A Note on Unconditionally Stable Linear Multistep Methods," **BIT,** Vol. 7, p. 65, (1967).

The Acoustoelectric Effects and the Energy Losses by Hot Electrons

Part V—Physical Concepts in Energy-Loss Processes

A. Rose, RCA Laboratories, Princeton, N. J.

Abstract—The loss of energy by an excited electron is known generally as spontaneous emission. The physical origin of this emission must logically lie in the interaction between the electron and its medium. The interaction in a solid medium, as opposed to vacuum, is easily traceable to a simple classical polarization of the medium by the emitting electron. A coupling constant is defined having the natural limits of zero and unity. It is shown that the constant can be expressed either in terms of the electrical and elastic components of the energy of the distorted medium or in terms of the real part of its dielectric constant. The structure of the imaginary part is shown to play a negligible role. The coupling constant is valid in the classical limit of acoustoelectric interactions as well as in the quantum limit of electron–phonon interactions. By detailed balance, it is also valid for induced as well as spontaneous emission. The form of the coupling constant gives an easy insight into several tangential problems; a generalized expression for the Lyddane–Sachs–Teller relation, the self-trapping of electrons, and the spontaneous deformation of a lattice.

Introduction

A major part of this series of papers* has been concerned with the rates of energy loss by fast-moving electrons in a solid medium. As the velocity of the electron is increased, the electron radiates energy first to acoustic phonons, then to optical phonons, impact ionizations, plasmons, x-ray levels, and Cerenkov radiation, in that order. The range of electron energies extends from 10^{-3} to over 10^5 electron volts.

---

* This is the concluding part of a series published in previous issues of RCA Review as follows: Part I, "Small Signal Acoustoelectric Effects," Vol. 27, p. 98, March 1966; Part II, "Rates of Energy Loss by Energetic Electrons," Vol. 27, p. 600, Dec. 1966; Part III, "Large Signal Acoustoelectric Effects," Vol. 28, p. 634, Dec. 1967; and Part IV, "Field and Temperature Dependence of Electronic Transport," Vol. 30, p. 435, Sept. 1969.

Each of these loss mechanisms has been treated separately in the literature,** which extends over the past sixty years. The modes of treatment cover a wide range of physical models as well as mathematical techniques. For the most part, the analyses are carried out in Fourier space as opposed to real space. While all of the energy losses must, in the strictest sense, be treated by quantum mechanical methods, the higher-energy losses to electronic excitations[1] and Cerenkov radiation[2] have also been examined or approximated by classical methods. The losses to phonons, on the other hand, have almost universally been treated by perturbation theory.

By contrast, we have attempted in this series to treat all of the loss mechanisms by a common model—a model that is relatively simple, graphic, essentially classical, and couched in real space. The necessary consistency with quantum principles has been obtained by imposing the more or less obvious constraints on the classical argument *after* the classical solution was arrived at. These constraints are (1) that the electron energy exceed the energy $\hbar\omega$ of the radiation it emits and (2) that the uncertainty radius of the electrons $\hbar/mv$ be less than the wavelength of emitted radiation. These constraints are sufficient to ensure agreement between the classical argument and the results of quantum mechanics for the *average* rate of loss of energy. The actual loss, of course, takes place via discrete quanta of energy and occurs stochastically in time and space.

The classical argument introduced a new coupling constant β whose values have the natural limits of zero and unity. β was defined as the fraction of the available coulomb energy of the electron that could be transferred to the medium. The coupling constant was successful not only in unifying the wide gamut of energy-loss mechanisms but also in relating the macroscopic acoustoelectric effects to the microscopic electron–phonon interactions. Because this form of coupling constant is new and because it has a broad significance extending beyond the field of energy loss, its meaning and evaluation are examined at length in this paper. The coupling constant bears, for example, on such problems as the Lyddane–Sachs–Teller relation, and the coupled phonon–photon luminescence emission by trapped electrons.

The present form of coupling constant, in particular the fact that it physically can not exceed unity, illuminates several diverse problems, namely, the range of validity of the concept of deformation potential; the concept, introduced by Frohlich,[3] of a spontaneous instability of the structure of energy bands caused by the presence of electrons; and

---

** See parts I and II of this series for list of references.

the concept, treated by Toyazawa,[4] of electrons self-trapped by acoustic phonons. Each of these items will be discussed.

Energy-loss phenomena are generally associated with the imaginary part of the dielectric constant. Our analysis, on the other hand, uses only the real part. The difference is more significant than the well-known free choice one has by virtue of the Kramers–Kronig relations to deal with either the real or imaginary parts of the dielectric constant. For fast electrons, the rate of emission of energy is actually independent of the form of the imaginary part of the dielectric constant, that is to say, independent of the magnitude of the damping constant γ. The reasons for this are discussed in the present paper.

Finally, we add a reminder that the classical approach to spontaneous emission relates this loss to an elementary and well-defined classical interaction between the electron and its medium and avoids whatever mystery may have been attached to it by the formalism of perturbation theory.

Origin of the Coupling Constant β

In the first of this series of papers a mechanical model was introduced as a prototype for the rates of loss of energy by fast electrons in solids. The mechanical model consisted of a stationary particle (analog of the electron) deforming some attendant mechanical system (analog of the solid medium in which an electron is immersed) so that an energy E_w, called an energy well, was stored in the mechanical system. The response time of the mechanical system was taken to be τ.

It is immediately evident that the maximum rate at which the particle can impart energy to the mechanical system is

$$\left.\frac{dE}{dt}\right|_{\max} \approx \frac{E_w}{\tau}. \qquad [1]$$

This is accomplished by letting the particle rest for a time τ sufficient to impart the energy E_w to the mechanical system; abruptly moving the particle to a new position so that the energy E_w is left in the wake of the particle; allowing the particle to remain at rest again for a time τ and again displacing it abruptly; and so on.

If the disturbance created by the stationary particle in the surrounding mechanical system has a diameter d, then the average velocity of the particle in the above argument is of the order:

$$v_o \approx \frac{d}{\tau}. \qquad [2]$$

If the particle now moves at a velocity v, considerably faster than v_o, it will traverse the diameter d in a time $T = d/v$ that is too short to form a complete energy well. Only a fraction $(T/\tau)^2$ of the complete energy well will be left in the wake of the moving particle. The reason for squaring the ratio T/τ is that the momentum imparted to the mechanical system is proportional to T; hence the energy imparted will be proportional to T^2. In summary, then, the particle loses energy to the mechanical system at the rate:

$$\frac{dE}{dt} \approx E_w \left(\frac{T}{\tau}\right)^2 \frac{1}{T} \qquad \text{for } T < \tau$$

$$= E_w \frac{T}{\tau^2}. \tag{3}$$

The parallel expression for the rate of loss of energy by an electron in a solid was obtained from Eq. [3] by using the following equivalents:

$$E_w = \beta \frac{e^2}{K_H d}, \tag{4a}$$

$$T = \frac{v}{d}, \tag{4b}$$

$$\tau = \omega^{-1}. \tag{4c}$$

Eq. [3] then takes on the general form for rate of loss of energy by an electron;

$$\frac{dE}{dt} \approx \beta \frac{e^2 \omega^2}{K_H v}. \tag{5}$$

We have omitted from Eq. [5] a geometric factor that comes from summing up Eq. [5] over a range of shell diameters d. The equivalents shown in Eq. [4a]-[4c] were derived by considering a fast electron losing energy to a mode (e.g., polar optical phonons) whose characteristic frequency is ω. The response time of the medium to an impulsive force is then, by definition, $\tau = \omega^{-1}$. If we fasten our attention on a particular spherical shell around the electron extending from about $d/2$ to $3d/2$, the disturbance in the medium also has these dimensions and the transit time is of order v/d. Finally, we recognize that the only way the electron can act on the medium (ignoring its spin) is via its coulomb field. The maximum energy the electron can impart to the medium is its vacuum coulomb energy e^2/d. If the electron is imparting energy by polarizing the medium, the maximum energy is reduced by K_H to $e^2/(K_H d)$ where K_H is the dielectric constant for frequencies higher than those under consideration (in the case of optical phonons, K_H is the electronic part of the dielectric constant). This part of the polarization permanently clings to the moving electron and masks the field and energy that it has available for doing work on the slower responding elements of the medium. The factor β (where $0 \leqslant \beta \leqslant 1$) was introduced purely formally to recognize that, in general, only a fraction of the available coulomb energy could be imparted to the medium. This fraction is not to be confused with the fraction $(T/\tau)^2$, which enters in explicitly to take into account the imperfect transfer of energy arising from the fast motion of the electron—fast compared with the response time of the medium. The factor β has to do with the fraction of coulomb energy that can be transferred to the medium when the electron is essentially stationary. That is, it may have a quantum mechanical kinetic energy of localization but it is not moving through the medium. The act of imparting energy is defined by the operation of suddenly displacing the electron in the medium. The energy left behind in the medium where the electron was is the energy imparted. This operational definition is, of course, designed to match the manner in which a moving electron leaves behind a trail of energy in the medium.

In addition to the formal definition of β as the fraction of available coulomb energy imparted to the medium, two other expressions for β were obtained for use in particular cases, namely,

$$\beta = \frac{K_L - K_H}{K_L}, \tag{6}$$

and

$$\beta = \left.\frac{\text{Electrical energy}}{\text{Total energy}}\right|_{\text{Lattice deformation}} \tag{7}$$

For well-separated resonances in a solid as, for example, the ionic resonances at a few hundredth of a volt and the electronic resonances at a few volts, the dielectric constants K_H and K_L in Eq. [6] refer to values above and below the resonance in question and on the flat parts of the dielectric constant versus frequency curves.

Eq. [7] is more general. If one thinks of any elastic deformation of a solid, there will be associated with this deformation an elastic energy and, in general, an electrical field energy. The total energy of the deformation will be the sum of the elastic energy and the accompanying electric field energy as, for example, in the case of a deformation in a piezoelectric solid. This is the total energy that appears in the denominator of Eq. [7]. The electrical energy that appears in the numerator denotes the energy that electrons can gain by relaxing to the new conditions of the deformed medium. This relaxation takes on a variety of forms. For example, a sine-wave deformation in a piezoelectric solid is accompanied by a sine-wave potential and field pattern. The electrical energy is the energy that electrons can gain by congregating in the troughs of the wave. In this case, the electrical energy is also equal to the electric field energy, i.e., $\mathcal{E}D/(8\pi)$. This is also true for polar optical phonons or for any deformation that creates a real, macroscopic electric field. We must note, parenthetically, that the electric fields that go to make up the elastic energy are, in contrast, atomic in dimensions and not coherent beyond an atomic layer. The term "real" is inserted as a reminder that the slope of an energy band caused by deformation or doping is not a real field in the Maxwellian sense even though it acts on free carriers as if it were. Note that, in the case of real, macroscopic electric fields, the field appears both as the numerator of Eq. [7] and as one term in the denominator. Hence, β can not exceed unity. This is consistent with its definition.

For deformations that are not accompanied by a real, macroscopic electric field, the total energy in the denominator of Eq. [7] is just the elastic energy. The numerator is still the energy that is gained when the free carriers relax into the new energy level system of the deformed medium.

The first part of this paper is concerned with the meaning of the coupling constant β. It will be derived both for mechanical and for electrical systems. It will include also a proof that the two expressions for β, Eqs. [6] and [7], are equivalent for deformations accompanied by real, macroscopic electric fields. The proof has the added bonus of yielding a generalized expression for the Lyddane–Sachs–Teller relation.[5] The meaning of the more general form for β, Eq. [7], will be discussed in relation to the question of whether β can exceed unity and in relation to the more conventional treatments of energy loss.

In summary, the central parameter determining the energy losses by electrons in solids is the coupling constant β. Eq. [7] gives its most general definition. β is a direct measure of the transfer of energy between two systems. And, finally, a reminder that the rates of energy loss can be used, as shown in Part IV, to obtain the normal, temperature-dependent mobilities of electrons in solids.

Energy Transfer in Mechanical Systems

We derive here the fraction of the energy of a compressed spring that can be transferred to a second quiescent or undistorted spring. This will depend on the relative spring constants. It will turn out also to be a symmetric fraction so that it will be independent of whether the transfer is from first spring to second or vice versa. In both these respects the springs not only offer a graphic parallel for the transfer of energy in electrical systems but also yield the correct quantitative relations.

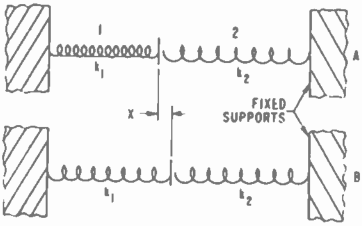

Fig. 1—Energy transfer between springs.

Consider, first, two springs with equal spring constants (Fig. 1). The first spring is compressed and the second undistorted. The two springs are in end to end contact. The first spring is released and the springs settle down after dissipating their kinetic energy so that they have equal amounts of stored energy. If the first spring was compressed by an amount s, the final rest position will obviously find each spring compressed by an amount $s/2$. This will mean that each spring has an elastic energy ¼ of the initial energy of the first spring since the elastic energy varies as s^2. In brief, ¼ of the initial energy of the first spring was transferred to the second. If we had examined the system before the kinetic energies were dissipated we would, of course, find equal amounts of kinetic and potential energy such that half the energy of the first spring had been transferred to the second spring. Equal spring constants represent the conditions for optimum transfer of energy.

We now examine the same problem but this time with different spring constant k_1 and k_2. Again, let the first spring be compressed an amount s. After release, the two springs will come to rest at a point at which their forces of compression are equal, namely,

$$k_1(s\text{-}x) = k_2 x. \tag{8}$$

The energy transferred to the second spring is then

$$\Delta E = \tfrac{1}{2} k_2 x^2, \tag{9}$$

and the ratio of this energy to the initial energy is

$$\frac{\Delta E}{E} = \frac{\frac{1}{2} k_2 x^2}{\frac{1}{2} k_1 s^2}. \tag{10}$$

From Eq. [8]

$$\frac{x}{s} = \frac{k_1}{k_1 + k_2}. \tag{11}$$

Insertion of Eq. [11] into Eq. [10] yields

$$\frac{\Delta E}{E} = \frac{k_1 k_2}{(k_1 + k_2)^2}. \tag{12}$$

Eq. [12], by its symmetry, confirms the fact that the fractional energy transferred from one spring to the other is independent of which spring initially held the energy. Eq. [12] also reproduces the factor ¼ for optimum transfer when the spring constants are equal, or the factor of ½ if we add the kinetic energy.

Finally, for $k_1 \ll k_2$:

$$\frac{\Delta E}{E} \doteq \frac{k_1}{k_2}. \tag{13}$$

We can imagine, at this point, that k_1 represents an electrical energy (like that of a coulomb field) and that k_2 is the sum of two springs in parallel, one with the constant k_1 representing an electrical energy and the second with the constant k_3 representing an elastic energy. Then:

$$\frac{\Delta E}{E} \doteq \frac{k_1}{k_2} = \frac{k_1}{k_1 + k_3} = \frac{\text{electrical energy}}{\text{electrical energy} + \text{elastic energy}}$$

$$= \left.\frac{\text{electrical energy}}{\text{total energy}}\right|_{\text{spring \#2.}} \qquad [14]$$

If spring #2 represents the medium on which spring #1 (the electron) is doing work, we have confirmed, in brief, that the fraction of coulomb energy transferred to the medium is as shown in Eq. [7],

$$\beta = \frac{\Delta E}{E} = \left.\frac{\text{electrical}}{\text{total energy}}\right|_{\text{lattice deformation}} \qquad [15]$$

Transfer of Energy in Electrical Systems

In this section, we will reproduce the spring arguments for an electrical system consisting of a capacitor with fixed charges and a dielectric that can be moved in and out of the capacitor. It will turn out that the energy that can be transferred from the electric field of the capacitor to the dielectric medium will follow the same pattern as that of the two springs. The arguments here, however, will be somewhat more involved algebraically but are worth going through in detail because they yield a generalized form for the Lyddane–Sachs–Teller relation. The capacitor with fixed charges acting on a removable dielectric is the equivalent of an electron moving through a polarizable medium.

Consider a medium whose dielectric constant has the classical form, with well-separated resonant frequencies ω_1, ω_2, etc;

$$K_o = 1 + \frac{\omega_{p1}{}^2}{\omega_1{}^2 - \omega^2} + \frac{\omega_{p2}{}^2}{\omega_2{}^2 - \omega^2} + \cdots, \qquad [16]$$

where

$$\omega_{pi} = \frac{4\pi n_i e^2}{m_i},$$

and ω_i, n_i and m_i are the frequency, density, and mass, respectively, of each set of oscillators. The dielectric constant as a function of frequency is shown in Fig. 2. We have omitted from Eq. [16] and the figure the lossy (imaginary) term in the dielectric constant because we will be concerned with the dielectric constant only on the flat parts of the curve somewhat removed from the resonances. This simplifies the algebra. It also emphasizes the contrast between the present treatment, which computes electron energy losses using only the real part of the dielectric constant, and the more conventional treatments, which begin with the imaginary part of the dielectric constant. The contrast, as we will clarify later, is not simply the usual choice one has, by virtue of the Kramers–Kronig relations, of dealing with either the real or imaginary parts of the dielectric constant. It is more fundamental in that the dielectric loss mechanism itself has substantially no effect on the rate at which an electron loses energy to the medium.

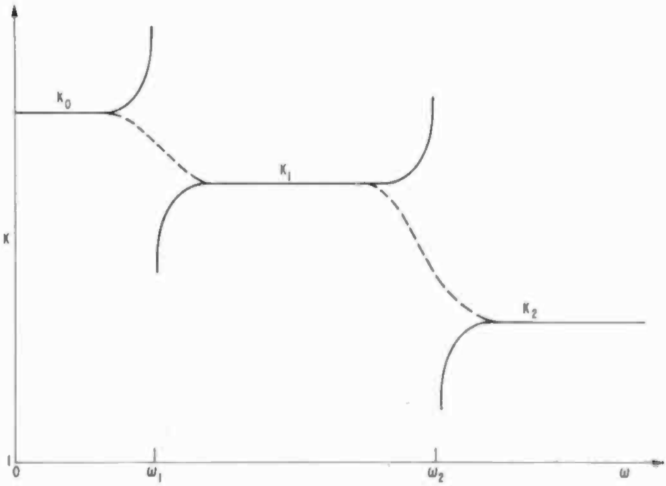

FIG. 2

Fig. 2—Real part of the dielectric constant as a function of frequency. Dotted portions show response to single impulse of duration ω^{-1}.

In Fig. 2 the solid lines are the usual response curves when the dielectric is excited by a periodic force of varying frequency. Near each resonance the response diverges to plus and minus infinity (in the absence of losses). If, on the other hand, we were to subject the dielectric to a single pulse of applied field, the width of the pulse being ω^{-1}, the response of the dielectric, that is, the amplitude of polarization (omitting small transient overshoots), would follow the dotted curve in passing through the various resonances. This is the type of field application we use below.

A further assumption is implicit in Fig. 2, namely, that the series of resonances make either comparable or increasing contributions to the dielectric constant but not decreasing contributions. The purpose of this assumption is to ensure that when we excite the *i*th resonance, the lower frequency resonances are neglibly excited. The assumption does not affect the conclusions drawn. The latter are based on the predominant excitation of a single resonance, independent of how the excitation is achieved.

Following Eq. [16], the dielectric constant K_i is

$$K_i = 1 + \frac{\omega_{pi}{}^2}{\omega_i{}^2 - \omega^2} + \frac{\omega_{pi+1}{}^2}{\omega_{i+1}{}^2 - \omega^2} + \cdots . \qquad [17]$$

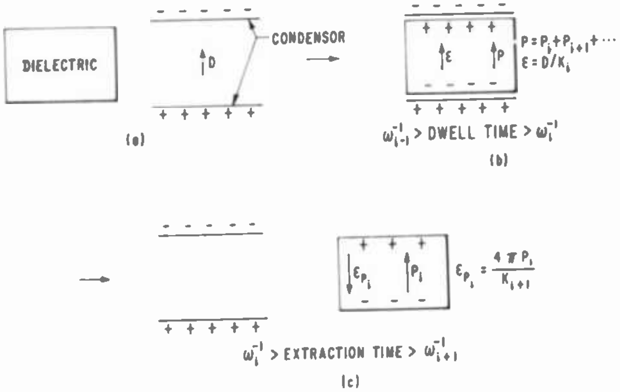

FIG. 3

Fig. 3—Polarization of a dielectric by transient exposure to an electric field.

Fig. 3 shows schematically the series of steps designed to impart the maximum energy to the *i*th mode of oscillation by transient exposure to an electric field. In brief, the dielectric is exposed to an electric field for a time long enough to polarize all of the oscillators beginning with ω_i and extending to higher frequencies but too short to polarize the lower frequencies. The dielectric is then removed in a time long enough to allow the oscillators with frequencies ω_{i+1} and higher to depolarize but too short to allow the oscillators ω_i to depolarize. In this way the oscillators ω_i are fully polarized by the electric field and retain that polarization after the field has departed. The energy of the polarized dielectric in this last step is the energy imparted to the medium.

The definition of β in terms of this model is the ratio of the energy of the polarized dielectric (Fig. 3C) to the "available" energy of the vacuum capacitor. The available energy of the capacitor is its vacuum field energy divided by K_{i+1}. The energy per unit volume of the polarized dielectric is

$$E_m \equiv \frac{1}{8\pi}\left[\frac{(4\pi P_i)^2}{K_{i+1}} + 4\pi \mathcal{E} P_i\right]. \qquad [18]$$

The first term is clearly the electric field energy of the polarization charge P_i. The second term is the elastic or "spring" energy that was stored in the polarized oscillators when they were first immersed in the capacitor field. To emphasize that this term is an elastic energy, and not an electrical energy in the sense of macroscopic electric fields, we can freeze the polarized dielectric and discharge the surface polarization charge so that no macroscopic fields remain. The remaining energy will then be the elastic energy $4\pi\mathcal{E}P_i$ of the polarized oscillators. Note that the energy of the dielectric while immersed in the capacitor field also contains the two terms—an electric field energy and the same elastic energy of the polarized oscillators;

$$\frac{\mathcal{E}D}{8\pi} = \frac{\mathcal{E}}{8\pi}(\mathcal{E} + 4\pi P_i + 4\pi P_{i+1} + \cdots) = \frac{K_i \mathcal{E}^2}{8\pi}$$

$$= \frac{1}{8\pi}(\mathcal{E}^2 + 4\pi\mathcal{E}P_i + 4\pi\mathcal{E}P_{i+1} + \cdots).$$

The distinction between electric field energy and elastic energy is also brought out below (see Eq. [25].

From Eq. [18] and the definition of β we write

$$\beta = \frac{\frac{1}{8\pi}\left[\frac{(4\pi P_i)^2}{K_{i+1}} + 4\pi\mathcal{E}P_i\right]}{\frac{1}{8\pi}\frac{D^2}{K_{i+1}}}, \qquad [19]$$

and use the conventional electrostatic relations,

and
$$\left.\begin{aligned} 4\pi P_i &= \mathcal{E}(K_i - K_{i+1}) \\ D &= K_i\mathcal{E} \end{aligned}\right\} \qquad [20]$$

to reduce Eq. [19] to

$$\beta = \frac{K_i - K_{i+1}}{K_i}. \qquad [21]$$

Hence, Eq. [6] is confirmed as a proper expression for β.

To confirm the equivalence of Eqs. [6] and [7] we write Eq. [7] in terms of the electric and total energy of the medium as given in Eq. [18];

$$\beta = \frac{\dfrac{1}{8\pi}\dfrac{(4\pi P_i)^2}{K_{i+1}}}{\dfrac{1}{8\pi}\left[\dfrac{(4\pi P_i)^2}{K_{i+1}} + 4\pi\mathcal{E}P_i\right]}, \qquad [22]$$

and use Eq. [20] to reduce Eq. [22] to

$$\beta = \frac{K_i - K_{i+1}}{K_i}. \qquad [23]$$

Hence Eqs. [6] and [7] are both valid for expressions for β.

The equivalence of Eqs. [6] and [7] can also be shown in a way that further illuminates the distinction between electrical and elastic energy.

From Eq. [16],

$$\frac{K_i - K_{i+1}}{K_{i+1}} = \frac{4\pi n_i e}{K_{i+1} m_i \omega_i^2}. \qquad [24]$$

Eq. [24] is valid on the flat parts of the dielectric constant versus ω (Fig. 2) where the dielectric constant is independent of ω. We now displace (polarize) each of the ith oscillators by an amount d so that a surface charge $n_i ed$ is formed. Then

$$\frac{K_i - K_{i+1}}{K_{i+1}} = \frac{4\pi n_i e}{K_{i+1} m_i \omega_i^2} \times \frac{4\pi n_i d^2}{4\pi n_i d^2}$$

$$= \frac{(4\pi n_i e d)^2}{8\pi K_{i+1}} \Bigg/ \tfrac{1}{2} n_i m_i (\omega_i d)^2 \qquad [25]$$

The numerator is the electrical energy owing to the surface charge $n_i ed$. The denominator is the maximum kinetic energy of the oscillators corresponding to an amplitude of oscillation d. The kinetic energy is also equal to the maximum potential energy of the oscillators—that is to say, their "spring" energy or elastic energy. Hence:

$$\frac{K_i - K_{i+1}}{K_{i+1}} = \frac{\text{Electrical Energy}}{\text{Elastic Energy}}, \qquad [26]$$

and

$$\frac{K_i - K_{i+1}}{K_i} = \frac{K_i - K_{i+1}}{K_{i+1} + (K_i - K_{i+1})}$$

$$= \frac{\text{Electrical Energy}}{(\text{Electrical} + \text{Elastic})\ \text{Energy}}$$

$$= \frac{\text{Electrical Energy}}{\text{Total Energy}}. \qquad [27]$$

Hence, the definitions of β given by Eqs. [6] and [7] are again shown to be equivalent.

Note that in Eq. [25], the electrical energy increases as the square of the density n of oscillators while the elastic energy increases only linearly.

The Lyddane–Sachs–Teller Relation

The free-standing polarized dielectric in Fig. 3C is an "electret," at least for the time required for the polarization to relax. In actual electrets the polarization is permanently frozen in by cooling and freezing a liquid dielectric in an electric field. The ionic part of the polarization is thereby frozen, while the electronic part is of course free to act. In actual electrets the ionic polarization is likely caused by the orientation of permanent dipoles and consequently does not carry with it an elastic energy.

The energy of the "electret" with its surface charge still intact is given by Eq. [18]

$$\begin{matrix}\text{Energy of "electret"} \\ \text{(with surface charge)}\end{matrix} = \frac{1}{8\pi}\left[\frac{(4\pi P_i)^2}{K_{i+1}} + 4\pi\mathcal{E}P_i\right]. \qquad [28]$$

With the aid of Eq. [20] this energy can be written in terms of D, the vacuum electric field of the capacitor used to induce the polarization in the "electret":

$$\begin{matrix}\text{Energy of "electret"} \\ \text{(with surface charge)}\end{matrix} = \frac{D^2}{8\pi}\left[\frac{1}{K_{i+1}} - \frac{1}{K_i}\right], \qquad [29]$$

If $K_i \gg K_{i+1}$ this energy reduces to

$$\frac{D^2}{8\pi K_{i+1}},$$

and, of course, if $K_{i+1} \to 1$ the energy is just that of the initial capacitor, as one would expect.

One can now discharge the surface charge of the "electret" (e.g., by ionizing the surrounding air) while retaining the frozen polarization. The remaining energy is then just the elastic energy given by the second term of Eq. [28];

$$\begin{matrix}\text{Energy of "electret"} \\ \text{(without surface charge)}\end{matrix} = \frac{\mathcal{E}P_i}{2},$$

or, with the aid of Eq. [20].

$$= \frac{D^2}{8\pi}\,\frac{K_i - K_{i+1}}{K_i^2}. \qquad [30]$$

This is the "frozen in" elastic energy that would be given up as heat if the "electret" were warmed to the point of releasing the polarization.

The Lyddane–Sachs–Teller relation is

$$\frac{\omega_l^2}{\omega_t^2} = \frac{K_L}{K_H},$$

and relates the longitudinal and transverse frequencies of the polar optical modes of an ionic lattice to the low-frequency dielectric constant, K_L, and the high-frequency or electronic part of the dielectric constant, K_H. The squares of the frequencies are proportional to the energy per unit volume of the vibrating lattice. The transverse vibrations have only an elastic energy since macroscopic electric fields would violate the essentially conservative (or relatively static) character of the fields. The longitudinal vibrations have the same elastic energy plus an electric field energy due to the longitudinal polarization of the lattice. Hence, the Lyddane–Sachs–Teller relation can also be regarded as the ratio of the energies of a charged and a discharged "electret" keeping the volume polarization intact. This ratio from Eqs. [29] and [30] is

$$\frac{\text{Energy of charged “electret”}}{\text{Energy of discharged “electret”}} = \frac{K_i^2}{K_i K_{i+1}} = \frac{K_i}{K_{i+1}} = \frac{\omega_l^2}{\omega_t^2}. \qquad [31]$$

Eq. [31] is a generalized form of the Lyddane–Sachs–Teller relation holding even when there are more than the usual two resonances—ionic and electronic—of an ionic solid.

Coupled Phonon–Photon Emission

If a shallow trapped electron recombines with a free hole in the valence band to emit a photon, part of the energy is also radiated away in the form of phonons. Hopfield[6] computed the phonon energy to be

$$E_{\text{phonon}} = \frac{2}{(2\pi)^{1/2}} \frac{e^2}{\epsilon_\infty r} \left(\frac{\epsilon_o - \epsilon_\infty}{\epsilon_o} \right),$$

where $e^2/(\epsilon_\infty r)$ is the binding energy and r the radius of the shallow trapped electron. Williams[7] has confirmed this relation in studies of radiation from GaAs.

In terms of the definition of our coupling constant β, $e^2/(\epsilon_\infty r)$ is the available coulomb energy and $(\epsilon_o - \epsilon_\infty)/\epsilon_o$ is the expression for β for polar optical phonons. The product of these two factors is, then, the energy transferred from the coulomb field to the lattice in the form of elastic energy, and is the phonon energy left behind when the electron makes its radiative transition.

Range of Validity of Deformation Potential

The deformation potential B for acoustic phonons is defined[8] as the shift in energy of the bottom of the conduction band (or top of the valence band) per unit strain s of the lattice. By the nature of its definition, the concept cannot remain valid down to dimensions as small as a lattice spacing since deformations of one lattice spacing cannot be precisely associated with a band edge.

The present definition of coupling constant β offers another quantitative criterion for the dimension or wavelength at which the deformation potential no longer can remain a constant. The coupling constant β was defined as that fraction of the available coulomb energy that could be transferred to the lattice. Hence, β cannot logically exceed unity. In order to find the shortest wavelength for which B is a constant, we equate the β for acoustic phonons (see e.g. Part II of this series) to unity;

$$\beta = \frac{\pi K B^2}{C e^2 \lambda^2} \leqslant 1.$$

If we choose the following representative values: $K = 10$, $B = 4$ eV $= 6 \times 10^{-12}$ erg, $C = 10^{11}$ dynes/cm^2, e in e.s.u., then

$$\lambda \geqslant 2.5 \times 10^{-7} \text{ cm}.$$

For wavelengths shorter than 2.5×10^{-7} cm the value of B must decrease at least in proportion to the wavelength in order that β not exceed unity.

Lattice Instability

In an early discussion of a possible model for superconductivity, Fröhlich[3] proposed that, under certain conditions, the conduction band of a metal might spontaneously deform into a sine-wave pattern with a period of a few lattice spacings in order to achieve the lowest energy state for the metal. The periodicity of the conduction band edge would then give rise to a set of narrow forbidden gaps.

Conceptually, the spontaneous deformation of the lattice means that the electrical energy gained by the electrons settling into the troughs of the sine-wave distortion must exceed the total energy required to distort the lattice. Since the ratio of electrical to total energy of a lattice distortion is one of the ways of defining the coupling constant β, it must then follow that β would have to exceed unity. On the other hand, an equivalent definition of β as the fraction of available coulomb energy that can be imparted to the lattice precludes β exceeding unity. Hence, the lattice instability is logically excluded.

Self-Trapped Electrons

It is expected from the theory of polarons[9] that an electron can be self trapped in an ionic crystal provided

$$\alpha \equiv \frac{(\epsilon_0 - \epsilon_\infty)\, e^2}{\epsilon_0 \epsilon_\infty} \left(\frac{m}{\hbar^3 \omega} \right)^{1/2} > 6.$$

This condition is almost satisfied in ionic crystals and would be more than satisfied if the frequency ω of optical phonons could be substantially reduced from its usual value of about 10^{14}/sec.

Toyozawa[4] has examined the corresponding problem for non-ionic solids, namely, the criterion for self trapping of an electron by acoustic phonons and gives the condition

$$\frac{mB^2}{22\hbar^2 Ca} > 1,$$

where a is the dimension of the self-trapped electron. Its smallest value is a lattice spacing. We can explore the possibility of satisfying this criterion by comparing it with the expression for β;

$$\beta = \frac{\pi}{4} \frac{KB^2}{e^2 Ca^2} \leqslant 1,$$

where we have replaced λ by $2a$.

Noting from the earlier argument that B is a constant only for $\lambda = 2a \geqslant 2.5 \times 10^{-7}$ cm where the value of β approximates unity and that $B \propto \lambda$ for smaller λ, we can write

$$\frac{\pi}{4} \frac{KB^2}{e^2 Ca^2} = \left(\frac{2.5 \times 10^{-7}}{2a} \right)^2, \qquad a > 1.2 \times 10^{-7} \text{ cm},$$

or

$$\frac{B^2}{C} = \frac{4}{\pi}\frac{e^2}{K} \times 10^{-14}.$$

We insert this value into Toyozawa's condition to obtain

$$\frac{2 \times 10^{-14}}{11\pi}\frac{e^2 m}{\hbar^2 K a} > 1,$$

or, since $\hbar^2/e^2 m = 0.5 \times 10^{-8}$ cm,

$$\frac{10^{-6}}{8\,Ka} > 1, \qquad a > 1.2 \times 10^{-7}\text{ cm}$$

The self-trapping condition is obviously not satisfied for dielectric constants $K > 1$, that is, for any real material.

For $a < 1.2 \times 10^{-7}$ cm, we give β its largest value, namely unity, and the above argument yields

$$\frac{10^8 a}{8K} > 1, \qquad a < 1.2 \times 10^{-7}\text{ cm}$$

which, again, is not satisfied for real materials.

Real Versus Imaginary Part of the Dielectric Constant

When a dielectric is subjected to an ac field, the rate of loss of energy to the dielectric and its dissipation by the dielectric into heat is, by definition, given by the imaginary part of the dielectric constant. Hence, the conventional formalism for energy loss by an electron to a dielectric is couched (see Eq. [36], below) in terms of the imaginary part of the dielectric constant. The pulse of electric field exerted by the electron on an element of the dielectric must, of course, be resolved into its fourier components. Our formalism, on the other hand, is couched in terms only of the real part of the dielectric constant. While the Kramers–Krönig relations allow the imaginary part of the dielectric constant to be expressed in terms of the real part, one normally expects the damping constant γ (see Eq. [38]) to appear in the final expression. Our formalism does not contain γ. What we wish to show is that, in a profound sense, the fast-moving electron is insensitive to the presence or absence of dielectric loss processes.

In Fig. 4 we show an electron moving past three different types of elements that the electron might encounter in its medium. The first is a free charge, the second is a bound oscillating charge having negligible frictional loss, and the third is a bound oscillating charge having significant frictional loss. We assume, as is true for most of the range of loss processes we have discussed, that the electron passes each of these elements in a time short compared with the response time of the element. That is to say, the electron gives each element an impulsive kick so that the element undergoes a vanishingly small displacement during the transit of the impacting electron. The meaning of this statement is that the impacting electron does not remain near each element long enough to distinguish whether the element is free, bound without friction or bound with friction. In each case, the impacting electron delivers substantially the same impulse (force × time) and, hence, the same energy, assuming the three elements to have the same mass. After the impacting electron has passed, each element disposes of its energy in its own way. The impacting electron is unaware of these subsequent events; it only knows that it has lost the same amount of energy to each of the elements. Since the impacting electron is unaware of the lossy nature of its medium, it is superfluous to introduce that information into the problem. Moreover, if it is introduced, it must then drop out in the subsequent analysis. It is for this reason that the rate of loss of energy by fast electrons can, at the outset, be expressed in terms of the real part of the dielectric constant only, and that substantially all trace of lossy nature of the medium be ignored.

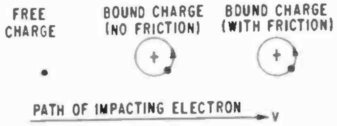

FIG. 4

Fig. 4—Three types of elements encountered by a high-velocity electron in a solid medium.

The above arguments are valid for fast encounters in which the electron interacts with elements of the medium in times short compared with the response time of the element. When the converse is true, the electron does remain in the neighborhood of an element long enough to sense the lossy nature of the element. Here, the imaginary part of the dielectric constant does play a significant role. It should be noted, however, that, in the problems we have discussed, the rate of energy loss in this regime occurs at the maximum of the energy-loss-versus-electron-velocity curve and that this maximum can be approximated within a factor of two by a smooth extrapolation of the high-velocity part of the curve where only the real part of the dielectric constant is significant.

We show in the following argument how the conventional formalism, couched in terms of the imaginary part of the dielectric constant, can be converted, in the case of widely separated resonances, into a form containing only the real part of the dielectric constant and no trace of γ, the measure of the dielectric losses.

The rate of energy loss to polar optical phonons, is, in our formalism,

$$\frac{dE}{dt} = \frac{K_L - K_H}{K_L K_H} \frac{e^2 \omega_o{}^2}{v} \ln \frac{r_2}{r_1}, \qquad [32]$$

where ω_o is the optical phonon frequency, K_L the dielectric constant for frequencies below ω_o, and K_H the same for frequencies above ω_o. The energy loss takes place to elements of the medium lying between the radial distances r_2 and r_1 from the electron path. $r_2 = v\omega_o{}^{-1}$ and $r_1 = \hbar/(mv)$. If we fasten our attention on a particular radial shell surrounding the electron path such that the radius varies by only a factor of about 2, the logarithmic factor reduces to unity. From the classical form for the dielectric constant (see Eq. [16])

$$K_L - K_H = \frac{4\pi n e^2}{M \omega_o{}^2} \equiv \frac{\omega_p{}^2}{\omega_o{}^2}. \qquad [33]$$

Here n and M are the density and mass, respectively, of the ions that give rise to the optical phonon frequency ω_o. With these considerations, Eq. [32] becomes

$$\frac{dE}{dt} = \frac{1}{K_L K_H} \frac{e^2 \omega_p{}^2}{v}. \qquad [34]$$

If we assume further that $K_L - K_H \ll K_H$, then $K_L \approx K_H$ and Eq. 34 can be written

$$\frac{dE}{dt} \approx \frac{1}{K_H{}^2} \frac{e^2 \omega_p{}^2}{v}. \qquad [35]$$

We undertake, now, to show* how the conventional form for energy loss[10]

$$\frac{dE}{dt} = -\frac{2e^2}{\pi v}\int_0^\infty \frac{dq}{q}\int_0^\infty \omega I_m \frac{1}{K(q,\omega)}\,d\omega \qquad [36]$$

reduces to Eq. [35]. The integral over q in Eq. [36] leads to the logarithmic factor in Eq. [32]. By confining our attention to a shell in which the radius varies by about a factor of two, this integral yields a factor of unity. Moreover since we are concerned with the loss of energy to the polar optical phonons only, the upper limit of the integral over ω can be replaced by ω_o+, a frequency somewhat in excess of ω_o. Eq. [36] then becomes

$$\frac{dE}{dt} = -\frac{2e^2}{\pi v}\int_0^{\omega_o+} \omega I_m \frac{1}{K(\omega)}\,d\omega. \qquad [37]$$

We write K(ω) in the form

$$K(\omega) = 1 + \frac{\omega_p{}^2}{\omega^2 - \omega_o{}^2 - i\gamma\omega} + R, \qquad [38]$$

where R is the real part of the contribution to the dielectric constant of elements (e.g., valence-band electrons) having speeds of response much greater than ω_o. The imaginary part of these contributions will be substantially zero for frequencies near or below ω_o+ where the integration terminates.

From Eq. [38] it follows that

$$\text{Im}\,\frac{1}{K(\omega)} = \frac{\omega_p{}^2\gamma\omega}{[(R+1)(\omega^2-\omega_o{}^2)-\omega_p{}^2]^2 + (R+1)^2\gamma^2\omega^2}\,. \qquad [39]$$

By our assumption of $K_L - K_H \ll K_H$, $(R+1)\,\omega_o{}^2 \gg \omega_p{}^2$. It then follows, writing $\omega = \omega_o + \Delta\omega$, that the major contribution to the integral in Eq. [37] occurs near $\omega = \omega_o$ and in the range of $2\Delta\omega = \gamma$. Hence Eq. [37] becomes

---

* I am indebted to Dr. Smith Freeman for the ensuing argument.

$$\frac{dE}{dt} \doteq \frac{2e^2\omega_p{}^2\omega\Delta\omega}{\pi v(R+1)^2\gamma\omega} = \frac{2}{\pi}\frac{e^2\omega_p{}^2}{(R+1)^2v}$$
$$= \frac{2}{\pi}\frac{e^2\omega_p{}^2}{K_H{}^2v}. \qquad [40]$$

Within these approximations Eq. [40] then matches Eq. [35]. The lossy nature of the dielectric, measured by γ, drops out in the evaluation of Eq. [36] because the integral has its major value in the range $2\Delta\omega = \gamma$. Another way of stating this is that Eq. [36] involves the integration of the imaginary part of the dielectric constant over a range of ω where it has a significant value, and the content of this integral is a constant independent of γ.

An alternative way of carrying out the argument is to evaluate $K_L - K_H$ through the Kramers–Krönig relation;

$$K_1(\omega) - K_\infty = \frac{2}{\pi}\int_0^\infty K_2(\mu)\,\frac{\mu}{\mu^2-\omega^2}\,d\mu,$$

where K_1 and K_2 are the real and imaginary parts of the dielectric constant. The result is in the form:

$$K_L - K_H \approx \frac{K_2(\omega_o)\Delta\omega}{\omega_o} = \frac{K_2(\omega_o)\gamma}{\omega_o} = \frac{\text{constant}}{\omega_o},$$

since $K_2(\omega_o)\gamma$ is a measure of the content of the imaginary part of the dielectric constant near ω_o and is a constant independent of γ.

Spontaneous Emission

We conclude this series with a reminder that the major part of it, the rates of energy loss by fast electrons in a solid, is concerned with spontaneous emission. In the literature on spontaneous emission in vacuum, the quantum mechanical formalism has been variously interpreted to reflect the perturbation of an excited state by zero-point vibrations in the vacuum field; to reflect the interaction between an excited state wave function and a possible mode of vibration in the vacuum; and, often, to reflect one of the mysteries peculiar to quantum mechanics, and not describable in classical language. Spontaneous emission in solids is subject to be the same formalism. In the solid, however, it is possible to trace the physical origin of spontaneous emission to the simple, classical, and graphic concept of the polarization of the solid by the electric field of the electron. The energy of the distorted solid left in the trail of the fast-moving electron constitutes the average rate of spontaneous emission. This classical concept leads to the definition of a coupling constant, β, which is equal to the ratio of electrical to total energy of the distorted solid (or medium). The coupling constant is symmetrical in the sense that it measures both the fraction of coulomb energy of the electron that can be transferred to the lattice and the fraction of distorted-lattice energy that can be transferred to electrons. The coupling constant is valid both in the classical limit of energy exchange with classical waves (acoustoelectric effect) and in the quantum limit of energy exchange with phonons (electron–phonon interactions). Finally, it is valid both for induced emission and for spontaneous emission processes, as indeed, is dictated by detail balance.

Acknowledgments

I am indebted to Professor M. A. Lampert and to Dr. A. Rothwarf for critical discussions of a number of parts of this paper.

Addendum to Part III

One of the notable and puzzling observations about the acoustoelectric effect is that the saturated drift velocities in GaAs and InSb are several times larger than the velocity of sound. In CdS and ZnO, the saturated drift velocities are, as expected, quite close to the velocity of sound. An argument was proposed in Part III to account for this difference in terms of the different behavior of the acoustoelectric effect in materials for which $ql > 1$ (GaAs and InSb) and those for which $ql < 1$ (CdS and ZnO).

A more likely source for this difference in behavior lies in the difference in coupling constants β for the two types of material. Qualitatively, one would expect that, in materials with a weak coupling constant, very high elastic strains would be needed to generate the electric fields required to bunch the carriers in the troughs of the acoustic waves. If this strain lies near the yield point of the material, the acoustic losses would be expected to increase so rapidly with increasing strain that the requisite strain could not be achieved.

Quantitatively, following the model initially cited by Smith,[11] one requires the electric field of the acoustic wave to be sufficient to accomodate the space charge of the electrons in a half wavelength. Thus:

$$\mathcal{E} = \frac{4\pi}{K} \cdot \frac{ne\lambda}{2}.$$

The value of $\lambda/2\pi$ at maximum gain is a Debye length:

$$\lambda^2 = (4\pi)^3 \frac{kT}{Kne^2}.$$

Also, by definition,

$$\beta = \frac{\text{Electrical energy}}{\text{Total energy}} = \frac{K\mathcal{E}^2}{4\pi CS^2}.$$

From these three equations, with $C = 5 \times 10^{11}$ dynes/cm², we compute the strain S required to trap all of the carriers:

$$S = \frac{5 \times 10^{-12}}{K} \left(\frac{n}{\beta} \right)^{1/2}$$

For CdS, $K = 9.3$ and $\beta = 5 \times 10^{-2}$. For GaAs, $K = 12.5$ and $\beta = 2.4 \times 10^{-3}$. These values give

$$S_{\text{CdS}} = 2.3 \times 10^{-12} n^{1/2},$$

and

$$S_{\text{GaAs}} = 8 \times 10^{-12} n^{1/2}.$$

Since the carrier densities are usually in the range of 10^{14}-10^{16}/cm³, these expressions yield strains in the range of 10^{-4} to 10^{-3}, namely, in the range of plastic flow or brittle fracture. If, in GaAs, strains approaching brittle fracture are reached before all of the carriers are bunched in the troughs of the acoustic waves, it is likely that the acoustic losses will increase abruptly and the current will level off at values well above those expected for complete saturation at the drift velocity of sound. Evidence that the strains can be in the range of irreversible damage was found by Smith, in some of his early work on CdS, in the form of macroscopic holes drilled through crystals in which the acoustic flux was more than high enough to saturate the drift current.

References:

[1] N. Bohr, **Phil. Mag.**, Vol. 25, p. 10 (1913) and Vol. 30, p. 581 (1915).

[2] L. I. Schiff, **Quantum Mechanics**, p. 271, McGraw-Hill Book Co., New York, 1955.

[3] H. Fröhlich, "On the Theory of Superconductivity: the One-Dimensional Case," **Proc. Roy. Soc.** (London), Vol. A223, p. 296, 1954.

[4] Y. Toyazawa, **Polarons and Excitons,** p. 211, Oliver and Boyd, London (1963), ed. by C. G. Kuper and G. D. Whitfield.

[5] R. H. Lyddane, R. G. Sachs, and E. Teller, "On the Polar Vibrations of Alkali Halides," **Phys. Rev.,** Vol. 59, p. 673 (1941).

[6] J. J. Hopfield, "A Theory of Edge-Emission Phenomena in CdS, ZnS, and ZnO," **J. Phys. Chem. of Solids,** Vol. 10, p. 110 (1959).

[7] E. W. Williams, "A Photoluminescence Study of Acceptor Centres in Gallium Arsenide," **J. Appl. Phys.,** Vol. 18, p. 253 (1967).

[8] W. Schockley and J. Bardeen, "Energy Bands and Mobilities in Monatomic Semiconductors," **Phys. Rev.,** Vol. 77, p. 407 (1950).

[9] See, e.g., H. Fröhlich, **Polarons and Excitons,** p. 1, Oliver and Boyd, London (1963), ed. by C. G. Kuper and G. D. Whitfield.

[10] Taken from T. D. Schultz, **Quantum Field Theory and Many Body Problems,** p. 91, Gordon and Breach, New York.

[11] R. W. Smith, "Current Saturation in Piezoelectric Semiconductors," **Phys. Rev. Letters,** Vol. 9, p. 87 (1962).

Low-Cost Pulsing of Avalanche Diodes

A. S. Clorfeine, R. D. Hughes, and S. Weisbrod

RCA Laboratories, Princeton, N. J.

Abstract—Because of the characteristics of avalanche diodes, modulation of these oscillator elements can, on the one hand, be simplified and, on the other, present special problems. Specifically, a low-power modulator can be used to deliver large pulse powers, and important cost savings can be effected in the design of an avalanche-diode modulator. Also, the use of an RC circuit is found to be quite useful when the diode is operated in the high-efficiency mode. Several methods are discussed for protecting the output transistor against diode failure. Experimental verification of the major points presented is given. A "minipulser" occupying less than 0.1 ft^3 was built and successfully tested.

Introduction

In this report we consider the problem of providing pulse power to avalanche diodes. The modulator (pulser) research was motivated by two factors, (1) the rapidly increasing importance of avalanche diodes as sources of pulsed (as well as CW) microwave power and (2) the unpleasant fact that pulse-modulator cost is greater than that of the diode and rf circuitry. Thus, it has become a major importance to reduce modulator cost. We shall discuss here modulation procedures that accomplish this purpose. More specifically, it is shown (a) how a low-power general-purpose modulator can be employed to deliver large pulse powers, (b) how a low-price transistor can be substituted for a high-price transistor in the fabrication of a special-purpose avalanche-diode modulator, (c) what auxiliary circuit measures can be taken to protect the output transistor, and (d) how to handle a special problem presented by a diode when it is operated in the high-efficiency mode. Experimental results are also presented; these include the use of a specially designed portable "minipulser" to obtain the required large pulse powers.

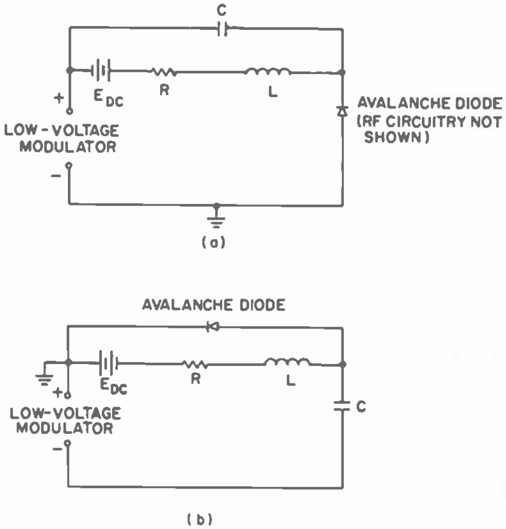

Fig. 1—Pulsing a high-voltage avalanche diode with a low-voltage pulser.

Some Basic Considerations

Once it is stipulated that the load for the modulator is to be an avalanche diode (or any other device which can be biased to a relatively high voltage while drawing little current), then the technique illustrated in Fig. 1(a) becomes applicable. The low-voltage modulator may be a simple periodic source of pulses or a more complicated coded modulator. A dc voltage, E_{DC}, biases the diode slightly below its breakdown value. The capacitor is charged to the same voltage (it is assumed that a dc charging path through the modulator is provided). When a pulse of voltage is turned on, the diode fires (avalanches) and stored energy is released from the capacitor. C is sufficiently large so that the voltage change across it during the pulse is small. The inductance L helps isolate the battery from the pulser during the pulse; however, it may not be necessary if the internal resistance, R, associated with E_{DC} is sufficiently high. Note that the modulator retains control of the output pulse, i.e., the diode extinguishes when and only when the modulator pulse is turned off. Most importantly, note that, with this pulsing technique, a low-voltage low-power pulser can be used to generate the required high-power pulses.

Most of the remarks made concerning the circuit of Fig. 1(a) are equally applicable to that of Fig. 1 (b) in which the diode and capacitor have been interchanged and the polarity of the pulser has been reversed. The latter circuit has two advantages. First the pulser, dc source, and diode can be simultaneously grounded. Secondly, in case the diode shorts, the pulser is not subjected to a large and possibly destructive dc voltage as is the case for the circuit of Fig. 1 (a).

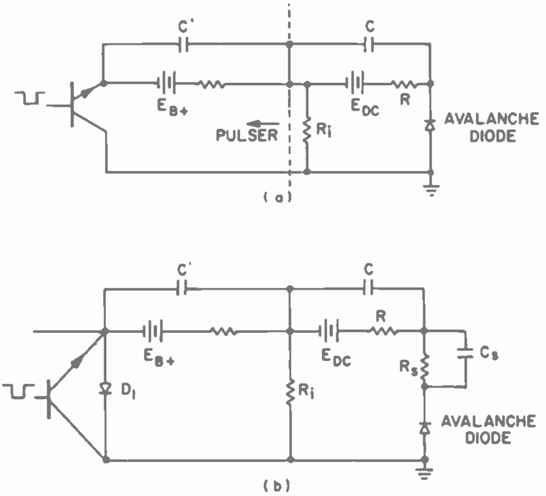

Fig. 2—Modulators for avalanche diodes.

We have described how a low-power general-purpose pulser can be utilized to obtain high pulse powers into an avalanche diode. Now we discuss considerations pertinent to the design of a pulser specifically for use with avalanche diodes. Most of the modulator design (e.g. multivibrators and preamplifiers) can proceed in a conventional manner; however, to make allowances for the special properties of an avalanche diode as a load, the output amplifier stage should be altered. This is now discussed with reference, first, to Fig. 2(a), which again illustrates the basic scheme of Fig. 1 (a), except that the inductance is removed, the output stage of the pulser is shown in more detail, and an isolating resistor R_i is added. Note that without the isolating resistor, the diode current in the absence of a pulse would assume a very small value, and the diode voltage, therefore, would be essentially at the breakdown value irrespective of the values of E_{DC} and E_{B+}, as long as their sum exceeded the breakdown voltage. Actually, it is possible to simplify the circuit by omitting R_l and replacing the two dc sources and capacitors by one of each. In using this simplification, however, we lose, first, the ability for individual control of the diode and transistor voltages and, second, one means of protecting the transistor against failure (this latter point will be discussed shortly).

In any case, what is most important is that, because the load is an avalanche diode, we may use an output transistor with a relatively small voltage rating. For example, if the load were a conventional one and 150 volts were required, a dc load-biasing technique could not be used and the output transistor, therefore, would have to be capable of handling at least 150 volts. For 150 volts (and the same current) into an avalanche diode, one may employ the dc load-biasing technique and an output transistor of, say, 20 volts. The cost difference between the two transistors can be appreciable, especially since they must be of high speed.

These techniques become even more useful in the case of stacked diodes. Stacking avalanche diodes in series appears to be a feasible means of generating higher rf powers.[1] Unfortunately, the peak voltage required to operate a stack of diodes is large. Depending on what the required voltage and response time are, an appropriate transistor is likely to be nonexistent or, at best, exceedingly expensive. The dc-biasing technique described here obviates the need for such a super-transistor (or the need to consider the much less advantageous SCR- or tube-type modulators).

In Fig. 2(b), we have added the elements R_s, C_s and D_1. To understand the need for R_s, consider the situation which is characterized between pulses (i.e., with no transistor base current) by a transistor voltage, for example, of $E_{B+} = 30$ volts. We further assume, for the moment, that the elements R_s and C_s are not used. The initial response to a pulse of base current is an increase in diode voltage and a like decrease in transistor voltage of, say, 20 volts. If, however, the diode is operated in the high-efficiency mode[2] (also referred to as trapatt mode[3] and anomalous mode[4]), the diode voltage will subsequently undergo a large drop (typically 60 volts for an L-band diode), with the transistor voltage increasing by the same amount, in this case to 70 volts. Thus, the transistor must be capable of handling this excess voltage without burning out and, preferably, without a significant increase in transistor (and diode) current. Therefore, we must use a transistor with a voltage rating considerably higher than would otherwise be necessary. This problem, however, can be avoided by employing the resistor R_s. If, for example, we wish to limit the transistor voltage to E_{B+}, the excess voltage, which in this case is 70-30 = 40 volts, may be absorbed across R_s. Hence, if the operating current is 5 A, a resistance of 40/5 = 8 ohms would serve this purpose. Note that the addition of this resistance does not reduce system efficiency, since the power dissipated by R_s (and, perhaps additional power) would otherwise be dissipated by the transistor. Note further that if too large a resistance is used, the threshold current for the high-efficiency mode may not be reached. A function of the capacitance C_s is to short-circuit R_s at the the beginning of the pulse, thereby permitting greater starting power without nullifying the effect of R_s once the high-efficiency mode is triggered. C_s also has been found, empirically, to improve the shape of the pulse. For the transit-time mode of diode operation, R_s and C_s are not necessary, since the change in diode voltage is negligible.

It is particularly desirable in laboratory testing of diodes to minimize the probability that diode failure will trigger transistor failure. Since, for the pulsing techniques described in this paper, the circuit dc voltage greatly exceeds the transistor rating, one might (depending on the specific circuit elements employed) encounter a situation where a shorted diode results in excessive transistor dissipation. One way of possibly avoiding this problem is by employing the configuration of Fig. 1b. Alternatively, a Zener diode (D_1 in Fig. 2b) can be used to ensure that the transistor voltage does not exceed a given value. Finally, voltage division between R_i and R can accomplish the same purpose. Certain factors should be considered, however, if the latter technique is used. If R_i is made too small, then the diode current may become excessive when the device switches to the high-efficiency mode, since a reduction in diode voltage is accompanied by a reduction in voltage and current across R_i and a shifting of this incremental current to the diode (this is most easily seen if one assumes a collector current that is invariant during the switch). On the other hand, too large a value of R_i may necessitate an artificial increase in R and a consequent reduction in system efficiency.

Experimental Results

To show that a high-power avalanche diode can be operated with a relatively low-power general-purpose pulser, a diode was first pulsed conventionally and yielded an rf output power of 192 watts at 1103 MHz. The power input to the diode was measured to be 762 watts. All of this power, of course, was being delivered by the pulser.

The same diode was then pulsed with a Hewlett-Packard 214A generator, rated at 200 watts. The desired operating current (6.4 amperes) necessitated a transformer at the output of the pulser. The circuit of Fig. 1a was employed with $E_{DC} = 135$ volts, $L = 0$, and $C = 3\ \mu f$. Again an output of 192 watts at 1103 MHz was noted. The pulse waveform was excellent except for the increased rise time contributed by the transformer. Only 136 watts of generator power was required.

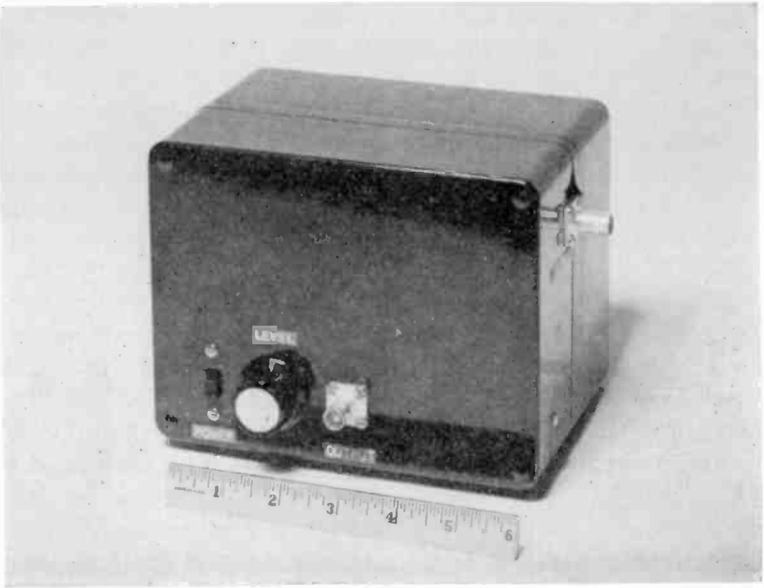

Fig. 3—"Minipulser" for avalanche diodes.

Our next objective was to construct and test a solid-state portable pulser using the techniques described in this report. The resultant "minipulser", is illustrated in Fig. 3. The instrument, which includes batteries, encompasses a total volume of less than 0.1 ft^3 and delivers pulses of greater than 500 watts peak power at a rate of 300 pulses/sec. The preliminary stages of the minipulser consist of a free-running multivibrator, a monostable multivibrator, and a two-stage emitter-follower-amplifier; the output circuitry is as illustrated in Fig. 2b, (except that the Zener diode was not used). The output transistor was an RCA-type 40341 with a collector-to-emitter breakdown voltage rating (with zero base current) of 35 volts. Other parameters in-

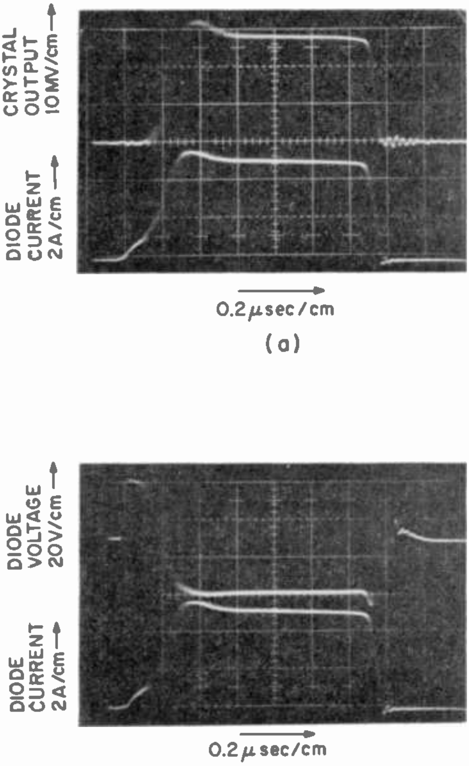

(a)

(b)

Fig. 4—Detected *rf* output, current, and voltage for avalanche diode powered with a minipulser.

cluded $E_{B+} = 45$ volts, $E_{DC} = 135$ volts, $C = 5\mu f$, $R = 2.7$ K and $R_l = 220$ ohms. R_s and C_s were adjusted to 12 ohms and 3900 pF.

The results obtained when the minipulser was used to modulate a high-efficiency-mode oscillator are shown in Fig. 4. The crystal voltage (upper trace in Fig. 4(b)) represents an output power of 138 watts at 1079 MHz. The pulse current is 5.2 A and the diode voltage, after an initial rise, falls to a value nearly 30 volts below the dc value.

Conclusions

Because of the characteristics of avalanche diodes, modulation of these oscillator elements can, on the one hand, be simplified and, on the other, present special problems. Specifically, a lower-power modulator can be used to deliver large pulse powers, and important cost savings can be effected in the design of an avalanche-diode modulator. Also, the use of an *RC* circuit is found to be quite useful when the diode is operated in the high-efficiency mode. Several methods are discussed for protecting the output transistor against diode failure. Experimental verification of the major points presented here are given. A minipulser occupying less than 0.1 ft^3 was built and successfully tested.

Acknowledgments

The interest and cooperation of K. K. N. Chang and A. Rosen in this work are acknowledged with gratitude.

References:

[1] S. G. Liu, "Stacked High-Power Avalanche Diode Oscillators," **Proc. IEEE,** Vol. 57, No. 4, p. 707, April 1969.

[2] A. S. Clorfeine, R. J. Ikola, and L. S. Napoli, "A Theory for the High-Efficiency Mode of Oscillation In Avalanche Diodes," **RCA Review,** Vol. 30, No. 3, p. 397, Sept. 1969.

[3] R. L. Johnston, D. L. Scharfetter, and D. J. Bartelink, "High-Efficiency Oscillations in Germanium Avalanche Diodes Below the Transit-Time Frequency," **Proc. IEEE,** Vol. 56, No. 9, p. 1611, Sept. 1968.

[4] H. J. Prager, K. K. N. Chang, and S. Weisbrod, "Anomalous Silicon Avalanche Diodes for Microwave Generation," Conf. on High-Frequency Generation and Amplification, Ithaca, N. Y., Aug. 30, 1967.

Static Negative Differential Resistance in Bulk Semiconductors

F. Sterzer
RCA Electronic Components, Princeton, N. J.

Abstract—Several simple theorems are derived that are useful in deciding whether a given bar of bulk semiconductor can exhibit a static negative differential resistance.

Introduction

A recurring question in the theory of bulk effect devices is whether a particular bulk device can exhibit a static negative differential resistance. One of the first authors to address himself to this question was Shockley[1] who in 1954 published his "positive conductance theorem". This theorem states that the static differential resistance of a stable, uniformly doped semiconductor of uniform cross-section and with ohmic cathode and anode contacts must always be positive, even if the semiconductor exhibits a negative differential mobility. Kroemer,[2] in 1970, generalized Shockley's positive conductance theorem to include arbitrary geometries and doping distributions, assuming in his calculations that diffusion effects could be neglected. In 1971, Hauge[3] showed that a material with negative differential mobility, a *large* field-dependent diffusion coefficient, and ohmic cathode contacts could exhibit a static negative differential resistance. Earlier (1968), Kroemer[4] had shown that a static negative differential resistance could also be obtained if, instead of ohmic cathode contacts, appropriate injecting contacts were used.

In the present paper several elementary theorems are derived that are helpful in deciding whether a given bulk semiconductor device can or cannot exhibit a static negative differential resistance. The application of these theorems is illustrated by several examples, including a particularly simple derivation of the generalized form of Shockley's positive conductance theorem.

Some Elementary Properties of Devices with Static Negative Differential Resistance

Consider a device with a voltage-controlled static negative differential resistance (see Fig. 1). For any voltage in the negative resistance region of the I-V characteristics such as V_2 of Fig. 1, there is always a corresponding voltage V_1 in the positive part of the I-V characteristics such that $I(V_1) = I(V_2)$. It follows therefore that:

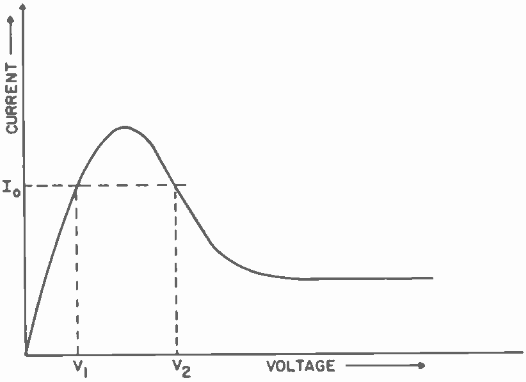

Fig. 1—Current-voltage characteristics of a device with a voltage-controlled static negative differential resistance.

1. A device whose dc voltage is a single-valued function of dc current cannot exhibit a static voltage-controlled negative resistance.
2. A device whose I-V characteristics is continuous and whose dc voltage is a multiple-valued function of dc current must have a static voltage-controlled negative resistance.*

The voltage V across a device is the negative of the line integral of the electric field E from cathode to anode,

$$V = -\int_{\text{Cathode}}^{\text{Anode}} E ds \qquad [1]$$

---

* The corresponding theorems for devices with current-controlled negative resistances are as follows:

1a. A device whose dc current is a single-valued function of dc voltage cannot exhibit a static current controlled negative resistance.

2a. A device whose I-V characteristics is continuous, and whose dc current is a multiple-valued function of dc voltage must have a static current-controlled negative resistance.

Eq. [1] shows that if the electric field distribution is a single-valued function of current, the voltage will also be a single-valued function of current. This fact coupled with Theorem 1 above yields the following theorems:

3. A device whose static electric field distribution is a single-valued function of dc current cannot exhibit a voltage-controlled static negative resistance.
4. A device that exhibits a static negative differential resistance must have a static electric field distribution that, for a range of dc currents, is a multiple-valued function of dc current.

Fig. 2 shows examples of static electric field distributions that would lead to a static negative differential resistance. Branches 1 of the field distributions correspond to voltages in the positive resistance region (such as V_1 of Fig. 1) and branches 2 to voltages in the negative resistance region (such as V_2 of Fig. 1).

Derivation of Shockley's Positive Conductance Theorem

We consider bulk devices with carrier velocities that are single-valued functions of electric field and ohmic cathode contacts. Diffusion effects are assumed to be negligible.

Application of Poisson's equation yields the following equation*

$$\epsilon \frac{\partial^2 V}{\partial s^2} = -\epsilon \frac{\partial E}{\partial s} = -n = \frac{J}{v} - n_d, \qquad [2]$$

where ϵ is the dielectric constant, n is the charge density, J is the conduction current density, v is the electron velocity (the semiconductor is assumed to be n-type), and n_d is the donor density. The electron velocity can be written as

$$v = \mu E, \qquad [3]$$

where the mobility μ is a single-valued function of electric field. Combining Eqs. [2] and [3] gives

$$\epsilon \frac{\partial E}{\partial s} = n_d - \frac{J}{\mu E}. \qquad [4]$$

---

* The calculations are carried out in one-dimension; extension to three-dimensions is straightforward.

The boundary condition for Eq. [4] (ohmic cathode contact) is

$$E = 0 \text{ at } s = 0. \qquad [5]$$

The value of E inside the semiconductor is uniquely determined for every value of current density J by Eqs. [4] and [5]. This means that the electric field distribution is always a single-valued function of current; field distributions like those shown in Fig. 2 cannot occur; and

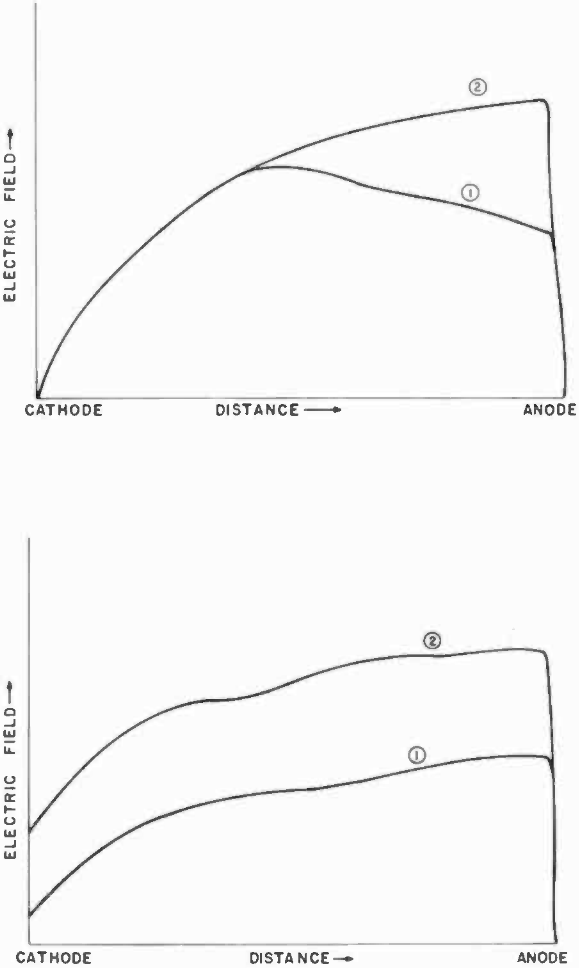

Fig. 2—Examples of static electric field distributions required in devices with a voltage-controlled static negative differential resistance.

according to Theorem 3 the device cannot exhibit a voltage-controlled static negative differential resistance. This remains true, of course, even if the differential mobility of the semiconductor is negative over large ranges of electric field, as is the case for transferred electron semiconductors.

Devices with Non-Ohmic Cathode Contacts

Diffusion is neglected, so that Eq. [4] applies. The cathode boundary conditions are classified into two groups:

$$E = \text{single-valued function of current at } s = 0 \qquad [6]$$

$$E = \text{multiple-valued function of current at } s = 0 \qquad [7]$$

If the cathode boundary condition falls into the class described by Eq. [6], the argument made in the previous section applies and the device cannot exhibit a voltage-controlled static negative differential resistance. On the other hand, if the cathode boundary condition falls into the category described by Eq. [7], an electric field distribution such as the one of Fig. 2b is possible and the device *can* exhibit a static negative differential resistance.[2,4]

Diffusion Effects

If diffusion effects become important, then the electron velocity must be written as

$$v = \mu E - \frac{T}{n}\frac{\partial}{\partial s}(\mu n), \qquad [8]$$

where T is the electron temperature. Substituting Eq. [8] into Eq. [2] yields

$$\epsilon \frac{\partial E}{\partial s} = n_d - \frac{J/\mu E}{1 - \dfrac{T}{\mu E n}\dfrac{\partial}{\partial s}(\mu n)}. \qquad [9]$$

Note that Eq. [9] is a higher order equation in $\partial E/\partial s$, since the product (μn) is a function of both E and s. It follows that $\partial E/\partial s$, and therefore also E, can be multiple-valued functions of current, and the possibility of a static negative differential resistance is not ruled out by Theorem 3. That a static negative differential resistance can be obtained, at least in principle, when diffusion effects are significant can be demonstrated by detailed calculations.[3,5]

References:

[1] W. Shockley, "Negative Resistance Arising from Transit Time in Semiconductor Diodes," **Bell Syst. Tech. J.**, Vol. 33, p. 799, July 1954.

[2] H. Kroemer, "The Gunn Effect Under Imperfect Cathode Boundary Conditions," **IEEE Trans. Electron Devices,** Vol. ED-15, p. 819, Nov. 1968.

[3] P. S. Hauge, "Static Negative Resistance in Gunn Effect Materials with Field-Dependent Carrier Diffusion," **IEEE Trans. Electron Devices,** Vol. ED-15, p. 390, June 1971.

[4] H. Kroemer, "Generalized Proof of Shockley's Positive Conductance Theorem," **Proc. IEEE,** Vol. 59, p. 1844, Nov. 1970.

[5] P. Gueret, "Convective and Absolute Instabilities in Semiconductors Exhibiting Negative Differential Mobility," **Phys. Rev. Letters,** Vol. 27, p. 256, 2 Aug. 1971.

RCA Technical Papers Second Quarter, 1971

April

"Adaptations of Newsfilming Camera Systems," S. Nemeyer, **Jour. SMPTE** (Technical Notes)

"Cesium-Oxygen Activation of Three-Five Compound Photoemitters," A. H. Sommer, **Jour. Appl. Phys.** (Communications)

"Electronic Image Storage Utilizing a Silicon Dioxide Target," R. S. Silver and E. Luedicke, **IEEE Trans. GED**

"Electronic Music Synthesis for Recordings," H. F. Olson, **IEEE Spectrum**

"Plasma-Grown Al_2O_3 for COS/MOS Integrated Circuits," F. B. Micheletti, P. E. Norris, and K. H. Zaininger, **Solid State Tech.**

"Interaction of 9.3-GHz Longitudinal Phonons with Electrons in Superconducting Films," B. Abeles and Coauthors, **Phys. Rev. B** (1 April)

"Mobilities of Electrons and Holes in CaF_2," J. Dresner and P. M. Heyman, **Phys. Rev. B** (15 April)

"Designing Out the Problems of Wide-Angle Color TV Tubes," W. D. Masterton and R. L. Barbin, **Electronics** (April 26)

May

"Adaptations of Newsfilming Camera Systems," S. Nemeyer, **Jour. SMPTE** (Technical Notes)

"Analysis of an Electronic Fence Element for a Vehicle Location System," G. S. Kaplan, **IEEE Trans. GVT**

"Analysis of Photoemissive Schottky Barrier Photodetectors," V. L. Dalal, **Jour. Appl. Phys.**

"Current Crowding in a Circular Geometry," E. S. Kohn, **Jour. Appl. Phys.**

"Direct Measurement of Diffusion Length in GaAs by α Particles," B. Goldstein, **Jour. Appl. Phys.** (Communications)

"Reflections on Muddied Waters," L. S. Nergaard, **IEEE Trans. GAES**

"Simple Model for Internal Photoemission," V. L. Dalal, **Jour. Appl. Phys.**

"Threshold Logic," D. Hampel and R. O. Winder, **IEEE Spectrum**

"Bootstrap Boosts Gain of Low-Noise RF Preamp," R. J. Turner, **Electronics** (Designer's Casebook) (May 24)

June

"The Ad-Conductor Cathode," K. G. Hernqvist, **RCA Review**

"Analysis of Transport Processes During Holographic Recording in Insulators," J. J. Amodei, **RCA Review**

"A Computer Program for Electronic Typesetting," J. L. Pierson, **IEEE Trans. GEWS**

"Contrast Thresholds of Image-Intensifier-Aided Eye at Low Field-Luminance Levels," I. P. Csorba, **RCA Review**

"Decrease in Spontaneous Emission at the Onset of Lasing in Semiconductors," F. H. Nicoll, **Jour. Appl. Phys.**

"Direct and Indirect Optical Energy Gaps of AlAs," W. M. Yim, **Jour. Appl. Phys.**

"Double Extraction of Uniformly Generated Electron-Hole Pairs from Insulators with Noninjecting Contacts," A. M. Goodman and A. Rose, **Jour Appl. Phys.**

"Foreshortening of Microstrip Open Circuits on Alumina Substrates," L. S. Napoli and J. J. Hughes, **IEEE Trans. GMTT** (Correspondence)

"400-MHz Acoustic Surface-Wave Pulse Expansion and Compression Filter," C. L. Grasse and D. A. Gandolfo, **IEEE Trans. GMTT** (Correspondence)

"High-Level Current Gain in Bipolar Power Transistors," J. Olmstead, W. Einthoven, S. Ponczak, and P. J. Kannam, **RCA Review**

"Hot-Electron Distribution in n-GaAs Derived from Photoluminescence Measurements with Applied Electric Field," P. D. Southgate, D. S. Hall, and A. B. Dreeben, **Jour. Appl. Phys.**

"A New Light Valve for Television Projection," J. A. van Raalte, **Jour. SMPTE**

"Observation of the Influence of Base Widening Upon Beta and f_T" C. F. Wheatley, **RCA Review**

"Optical Techniques for Detecting Defects in Silicon-On-Insulator Devices," R. A. Sunshine, **RCA Review**

"Permanent-Holograms in Glass by RF Sputter Etching," J. J. Hanak and J. P. Russell, **RCA Review**

"Phototransistor Arrays of Simplified Design," P. K. Weimer, F. V. Shallcross, and V. L. Frantz, **IEEE Jour. Solid-State Circuits** (Correspondence)

"A Program to Hyphenate English Words," W. A. Ocker, **IEEE Trans. GEWS**

"RF Sputtered Transparent Conductors II: The System In_2O_3-SnO_2," J. L. Vossen, **RCA Review**

"Symmetrical Trough Waveguide Nonresonant Ferrite Isolators and Steerable Antenna," C. P. Wen, **RCA Review**

"System Aspects of Electrophotographic Materials and Processing for Liquid Reversal Toning," E. C. Giaimo and H. Wielicki, **RCA Review**

"Systems and Technologies for Solid-State Image Sensors," P. K. Weimer, **RCA Review**

"A Technique for Selective Electroless Plating," N. Feldstein and T. S. Lancsek, **RCA Review**

"Temperature Dependence of Hole Velocity in p-GaAs," V. L. Dalal, A. B. Dreeben, and A. Triano, **Jour Appl. Phys.**

Patents Issued to RCA Inventors Second Quarter, 1971

April

P. R. Ahrens Color Killer and A.C.C. Circuits (3,573,354)
R. W. Ahrons Counter or Shift Register Stage Having Both Static and Dynamic Storage Circuits (3,573,498)
J. J. Amodei Circuit Producing Output Pulse of Polarity Dependent on Relative Times of Occurrence of Input Pulses (3,576,448)
G. E. Anderson Video Muting Circuits (3,573,365)
W. E. Bahls, R. E. Benway, A. C. Grover, J. Regnault, D. M. Priestley, and L. M. Whitcomb Digital Computer Controlled Test System (3,576,494)
D. J. Barth Circuit for Detecting a Change in Voltage Level in Either Sense (3,575,608)
H. R. Beelitz Electrical System and LSI Standard Cells (3,573,488)
D. S. Bond, A. C. Schroeder, and D. H. Pritchard Apparatus for Generating Test Signals Useful in Measuring Television Transmission Performance without Affecting Receiver Synchronization (3,576,390)
T. A. Bridgewater Noise Immunity Circuit (3,573,492)
J. R. Burns Field Effect Transistor, Content Addressed Memory Cell (3,575,617)
J. D. Callaghan UHF Television Antenna (3,573,832)
D. J. Carlson Oscillator Circuit with Series Reasonant Coupling to Mixer (3,573,631)
N. Feldstein Room Temperature Electroless Nickel Plating Bath (3,574,644)
T. D. Floyd Priority Circuit (3,576,542)
R. A. Gange, Repair of Thin-Film Structure Such as Cryoelectric Memory (3,576,551)
G. H. Heilmeier Decreasing Response Time of Liquid Crystals (3,575,491)
G. H. Heilmeier Fast Self-Quenching of Dynamic Scattering in Liquid Crystal Devices (3,575,493)
P. M. Heyman and Z. J. Kiss Photochromic-Photoconductive Memory (3,576,546)
S. R. Hofstein Semiconductor Vidicon Target Having Electronically Alterable Light Response Characteristics (3,576,392)
W. D. Houghton Television System for Transmitting Auxiliary Information During the Vertical Blanking Interval (3,576,391)
L. M. Lunn FET Control System Employing a Storage Capacitor and Switching Tube Means (3,575,612)
J. C. Miller and C. M. Wine Stroboscopic Display Apparatus (3,573,785)
E. O. Nester and B. J. Lechner Turn-Off Method and Circuit for Liquid Crystal Display Element (3,575,492)
F. H. Nicoll Method of Electrostatic Recording on a Thermoplastic Recording Element (3,574,613)
F. H. Nicoll Cathode Ray Tube with Screen Comprising Laser Crystals (3,575,627)
S. A. Raciti Constant Velocity Vector Generator (3,576,461)
J. F. Schanne Speech Synthesizer Providing Smooth Transition Between Adjacent Phonenes (3,575,555)
J. C. Schira Compensation Circuit for Electronic Photocomposition System (3,573,786)
A. P. Storz and F. P. Chiovarou Method of Making a Phosphorus Glass Passivated Transistor (3,575,743)
C. F. Wheatley, Jr. Phase Splitting Amplifier (3,573,645)
L. A. Zanoni Color Advertising Display Employing Liquid Crystal (3,576,364)

May

J. Avins Integrated Circuit Biasing Arrangements (3,577,167)
E. F. Belohoubek Transistor Package for Microwave Stripline Circuits (3,577,181)
R. J. Clark Light Probe Circuit for Persistent Screen Display System (3,579,225)
J. Craft Automatic Frequency Control Apparatus (3,577,008)
W. J. Dodds Display Device for Providing Graticules of Various Configurations (3,581,002)

R. A. Gange Low Inductance Interconnection of Cryoelectric Memory System (3,579,206)
D. F. Griepentrog Video Amplifier for Driving a Delay Line Between Grounded Collector and Grounded Base Stages (3,578,901)
W. J. Hannan Retrieval of Holographically Recorded Data (3,578,836)
J. R. Harford Automatic Gain Control Systems (3,579,112)
J. R. Harford Signal Translating Stage (3,579,133)
R. C. Heuner Pulse Width Stabilized Monostable Multivibrator (3,578,989)
R. J. Klensch Constant Sized Halftone Dot Image Generator (3,580,995)
R. W. Longsderff Circuit for Starting and Maintaining a Discharge Through a Gas Discharge Tube (3,577,174)
H. J. Mackway Push Button Mechanism (3,579,160)
T. B. Martin and H. J. Zadell Sequence 'And' Gate With Resetting Means (3,577,087)
J. Monsay Apparatus for Synchronized Generation of a Signal from a Composite Color Video Signal Subjected to Signal Perturbations (3,578,902)
R. R. Norley Circuits Using Transistors to Provide Variable Phase Shift (3,579,095)
F. L. Putzrath and C. A. Michel Switching Regulator Having a Diode Connected to an Intermediate Tap of a Choke (3,577,065)
M. Rotolo, Jr. Relaxation Oscillator Gated by Transistor Switch (3,579,144)
W. I. Smith Automatic Impedance Matching Circuits for Variable Frequency Source (3,581,244)
A. I. Stoller Method of Making a Semiconductor Article and the Article Produced Thereby (3,579,057)
P. K. Weimer Coupling and Driving Circuit for Matrix Array (3,579,189)
W. R. Wheatley Optical Semiconductor Device (3,581,162)
R. Williams Single Crystal Zinc Oxide and an Electrophotographic Plate Made Therefrom (3,579,332)
D. H. Willis Video Amplifier Circuit (3,578,900)
D. H. Willis Control Circuits for Preventing Kinescope Color Saturation During Blooming (3,578,903)
E. Wonilowicz and H. F. Machnacz Method of Making Ohmic Contact to Semiconductor Devices (3,579,375)
C. M. Wright Decimal to Binary Conversion (3,579,267)
J. M. Yongue Automatic Chroma Control Circuit (3,578,889)
A. K. Yung C-MOS Dynamic Binary Counter (3,577,166)

June

H. Ball and T. M. Wagner Colored Light Transmission Compensating Encoding Filter (3,588,325)
R. L. Barbin Electromagnetic Deflection Yoke Having Bypass Winding Turns (3,588,566)
L. J. Baun Television Blanking and Synchronizing Signal Generator (3,588,351)
E. P. Cecelski Structural Corner (3,586,359)
J. R. Collard Gallium Arsenide Diodes and Array of Diodes (3,586,925)
J. L. Deckert High Voltage Electron Discharge Tube Having Anode Target (3,590,308)
R. A. Dischert and L. J. Thrope Gamma Correction and Shading Modulation Circuitry for a Television Camera (3,588,338)
P. J. Donald Projection of Color-Coded B and W Transparencies (3,582,202)
M. S. Fischer Control Circuits (3,590,275)
R. E. Flory and W. J. Hannan Crosstalk Reduction in Film Player (3,584,147)
R. E. Flory Continuous Motion Apparatus for TV Film Scanning (3,584,148)
R. E. Flory Registration Apparatus for Television Film Projection System (3,584,149)
H. F. Frohbach Lens Array Imaging System for a Color Encoding Camera (3,588,326)
G. F. Granger and H. Khajezadeh High Voltage Integrated Circuit Including an Inversion Channel (3,582,727)
P. E. Haferl Video Amplifier (3,585,295)
V. P. Head Self Righting Vessel (3,585,952)
J. T. Helzer Signal Transmission in Recorder Systems with Impedance Transformation (3,585,312)
M. E. Heller and H. J. Gerritsen High Resolution Laser Engraving Apparatus (3,588,439)
D. V. Henry Method of Assembly of Electron Tubes (3,587,148)

M. B. Herscher and T. B. Martin Word Recognition System for Voice Controller (3,588,363)

K. H. Hoffman Trigger Pulse Circuits (3,584,240)

M. Horll and K. Sadashige Servo System (3,586,946)

W. P. Imhauser Microwave Transistor with a Base Region Having Low-and-High-Conductivity Portions (3,585,465)

E. King Digital Companding Loop for Monobit Encoder/Decoder (3,587,087)

J. C. Kmiec and A. C. Luther, Jr. Video Tape Reproducer System Having Automatic Standard Selection (3,586,769)

R. M. Kongelka Transmission Including Toothed Belt and Partially Toothed Pulley (3,583,250)

K. A. Long Shadow-Mask Cathode Ray Tube Including a Masking Member Comprising a Skirt Having Indentations and Projections Overlapping and Attached to a Frame (3,585,431)

D. G. Macaulay Reed Armature Valves for Controlling Fluid Flow (3,584,650)

A. Macovski Colored Light Encoding Filter (3,585,284)

D. F. Martin Method and Apparatus for Manufacturing Magnetic Recording Tape (3,588,771)

T. B. Martin Speech Synthesizer Utilizing Timewise Truncation of Adjacent Phonemes to Provide Smooth Formant Transition (3,588,353)

A. H. Medwin Integrated Circuit (3,588,635)

C. M. Mengani Character Parity Synchronizer (3,587,043)

C. H. Morris, Jr. Process for Fabricationg Replicating Masters (3,585,113)

C. M. Morris High Voltage Electron Discharge Tube (3,588,575)

L. J. Nicastro Electro-Optic Devices for Portraying Closed Images (3,588,225)

W. L. Oates Semiconductor Hybrid Power Module Package (3,586,917)

L. S. Onyshkevych Magnetostrictive Element (3,582,408)

T. G. Paterson Electron Check Cashing System (3,588,449)

S. S. Perlman and J. H. McCusker Adaptive Resonant Filter (3,588,551)

H. J. Prager, K. K. N. Chang, and S. Weisbrod UHF or L-Band Non-Free-Running Avalanche Diode Power Amplifying Frequency Synchronized Oscillator (3,588,755)

J. N. Pratt Keyed Burst Separator (RE 27134)

D. H. Pritchard Adjustable Bandwidth Optical Filter (3,588,244)

M. Rosenblatt Digital Signalling System (3,585,596)

R. A. Rubenstein and J. C. Schopp Apparatus for Monitoring and Controlling the Concentration of Powder Particles in a Mixture of Powder and Magnetic Particles (3,587,521)

R. E. Salveter, Jr. Method of Coating Wide-Angle Cathode Ray Picture Tube Envelopes (3,582,394)

R. F. Sanford Coding Arrangements for Multiplexed Messages (3,585,290)

T. A. Saulnier Method for Metallizing Phosphor Screens (3,582,389)

T. A. Saulnier Method of Metallizing Phosphor Screens Using an Aqueous Emulsion Containing Hydrogen Peroxide (3,582,390)

B. Schwartz and W. H. Liederbach Miniature Ceramic Capacitor and Method of Manufacture (3,585,460)

W. W. Siekanowicz, T. E. Walsh, and D. J. Blattner Low Reluctance Resonant Structure in Waveguide (3,582,831)

R. E. Simon and R. L. Rodgers Gallium Arsenide Phosphide Camera Tube Target Having A Semi-Insulating Layer on the Scanned Surface (3,585,430)

A. A. Smalarz Clamp Assembly (3,586,356)

F. M. Sohn Rectangular Shadow Mask Type Color Picture Tube with Barrel Shaped Mask Frame (3,588,568)

P. D. Southgate Field-Excited Semiconductor Laser which Uses a Uniformly Doped Single Crystal (3,586,999)

C. Sun Frequency Multiplier (3,582,760)

G. W. Taylor and P. Goldstein Light Aperture Matrix (3,582,907)

L. J. Thorpe Automatic Black Level Video Signal Clipping and Clamping System (3,582,545)

D. A. Wisner Optical Flaw Detector (3,584,963)

S. Wlasuk Test Signal Generator for Producing Test Patterns for a Television Receiver (3,582,544)

S. Wlasuk Test Signal Generator (3,586,755)

O. M. Woodward Corporate-Network Printed Antenna System (3,587,110)

C. M. Wright J-K' Flip-Flop Using Direct Coupled Gates (3,588,545)

AUTHORS

James E. Berkeyheiser served in the U.S. Navy from 1942 to 1948 as an Aviation Radioman and as an Electronics Technician. He joined RCA Laboratories in March 1948 as a wireman. In September 1950 he was called back into service with the U.S. Navy, where he assisted in the re-establishment of the Aviation Ordinance School at Jacksonville, Florida. He was Supervisor of the electrical phase of instruction. He rejoined RCA Laboratories in June 1952. In June 1960, he received his B.S. degree in Electrical Engineering from Drexel Evening College. Mr. Berkeyheiser has worked on flying-spot scanners, projection color television, panel light amplifiers, and panel light amplifier type of x-ray fluorescent screen. He has worked on thin SiC films and has set up facilities for the deposition of these films. He has also designed equipment for the evaporation and study of thin films. More recently, he has assisted in the study of GaAs lasers. He has also worked on the design and construction of equipment for cathode luminescence studies of materials at temperatures down to 4.2°K and has taken much spectroscopic data using this equipment.

Mr. Berkeyheiser is a member of IEEE.

Jerome K. Butler received the B.S. degree from Louisiana Polytechnic Institute, Ruston, in 1960, and the M.S. and Ph.D. degrees from the University of Kansas, Lawrence, in 1962 and 1965, respectively. From 1960 to 1965 he was a Research Assistant at the Center for Research in Engineering Sciences, University of Kansas. His research was related to electromagnetic wave propagation in anisotropic media and wave propagation in anisotropic media and to the optimization and synthesis techniques of antenna arrays. In 1965, he joined the staff of the Institute of Technology, Southern Methodist University, Dallas, Tex., where he is now Associate Professor of Electronic Sciences and Electrical Engineering. His primary research areas have been in theoretical antenna array studies, wave scattering, electromagnetic wave propagation in semiconductors, semiconductor lasers, and quantum electronics. He has held consulting appointments with Texas Instruments Incorporated, the Geotechnical Corporation of Teledyne, Inc., and Earl Cullum Associates of Dallas, Tex. In the summer of 1969 he was a Member of the Technical Staff, RCA Laboratories, Princeton, N.J., where he did research concerned with electromagnetic wave propagation in solid-state injection lasers.

Dr. Butler is a member of Sigma Xi, Tau Beta Pi, and Eta Kappa Nu.

Alvin S. Clorfeine received the B.S. degree magna cum laude from the City College of New York, New York, N.Y., in 1959, and the M.S. and PhD. degrees in electrical engineering from the Carnegie Institute of Technology, Pittsburgh, Pa., in 1960 and 1966, respectively. In 1961, he joined RCA Laboratories, Princeton, N.J., as a member of the technical staff. Areas of his research have included tunnel diodes, microwave parametric amplification, and millimeter-wave frequency conversion in superconductors, and studies of self-pumped parametric amplification and thermal problems in semiconductor microwave devices. His work with superconductors resulted in an Industrial-Research-100 Award. More recently, in the area of avalanche diodes, he has contributed to the theory of the high-efficiency mode, the attainment of high L-band pulse powers, and the development of cost-saving pulsing methods.

Dr. Clorfeine is a member of Eta Kappa Nu, Tau Beta Pi, Sigma Xi, and IEEE.

Michael Ettenberg received the B.S. degree in metallurgy from Polytechnic Institute of Brooklyn in 1964. From 1964 to 1969 he attended New York University and received an M.S. in 1967 and a Ph.D. in 1969. His dissertation was concerned with the thermodynamic studies of compounds with extended solubility. After graduation, he joined RCA Laboratories as a Member of the Technical Staff and is currently involved in studies of injection lasers and III-IV compound synthesis. He is a member of the American Institute of Metallurgical Engineers, the American Society of Metals and Alpha Sigma Mu Metallurgical Honor Society.

Frank Hawrylo attended Trenton Junior College, graduating in 1958 with an A.S. degree. From 1958 to 1960, he was employed by various departments of the State of New Jersey. In April 1960, he joined RCA Laboratories as a research technician. He has worked on the preparation, fabrication, and evaluation of materials in such areas as tunnel diodes, wide-bandgap transistors, hetero junctions, and light transistors. At the present time he is working on (AlGa) As-GaAs heterojunction lasers.

R. D. Hughes was born in Philadelphia on June 19, 1908. After competing his education he spent five years in the electrical construction industry. Two years more were spent in the Instrument Shop of the Western Electric Company. In 1933 he joined RCA where he worked until 1938 in the Special Apparatus Department at Camden. At that time he was transferred to the Engineering and Research Department where he did television, sound, and radar development work. He moved with the department to Princeton, upon the opening of the RCA Laboratories in 1942. He assisted in the development of the FM Radio Altimeter and other FM-Radar systems. Subsequent assignments in color-television transistor, and electron-tube research followed. Since 1951, he has worked in the area of microwave research. His work has included such areas as traveling-wave tubes, parametric devices, tunnel diodes, Hall-effect devices, superconducting devices, and most recently avalanche diodes.

Robert S. Johnson received his B.S. degree in mathematics in 1950 and his M.S. degree in mathematics in 1951, both from Northwestern University. In 1953, he joined the Institute for Cooperative Research at the University of Pennsylvania where he was assigned to projects BIGBEN and CARAMU. He received his Ph.D. degree in mathematics from the University of Pennsylvania in 1959. He joined RCA in 1959 as a numerical analyst and scientific programmer, and has worked primarily in the areas of orbital mechanics, optimization techniques, and systems simulation. He was responsible for the numerical analysis and programming of the PAGE, LEMIP, and EAST programs. He is a member of the American Mathematical Society and of S.I.A.M.

Werner Kern received a certificate in chemistry in 1944 from the University of Basle, Switzerland, and a diploma in chemical technology in 1946. He published a thesis on the chromatographic isolation and characterization of fluorescing polynuclear hydrocarbons which he discovered in soil. He was analytical research chemist with Hoffmann-LaRoche in Switzerland, and in 1948 transferred to their research division in New Jersey to develop new radiochemical methods. In 1955 he received an AB degree in chemistry from Rutgers University and in 1958 joined Nuclear Croporation of America where he became chief chemist directing research in nuclear and radiation chemistry. He joined RCA Electronic Components in 1959 primarily to investigate semiconductor contamination and surface passivation by radiochemical methods. Since 1964, he has been at RCA Laboratories as a Member of the Technical Staff, where his activity has centered in semiconductor process research in the areas of device passivation, new methods of chemical vapor deposition of dielectric films, and the development of associated analytical methods.

Mr. Kern is a member of the American Chemical Society, the Electrochemical Society, the Society of Sigma Xi, and AAAS, the Geological Society of New Jersey, and is listed in American Men in Science.

Ralph W. Klopfenstein received his B.S. in Electrical Engineering from the University of Washington (Seattle) in 1944. He subsequently studied Applied Mathematics at Iowa State University where he received the M.S. and Ph.D. degrees in 1951 and 1954, respectively. From 1943-46 he served in the United States Navy, completed the United States Navy Radio Material Program, and served as Radio Materiel Officer in the Pacific Fleet. He was employed by the RCA Victor Division, Camden, New Jersey, as an Electrical Engineer in 1948 where he worked on the development of high power filters and transmitting antennas for UHF and VHF television applications. Since 1953, Dr. Klopfenstein has been engaged in research at RCA Laboratories, Princeton, N.J., where he is a Fellow of the Technical Staff. From 1953-57 he was active in research in microwave and UHF filters and antennas. In 1957 he was named Head, Mathematical Services, with principal responsibilities in numerical analysis research and the development of computer programs for applications in scientific problems. From 1962-63 he was on leave of absence and served as Director of the Computation Center and Professor of Mathematics at Iowa State University. Since 1963 he has been engaged in research related to the application of mathematics with a principal interest in the development of algorithms for the numerical solution of differential equations.

Dr. Klopfenstein is a member of the American Mathematical Society, Association for Computing Machinery, Institute of Electrical and Electronic Engineers, Mathematical Association of America, Society for Industrial and Applied Mathematics, and the Society of Sigma Xi.

Henry Kressel received the B.A. degree from Yeshiva College in 1955. He received the S.M. degree in Applied Physics from Harvard University in 1956, and the M.B.A. and Ph.D. degree from the University of Pennsylvania in 1959 and 1965, respectively. Dr. Kressel joined RCA Electronic Components and Devices, Somerville, N. J., in 1959. He has been instrumental in the research and development of high-frequency mesa, planar, and planar epitaxial silicon transistors. In 1961 Dr. Kressel became head of the microwave diode group, where he was responsible for research, development, and pilot-line engineering of gallium arsenide and silicon varactor diodes. From 1963 to 1965, he was on leave of absence doing doctoral work in metallurgy. Upon his return to RCA in 1965, he became head of the Device Physics Group in the Technical Programs Laboratory (Somervile, N. J.). He joined RCA Laboratories, Princeton, in 1966. He is currently head of the semiconductor Optical Devices Research Group. Dr. Kressel is a member of the IEEE, The American Physical Society, and Sigma Xi.

Harry F. Lockwood received the B.S. degree with Honors in Physics from St. Johns College in 1957, and is presently concluding his Ph.D. in Physics at New York University. From 1957 to 1963, Mr. Lockwood was employed at General Telephone and Electronics Laboratories as a Senior Engineer in the Solid-State Group where he worked on solid-state devices including field-effect transistors, tunnel diodes, and injection luminescence devices. He was Project Engineer of the tunnel diode research program that resulted in tunnel diode oscillators capable of operation at frequencies in excess of 20 Gc. Mr. Lockwood was one of the early investigators of injection luminescence in III-V compounds, in particular GaAs and GaAsP. This work preceded the injection laser development. From 1963 to 1969, Mr. Lockwood attended New York University where he was engaged in fundamental studies of spin-lattice relaxation in semiconductors. His doctoral dissertation is entitled "Acoustic Paramagnetic Resonance in Arsenic Doped Germanium." In March 1969 he joined RCA Laboratories as a Member of the Technical Staff and is currently working on liquid phase epitaxy and injection lasers.

Mr. Lockwood is a member of the American Physical Society.

Edward A. Miller received his BA in chemistry in 1960 from LaSalle College, Philadelphia, Pennsylvania and his MS in chemistry in 1966 from Drexel University, Philadelphia, Pennsylvania. He joined RCA Laboratories in 1960 as a research technician and became a Technical Staff Associate in 1963. He has worked on high-pressure Czochralski growth of gallium phosphide, preparation and characterization of eutectic alloys with ordered microstructures, vacuum deposition of silicon, vapor phase growth of III-V compounds and alloys, and most recently on the compound gallium nitride.

T. Murakami received the B.S. degree in E.E. from Swarthmore College in 1944, and the M.S. degree from the Moore School of Electrical Engineering, University of Pennsylvania in 1947. From 1944 to 1946 he was an assistant and research associate in the Department of Electrical Engineering at Swarthmore College. From 1946 to 1961 he was associated with the Advanced Development Section of the RCA Home Instruments Division, Camden, N. J., working on radio-frequency circuit development and analyzing various radio and television problems. Since January 1961 he has been with the Advanced Techniques Development group of the RCA Missile and Surface Radar Division at Moorestown, N. J. Mr. Murakami is a Senior member of the Institute of Electrical and Electronics Engineers and a member of Sigma Xi and Sigma Tau.

Jacques I. Pankove obtained his B.S. (1944) and M.S. (1948) degrees from the University of California. He received his doctorate from the University of Paris in 1960 for a study of infrared radiation and germanium. Since 1948, when he joined RCA Laboratories, he has made many contributions to the understanding, technology, and evolution of various semiconductor devices, including large-area photocells and transistors. He has worked in the field of superconductivity, studies of silicon carbide, and investigations of the optical properties of degenerate germanium and the electrical properties of tunnel diodes in germanium, as well as in superconductors and in thin oxide layers. Currently, he is concerned with the study of injection luminescence and laser action in gallium arsenic and other compounds.

Albert Rose received the A.B. degree from Cornell University in 1931 and the Ph.D. degree in Physics in 1935. From 1931 to 1934 he was a teaching assistant at Cornell University. From 1935-1942 he was with the RCA Tube Division in Harrison, N. J., and since 1942 he has been associated with RCA Laboratories at Princeton, N. J. From 1955 to 1957 he directed the research at Laboratories RCA, Ltd., in Zurich, Switzerland. Dr. Rose is a Fellow of the Institute of Electrical and Electronics Engineers and of the American Physical Society.

R. B. Schilling received the BS in Electrical Engineering from the City College of New York in 1961. He attended Princeton University under the RCA Laboratories Graduate Study Program and received the MS in Electrical Engineering in 1963. Under the RCA Laboratories Doctoral Study Award, he attended the Polytechnic Institute of Brooklyn and received the PhD in Electrical Engineering in 1966. His dissertation was entitled "Selected Topics in Space-Charge-Limited-Currents". From 1961 to 1966 he was a member of the technical staff of RCA Laboratories, Princeton, N. J., where he conducted research on thin film transistors (TFT's), MOS transistors, superconductors, adaptive semiconductor diodes and carried out theoretical studies in space-charge-limited-currents. In December 1966, he transferred to the RCA Solid-State Division, Somerville, N. J., to head a group involved in computer-aided transistor design, design and fabrication of PIN microwave switches, PIN and transistor photodetectors. In July 1968, he was promoted to Engineering Leader-Microwave Module Design where he was responsible for the design of lumped-element microwave integrated systems. He was promoted to his present position of Market Planner, RF and Hybrid Devices, in March 1971.

Dr. Schilling is a member of IEEE, Eta Kappa Nu, Tau Reta Pi, and Sigma Xi.

Fred Sterzer received his B.S. degree in physics from the College of the City of New York in 1951, and his M.S. and Ph.D. degrees from New York University in 1952 and 1955, respectively. From 1952 to 1953 he was employed by the Allied Control Corporation, New York. During 1953 and 1954 he was an instructor in physics at the Newark College of Engineering, Newark, New Jersey, and a research assistant at the New York University. Dr. Sterzer joined RCA in 1954. He is now in charge of the Advanced Technology Laboratory at the David Sarnoff Research Center in Princeton, New Jersey. His work has been in the field of microwave spectroscopy, microwave tubes, light modulators and demodulators, microwave solid-state devices, including parametric amplifiers, harmonic generators, tunnel amplifiers and frequency converters, microwave computing circuits, and bulk effect devices.

Dr. Sterzer is a member of Phi Beta Kappa, Sigma Xi, the American Physical Society, and is a fellow of the IEEE.

Sherman Weisbrod also attended Buffalo University and completed the Advanced Electronics course at RCA Institutes, New York in May 1961. Since then he has been employed as a Research Technician in the Microwave Research Laboratory, RCA Laboratories, Princeton, N. J. During this time he completed the Transistor Course and the Vacuum Technology Course at the RCA Laboratories. Mr. Weisbrod has been engaged in such projects as fabrication of tunnel diodes for microwave uses, Hall-effect isolators, and infrared radiation from bulk GaAs. Since February 1966 he has been actively engaged in work on high-power avalanche diodes.

Kenneth Weller received the B.S., M.S., and Ph.D. degrees in electrical engineering from the University of California in 1965, 1966, and 1969, respectively. From 1960 to 1964, he was employed at the Pacific Missile Range, Point Mugu, California, as a student trainee. He joined RCA Laboratories in August 1969 and is presently doing research in the area of semiconductor devices for millimeter-wave applications.

Dr. Weller is a member of Phi Beta Kappa, Sigma Xi, Eta Kappa Nu, and Tau Beta Pi.